Correlative microscopy reveals abnormalities in type 1 diabetes

de Boer, Pascal

Correlative microscopy reveals abnormalities in type 1 diabetes

Pascal de Boer

2018

The research in this thesis was performed at the department of cell biology of the University Medical Center Groningen.

This PhD project was financially supported by *Stichting Techniek en Wetenschappen* (STW) as part of the Microscopy Valley project (12718)

Correlative microscopy reveals abnormalities in type 1 diabetes

Pascal de Boer

ISBN: 978-94-6295-875-3

Printing of this thesis was generously supported by:
Graduate School of Medical Sciences (GSMS) at the University of Groningen
University Medical Center Groningen
University of Groningen

Printed and published by: ProefschriftMaken || www.proefschriftmaken.nl
Cover design: ProefschriftMaken || www.proefschriftmaken.nl
Cover: "*Birth of an insulin granule*"
Lay-out: Pascal de Boer

rijksuniversiteit groningen

Correlative microscopy reveals abnormalities in type 1 diabetes

Proefschrift

ter verkrijging van de graad aan de
Rijksuniversiteit Groningen
op gezag van de
rector magnificus prof. dr. E. Sterken
en volgens besluit van het College voor Promoties

De openbare verdediging zal plaatsvinden op

woensdag 4 april 2018 om 16:15 uur

door

Pascal de Boer

geboren op 28 december 1988
te Leeuwarden

Promotor
Prof. dr. O.C.M. Sibon

Copromotor
Dr. B.N.G. Giepmans

Beoordelingscommissie
Prof. dr. H.C. Gerritsen
Prof. dr. J.L. Hillebrands
Prof. dr. E.A.J. Reits

Contents

Chapter 1

General introduction and thesis outline

The use of microscopes to visualize the unimaginable many molecular processes within cells and tissues unable to be seen by the naked eye has been key for life sciences over the past centuries. Fluorescence microscopy enables to identify specifically labeled molecules to study their respective roles in the regulation of life in health and disease. The development of fluorescent proteins (FPs), such as green fluorescent protein (GFP), opened up a new dimension, since specific proteins tagged with a FP could be imaged in time and space in living cells[1-3]. However, the diffraction limit of fluorescent light microscopy restricts the lateral resolution to a maximum of approximately 250 nm, precluding the ability to image single biomolecules, typically ranging from 0.1 to 10 nm in size. Super-resolution fluorescent microscopy techniques have been developed to break the diffraction limit approaching the biomolecular scale[4]. However, all fluorescent microscopy approaches are based on imaging of specifically labeled molecules, leaving all the unlabeled molecules 'in the dark'[5]. With electron microscopy (EM) cellular ultrastructure can be analyzed at high resolution. However, specific molecules are hard to define in grey-scale EM data. Furthermore, EM is performed on fixed samples, precluding dynamic imaging as with FPs, making it very difficult to find rare events in time and space. Limitation of both microscopy modalities can be overcome when combined, called correlated light and electron microscopy (CLEM)[6-87, 8]. Dynamic fluorescent imaging can directly be followed by EM to put the process in a ultrastructural context[9, 10]. Furthermore, color introduced by fluorescence to the ever expanding high content EM techniques, such as 3D and large-scale 2D approaches, aides to analyze gigabytes of otherwise grey-scaled data[11-13].

Successful CLEM experiments depend on the choice of suitable probes. Correlating data for CLEM can be performed by 'simply' overlaying fluorescence images on the same region acquired with EM to analyze the ultrastructure under the diffraction limited fluorescent spot[14]. Therefore, all available fluorescent probes can in principle be used in CLEM experiments. Often for CLEM, a more precise localization of the targeted molecules is desired, for example by correlating super-resolution fluorescence microscopy with EM[15-17]. Moreover, by combining fluorescence with electron dense EM probes even higher resolution localization can be obtained, for example by sequential labeling of FPs by immunogold[18] or by probes with both fluorescent and electron dense properties[10, 19-21]. The recognition of electron dense probes in EM still depend on grey-scale and discrimination is mostly based on size and shape, for example with different nanoparticles. Recently, the ability to create high resolution color- instead of grey-scaled images using the primary electron beam in a scanning EM (SEM), has been explored. In this thesis, these 'colorEM' approached are either based on photon emission by specific probes, cathodoluminescence (CL)[22-25], or the release of element specific X-rays, energy dispersive X-ray spectroscopy (EDX)[26, 27], upon electron beam induction, which can then be detected with an optical objective or a dedicated EDX detector respectively. Studying life sciences often involves the regulation and interaction of different molecules in time and space. Therefore, expansion of the still limited CLEM probe toolbox is highly desired to aim for multi-target color labeling with localization at high resolution.

Probes used for microscopy typically contain genetically-encoded, e.g. FPs, or affinity-based targeting to identify proteins of interest. Most affinity-based labeling approaches often involve antibody-mediated immunolabeling, which is mostly applied on fixed material, since antibodies have to penetrate cells and tissue to label the molecules of interest. However, immunolabeling does allow

probing of endogenous molecules in (human) tissue, which is impossible for genetically-encoded targeting.

The aim of this thesis is to develop novel affinity-based CLEM and colorEM probes together with improving labeling approaches for existing probes. Next, improved probes and sample preparation approaches are implemented to study type 1 diabetes (T1D) pathology.

Outline of the thesis

Over the past decade CLEM has been boosted by the development of dedicated probes, specialized sample preparation protocols, improved image registration, dedicated microscopes, and increased throughput. Different methods and CLEM approaches emerged from a wide variety of biological questions. Therefore, there is not just one generic CLEM method for each specific research question. **Chapter 2** provides an overview of the latest developments and future directions of CLEM methodology[6]. Moreover, guidelines, tips and tricks are described to aid novel users to choose the most suitable CLEM approach for their own specific research question.

Classical transmission EM (TEM) imaging on ultrathin sections at high resolution is limited to a micrometer field of view (FOV), leaving out the 'big picture' context of the complete cell or tissue. Large-scale scanning transmission EM (STEM) allows acquisition of complete tissue cross sections at high resolution, termed nanotomy for nano-anatomy, generating 'google-earth'-like datasets. Identification of cells and structures in these gigabyte grey-scaled datasets can be achieved by post-embedding immunolabeling with quantum dots (QDs) as described in **Chapter 3**[28]. QDs showed a tenfold increased labeling efficiency compared to conventional immunogold labeling. Furthermore, QDs are both fluorescent and electron dense, making them very suitable for CLEM as shown in figure 2a of chapter 2. In addition to the ability to perform large-scale EM, STEM imaging provides sufficient contrast when heavy metal staining with uranyl acetate and lead citrate is omitted, which is required for TEM. The absence of these heavy metals facilitated the recognition of QDs on insulin granules, which were masked otherwise.

Chapter 4a and 4b discuss two electron beam induced colorEM approaches. First, **Chapter 4a** describes the use of fluorescent nanodiamonds (FNDs) as multi-purpose microscopy probes[29]. FNDs are used for prolonged fluorescence imaging for their photostability and. Furthermore, nitrogen vacancy containing FNDs have the potential to be observed with CL. Therefore here, CL experiments were performed on smaller FNDs, i.e. 40 and 70 nm, in both an uptake assay and pre-embedding immunolabeling, followed by high resolution localization in epon sections.

Chapter 4b[30]. When performing EM, the focused primary electron beam may eject inner shell electrons from the atoms within a sample, creating an electron vacancy. Then an electron from an higher energy outer shell fills the vacancy and the difference in energy is released in the form of an X-ray. The energies of the emitted X-rays are element specific. By equipping a SEM with a dedicated EDX detector, the elemental content per scanned pixel can be fingerprinted and reconstructed to color images at EM resolution ('colorEM'). EDX allowed to discriminate between 10 nm immunogold labels and cadmium containing QDs, which are otherwise difficult to distinguish. Furthermore, different cell types within rat islets of Langerhans could be discriminated in a label-free manner by looking at the endogenous elements present in the secretory granules. Insulin granules for example are specifically enriched in sulfur. Interestingly, EDX identified endocrine cells at the border of the islet of the diabetic prone normoglycaemic rat used for the method development also contained granules from the exocrine pancreas together with an overall affected ultrastructure. This

observation may hint to a harmful interaction between exocrine and endocrine cells at the onset of T1D.

The underlying mechanism(s) initiation beta cell destruction resulting in type 1 diabetes (T1D) are still poorly understood. Understanding the T1D etiology demands full knowledge of cellular composition and microenvironment of the islets of Langerhans to ultimately find alternatives for insulin therapy. **Chapter 5a** describes an online nanotomy repository of human T1D pancreatic tissue from the network of pancreatic organ donors (nPOD). A first round of analysis of the database revealed the presence of atypical immune cells specifically present in T1D pancreases. Moreover, with EDX intermediate endocrine-exocrine cells were identified in the islets of two of eight T1D donors, and not in non-diabetic donors, similar as observed for rat tissue in chapter 4b. Since intermediate cells have been observed in early-onset T1D human donor islets and in 'pre-diabetic' rats, we hypothesized that exocrine cell damage triggers beta cell stress at T1D onset. This is in accordance with a current notion that the complete pancreas rather than only the islets of Langerhans is affected during T1D. Findings from pilot functional follow up experiments to elucidate beta cell stress upon an exocrine cell trigger are discussed in **chapter 5b.** Insulinoma cell lines have been stimulated with exocrine cell lysates to subsequently assess a possible T1D associated stress response. Most interesting a chemokine that is a prominent expressed during early onset T1D[31] (CXCL-10) is increased by a rat insuloma cell line specifically upon treatment with exocrine cell lysates. This indicates a pro-inflammatory response by these cells. Taken together, EM/EDX data from chapters 4b and 5a combined with findings from the functional follow up experiments from chapter 5b might indicate that exocrine cell damage might serve as a trigger to T1D. Furthermore, Chapter 5b discusses possible follow up experiments and model optimization possibilities to investigate the role of the exocrine pancreas at the onset of T1D.

Chapter 6 provides a summary and general discussion of the thesis. Furthermore, future perspectives following the work in this thesis are discussed. I here conclude that CLEM is a powerful approach to combine the strengths of both light microscopy and electron microscopy modalities. CLEM probes ideally contain fluorescent and electron dense properties to visualize them both in overview, using fluorescence microscopy combined with large scale EM, and to localize them at high resolution in the context of ultrastructure. To expand the CLEM probe tool kit the electron beam will get a prominent role, like with CL and EDX. To achieve multi-target CLEM by affinity based labeling of endogenous targets in (human) tissue, immunoEM approaches need to be further optimized and standardized. By combining the large-scale EM method nanotomy with visualizing endogenous molecules using immunoEM and EDX provided novel clues for a possible trigger for type 1 diabetes, which earned a functional follow up granted by the *European association for the study of diabetes* (EASD). Overall, the take home message is that novel important insights into disease mechanisms or normal life regulation can be gained by combining newly developed advanced microscopy techniques.

References

1. Chalfie, M., Tu, Y., Euskirchen, G., Ward, W. W. & Prasher, D. C. Green fluorescent protein as a marker for gene expression. *Science* **263**, 802-805 (1994).

2. Tsien, R. Y. The green fluorescent protein. *Annu. Rev. Biochem.* **67**, 509-544 (1998).

3. Shaner, N. C. *et al*. Improved monomeric red, orange and yellow fluorescent proteins derived from Discosoma sp. red fluorescent protein. *Nat Biotechnol* **22**, 1567-72 (2004).

4. Schermelleh, L., Heintzmann, R. & Leonhardt, H. A guide to super-resolution fluorescence microscopy. *J. Cell Biol.* **190**, 165-175 (2010).

5. Giepmans, B. N. Bridging fluorescence microscopy and electron microscopy. *Histochem Cell Biol* **130**, 211-7 (2008).

6. de Boer, P., Hoogenboom, J. P. & Giepmans, B. N. Correlated light and electron microscopy: ultrastructure lights up! *Nat. Methods* **12**, 503-513 (2015).

7. Müller-Reichert, T. & Verkade, P. Methods in Cell Biology. **111**, 445 (2012).

8. Müller-Reichert, T. & Verkade, P. Methods in Cell Biology. **124**, 442 (2014).

9. Gaietta, G. M. *et al*. Golgi twins in late mitosis revealed by genetically encoded tags for live cell imaging and correlated electron microscopy. *Proc Natl Acad Sci U S A* **103**, 17777-177782 (2006).

10. Shu, X. *et al*. A genetically encoded tag for correlated light and electron microscopy of intact cells, tissues, and organisms. *PLoS Biol.* **9**, e1001041 (2011).

11. Micheva, K. D. & Smith, S. J. Array tomography: a new tool for imaging the molecular architecture and ultrastructure of neural circuits. *Neuron* **55**, 25-36 (2007).

12. Patwardhan, A. *et al*. A 3D cellular context for the macromolecular world. *Nat. Struct. Mol. Biol.* **21**, 841-845 (2014).

13. Russell, M. R. *et al*. 3D correlative light and electron microscopy of cultured cells using serial blockface scanning electron microscopy. *J. Cell. Sci.* **130**, 278-291 (2017).

14. Peddie, C. J. *et al*. Correlative and integrated light and electron microscopy of in-resin GFP fluorescence, used to localise diacylglycerol in mammalian cells. *Ultramicroscopy* **143**, 3-14 (2014).

15. Betzig, E. *et al*. Imaging Intracellular Fluorescent Proteins at Near-Molecular Resolution. *Science* **313**, 1642-1645 (2006).

16. Watanabe, S. *et al*. Protein localization in electron micrographs using fluorescence nanoscopy. *Nat. Methods* **8**, 80-84 (2011).

17. Kopek, B. G. *et al*. Diverse protocols for correlative super-resolution fluorescence imaging and electron microscopy of chemically fixed samples. *Nat. Protoc.* **12**, 916-946 (2017).

18. van Rijnsoever, C., Oorschot, V. & Klumperman, J. Correlative light-electron microscopy (CLEM) combining live-cell imaging and immunolabeling of ultrathin cryosections. *Nat. Methods* **5**, 973-980 (2008).

19. Gaietta, G. *et al*. Multicolor and electron microscopic imaging of connexin trafficking. *Science* **296**, 503-507 (2002).

20. Giepmans, B. N., Deerinck, T. J., Smarr, B. L., Jones, Y. Z. & Ellisman, M. H. Correlated light and electron microscopic imaging of multiple endogenous proteins using Quantum dots. *Nat Methods* **2**, 743-9 (2005).

21. Lam, S. S. *et al*. Directed evolution of APEX2 for electron microscopy and proximity labeling. *Nat. Methods* **12**, 51-54 (2015).

22. Glenn, D. R. *et al*. Correlative light and electron microscopy using cathodoluminescence from nanoparticles with distinguishable colours. *Sci. Rep.* **2**, 865 (2012).

23. Narváez, A. C., Weppelman, I. G. C., Moerland, R. J., Hoogenboom J.P. & Kruit P. Confocal filtering in cathodoluminescence microscopy of nanostructures. *Applied physics letters* **104** (2014).

24. Nagarajan, S. *et al*. Simultaneous cathodoluminescence and electron microscopy cytometry of cellular vesicles labeled with fluorescent nanodiamonds. *Nanoscale* **8**, 11588-11594 (2016).

25. Garming, M. W. H. *et al*. Nanoparticle discrimination based on wavelength and lifetime-multiplexed cathodoluminescence microscopy. *Nanoscale* **9**, 12727-12734 (2017).

26. Somlyo, A. V., Shuman, H. & Somlyo, A. P. Composition of sarcoplasmic reticulum in situ by electron probe X-ray microanalysis. *Nature* **268**, 556-558 (1977).

27. Shuman, H., Somlyo, A. V., Safer, D., Frey, T. & Somlyo, A. P. Applications of energy filtered imaging in biology. *Scan. Electron Microsc.* **(Pt 2)**, 737-743 (1983).

28. Kuipers, J., de Boer, P. & Giepmans, B. N. Scanning EM of non-heavy metal stained biosamples: Large-field of view, high contrast and highly efficient immunolabeling. *Exp. Cell Res.* **337**, 202-207 (2015).

29. Hemelaar, S. R. *et al*. Nanodiamonds as multi-purpose labels for microscopy. *Sci. Rep.* **7**, 720-017-00797-2 (2017).

30. Scotuzzi, M. *et al*. Multi-color electron microscopy by element-guided identification of cells, organelles and molecules. *Sci. Rep.* **7**, 45970 (2017).

31. Uno, S. *et al*. Expression of chemokines, CXC chemokine ligand 10 (CXCL10) and CXCR3 in the inflamed islets of patients with recent-onset autoimmune type 1 diabetes. *Endocr. J.* **57**, 991-996 (2010).

Chapter 2

Correlated light and electron microscopy: ultrastructure lights up!

Pascal de Boer[1], Jacob P. Hoogenboom[2], Ben N.G. Giepmans[1]

[1]Department of Cell Biology, University Medical Center Groningen, Groningen, the Netherlands;
[2]Faculty of Applied Sciences, Delft University of Technology, Delft, the Netherlands.

Nature Methods (2015) 12(6): 503-513

Abstract

Microscopy has gone hand in hand with the study of living systems since van Leeuwenhoek observed living microorganisms and cells in 1674 using his light microscope. A spectrum of dyes and probes now enable the localization of molecules of interest within living cells by fluorescence microscopy. With electron microscopy (EM), cellular ultrastructure has been revealed. Bridging these two modalities, correlated light microscopy and EM (CLEM) opens new avenues. Studies of protein dynamics with fluorescent proteins (FPs), which leave the investigator 'in the dark' concerning cellular context, can be followed by EM examination. Rare events can be preselected at the light microscopy level before EM analysis. Ongoing development—including of dedicated probes, integrated microscopes, large-scale and three-dimensional EM and super-resolution fluorescence microscopy—now paves the way for broad CLEM implementation in biology.

Introduction

Fluorescence microscopy (FM) allows researchers to identify specific molecules and study their biological roles. However, because a large fraction of molecules remain unlabeled and therefore 'in the dark', the context of the localization is lost. In addition, the resolution of light microscopy (LM) is typically submicrometer and thus does not match the size of biomolecules, which typically range from 0.1 to 10 nm. The way to analyze molecules both in their biological context and at high resolution is via EM. However, with EM, ultrastructural analysis is on grayscale images, in which molecules are hard to define; biological samples are in a fixed state; and finding rare events in space and time is nearly impossible. These limitations can be overcome with CLEM (**Box 1**), which combines the strengths of the two modalities and enables the analysis of rare cellular (or subcellular) events in their cellular context. Recent developments in probes, sample preparation, super-resolution FM, image overlay, dedicated microscopes and data handling have provided a boost for CLEM in the past decade. Not only is resolution now better matched between the two modalities but EM analysis can now also be performed over larger volumes. Together with improving methodology, better matched scales (**Fig. 1**) between the two modalities makes CLEM more widely applicable in biology. Here we review the basic ingredients for CLEM, as well as the latest developments. We provide guidelines, tips and tricks for their generic implementation in biology, and we discuss the road ahead toward crisp and bright CLEM analysis of cells, structures, molecules and ultrastructure.

Box 1| CLEM terminology

CLEM is the acronym for correlated (or correlative) light microscopy and electron microscopy, where light microscopy typically refers to fluorescence light microscopy. CLEM implementation varies widely and is often based on the hardware used. Examples of hardware include ILEM[32] and SCLEM[15] for integrated microscopes and simultaneous CLEM, respectively. However, the "I" in ILEM may refer to immunobased CLEM, and the "S" in SCLEM to scanning or serial CLEM. Moreover, in "cryo-CLEM," the term "cryo" may refer to cryo-EM with cryo-LM or with room-temperature FM. We propose to use the acronym CLEM generally, with further explanation detailed in materials and methods sections of research articles.

Microscopy and acquisition

CLEM is typically performed in one of two ways in which any FM or EM modality can be used: (i) samples are analyzed by fluorescence imaging—for instance, time-lapse studies of FP-tagged proteins—followed by fixation and further EM processing, acquisition and analysis, or (ii) ultrathin sections prepared for EM still contain fluorescent label, or are fluorescently labeled, and are imaged with both LM and EM (**Fig. 2**), for instance after immunolabeling. The latter approach also allows for analysis with integrated microscopes as discussed below. Probes to identify specific molecules, organelles or cells are either genetically encoded or affinity based. A subset of specific CLEM probes can allow detection in both microscopes. However, precautions or specific strategies are needed to perform CLEM: routine FM procedures and EM preparation are often mutually exclusive in that either fluorescence is lost or the ultrastructure is destroyed. Thus, CLEM requires special attention to sample preparation[1].

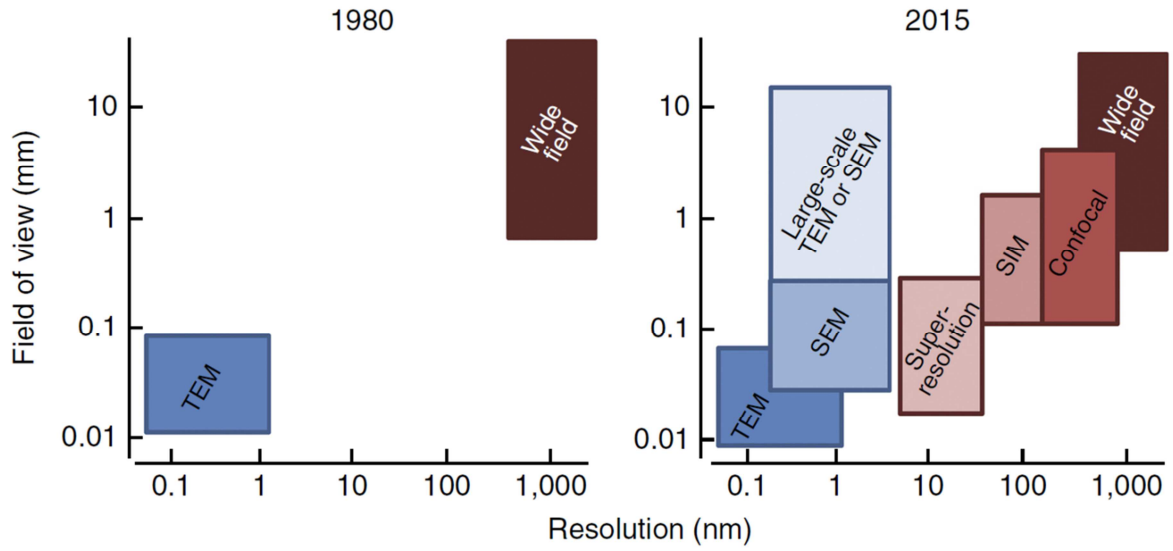

Figure 1 | Matching scales. The gap between EM (blue) and FM (red) in lateral dimensions has been filled by increasing the EM field of view, imaged at high resolution, mainly by automation and digitization, and by 'breaking' the FM diffraction limit, resulting in nearly matching scales for CLEM. Note that all FM and EM approaches depicted here can be used for CLEM. SIM, structured illumination microscopy.

Sample preparation

Chemical fixation and embedding. Classical EM preparation involves fixation and staining with heavy metals followed by plastic embedding and sectioning[2, 3] (**Figs. 2a–c and 3**). Labeled molecules may be visualized after EM preparation using sequential FM and EM contrast with combinatorial tags (Figs. 2a–c and 3) or post-embedding labeling of the section (discussed below in Probes for CLEM). Common fluorescent probes, such as FPs, are incompatible with classical EM sample preparation; although protocols can be used to preserve fluorescence in the EM sample, for both immunotargeted fluorophores[4, 5] and genetically encoded probes[6-11] (Fig. 2d,e), this may come at the expense of ultrastructural preservation. Fluorescence reduction caused by treatment with high concentrations of osmium and by complete dehydration may be prevented by cryofixation[6, 7, 10, 12] or Tokuyasu-like sample preparation[13]. Integrated FM-EM inspection in a vacuum is also being optimized[10, 14, 15] (Fig. 2d,e). Alternatively, cryogenic EM can be performed.

***Cryo-microscopy*.** In cryo-electron microscopy (cryo-EM), biomaterials are preserved in a near-native frozen hydrated state, which does not require chemical fixation or embedding. Samples (small cells, viruses or macromolecules) can be rapidly vitrified, which allows for fluorescence preservation[16, 17]. Although brightness may decrease under cryogenic conditions, photobleaching rates are also reduced; this leads to prolonged observation times, which may be beneficial for some CLEM applications, as discussed below.

Data acquisition and overlay

Sequential acquisition and matching regions of interest (ROIs). Sample transfer between microscopes offers a free choice in FM modalities before EM, including wide-field, confocal and super-resolution FM. Because EM sample preparation can be performed after FM acquisition, there are many options for labeling and staining techniques that allow ultrastructural preservation and EM contrast, as they are not constrained by the need to preserve fluorescence. For cryogenic studies, dedicated sample holders for cooling have been developed for light microscopes that can then be transferred to a cryo-electron microscope[18-20]. Commercial versions are available at FEI (CryoStage$_2$), Linkam (CMS196)[21] and Leica (Cryo CLEM)[17]. Matching the observed areas between modalities, or image registration, is essential for CLEM, and retrieval of an ROI identified with FM in the EM image has long been a major issue in correlative microscopy. Finder grids enable coarse alignment of a sample from live-cell observation to EM[22]. Commercial sample holders with navigation markers recognized by microscope software for automated ROI retrieval from Carl Zeiss (Shuttle & Find and Atlas5) and Jeol/Nikon (MiXcroscopy) are now available. The ROI can also be retrieved on the basis of LM data by means of virtual overlay[23], and both FEI (MAPS and CorrSight) and Jeol (JEM-1400Plus) provide recognition software. Three-dimensional (3D) alignment markers can be created in the sample by branding optical marks using laser irradiation, which are suitable for 3D CLEM[24]. Although these techniques do help to match areas, the accuracy they offer is too low for several applications.

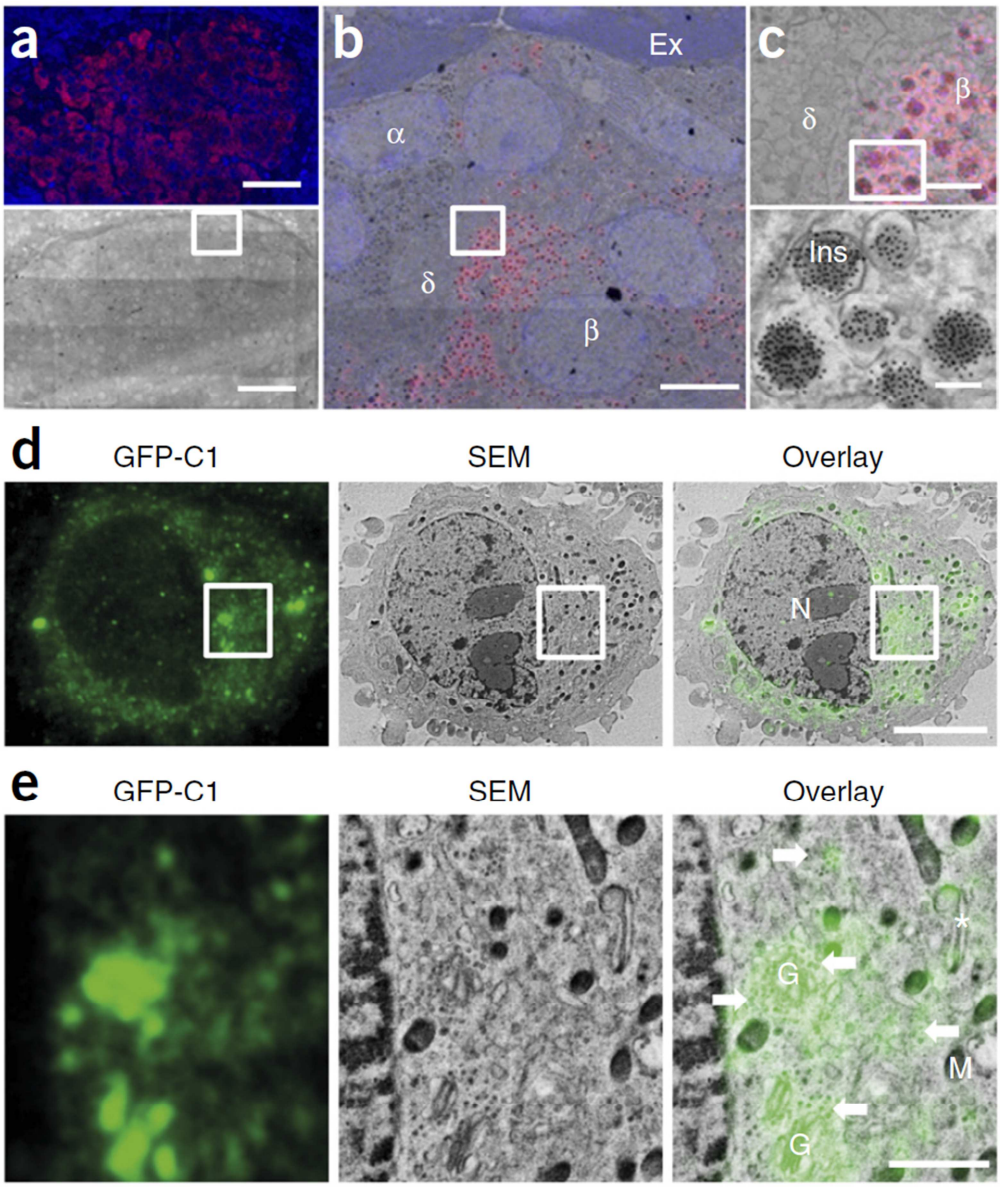

Figure 2 | Examples of CLEM with distinct approaches. (**a–c**) Post-embedding insulin immunolabeling (biotin-labeled antibodies) by QDs (streptavidin-conjugated QD655, red) and Hoechst counterstain (blue) of rat pancreas[73]. FM (top) followed by scanning EM (bottom) and overlay (**b**). (**c**) Boxed area from **b** (top) and magnification (bottom). Note the detection of the electron-dense nanoparticles. Ex, exocrine pancreas; α, alpha cell; β, beta cell; δ, delta cell; Ins, insulin granule. (**d**,**e**) Integrated microscopy (SECOM) of resin-embedded HeLa cells expressing GFP-C1, a diacylglycerol sensor, prepared with high-pressure freezing followed by freeze substitution[10]. Fluorescence from a 200-nm section (left), the matching back-scattered electron image (center) and the overlay (right) are shown. Note how precise subcellular localization of the fluorescent signal allows identification of corresponding structural features. (**e**) Detail from **d**, showing fluorescence corresponding to putative vesicular structures (arrows), Golgi networks and other highly curved membranous structures within the cytoplasm (asterisk). G, Golgi network; M, mitochondrion; N, nucleus. Images in **a–c** are our unpublished results; images in **d**,**e** are unpublished data kindly provided by C.J. Peddie and L.M. Collinson (Cancer Research UK). Scale bars: 50 µm (**a**), 5 µm (**b**,**d**), 1 µm and (**c**, top, and **e**) and 200 nm (**c**, bottom)

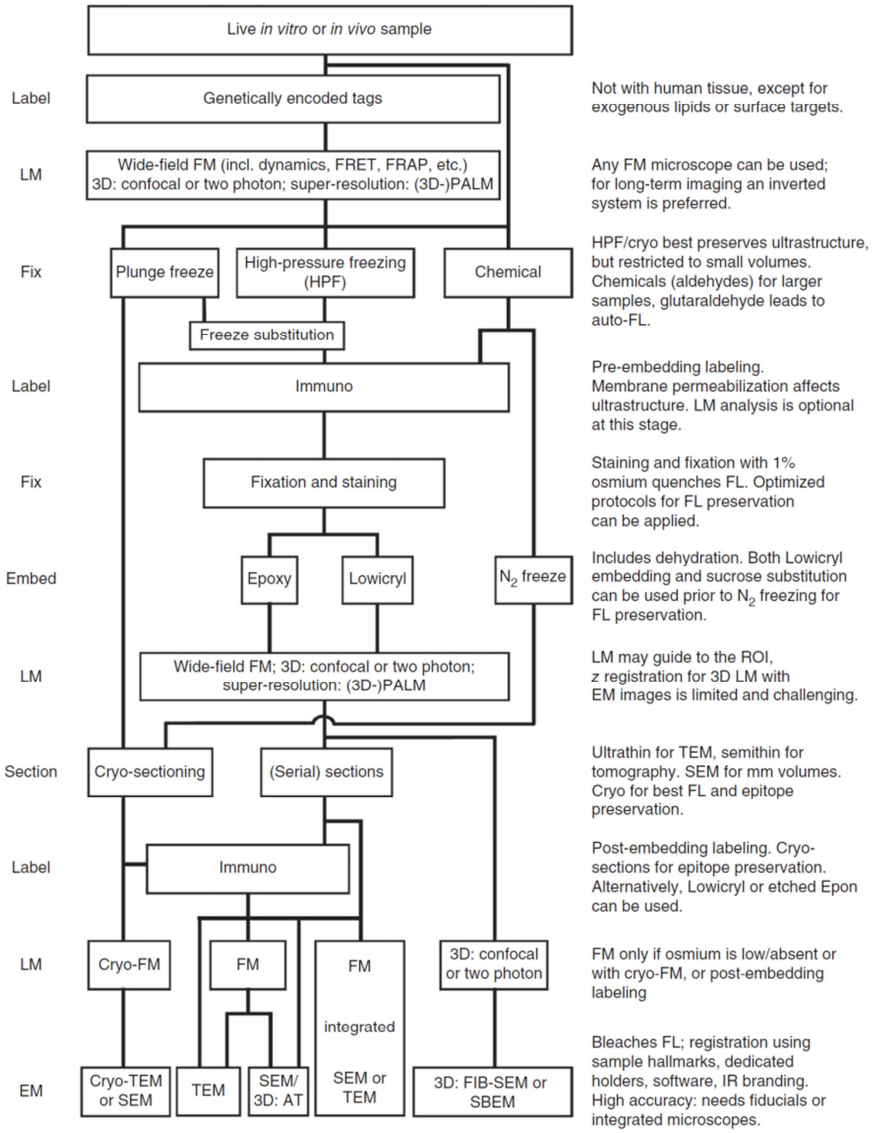

Figure 3 | CLEM procedures and considerations. A single flowchart for the numerous diverse CLEM applications cannot be given. The general layout is depicted (left), emphasizing considerations on the sample under study, preparation and preservation, as well as reagents and microscopes available (right). When choosing a certain trajectory (center), we recommend starting from previous achievements within the same field or from work that used the techniques of choice (S**upplementary** T**able 1**; references throughout the text). FRAP, fluorescence recovery after photobleaching; AT, array tomography; FL, fluorescence; IR, infrared.

***High-precision overlay*.** For image overlay with accuracy better than 0.5 µm, fiducial markers identifiable in both LM and EM are needed. Several types of particles have been used for this purpose, including nanoparticles[25, 26], quantum dots (QDs)[27] and polymer beads[6]. The use of multiple different fiducials may help cover different scales or account for chromatic distortions in multicolor microscopy[28]. Fiducials may be an integrated part of the sample (**Fig. 2a–c**) but are often only added for image registration. To preserve sample integrity, researchers can embed fiducials in a thin top layer below the sample[29] or create them with electron beam patterning[30]. However, in all these approaches, the overlay precision is limited by distortions introduced in the intermediate EM preparation steps.

***Integrated microscopy*.** Following initial development in the 1980s[31], commercial systems for integrated microscopy have appeared recently (**Fig. 4**). Integrated microscopes circumvent issues with ROI retrieval and registration markers, allowing inspection for rare events by LM and then EM analysis directly after. Because samples are not transferred between FM and EM acquisition, they should be both fluorescent and suitable for EM. As all preparation must therefore be done before inspection, sample distortion between FM and EM inspection is not an issue for the overlay image. FEI's iCorr, based on the iLEM prototype[32], is a single-color wide-field fluorescence microscope inside a transmission electron microscope (TEM). An objective lens with long working distance and low numerical aperture is placed between the pole pieces of the TEM lens. The fluorescence microscope

serves to identify an ROI for TEM inspection on the basis of fluorescence. The sample is then rotated for TEM acquisition (**Fig. 4a**). The custom-made iLEM2 allows cryogenic examination of biosamples[16]. Delmic's SECOM is an inverted fluorescence microscope that can be retrofitted to a scanning electron microscope (SEM) such that the objective lens is below the sample, paraxial to the SEM (**Fig. 4b**). The SEM can then be used anywhere within the FM field of view (FOV)[10,15,31]. In the atmospheric SEM (ASEM, or Jeol's ClairScope)[33, 34] and similar systems[35], the fluorescence microscope and SEM are also positioned in paraxial configuration, but with the SEM inverted. Only back-scattered electrons can be detected through a thin (50- to 100-nm) silicon nitride membrane[36, 37], which seals the SEM vacuum chamber (**Fig. 4c**). The sample and the fluorescence microscope are both kept under atmospheric conditions, typically using water-dipping objectives. The lateral size of the membrane limits the observable area to several hundreds of micrometers[36, 37]. Atmospheric inspection has been taken one step further in B-nano's airSEM, in which the sample is physically separated from the membrane vacuum seal[38, 39] (**Fig. 4d**). As the sample is mounted on a translation stage, the observable area can be square centimeters. The fluorescence microscope or other systems, such as an atomic force microscope, can be positioned along the translation stage to allow correlative inspection with automated translation of an ROI between microscopes. Depending on the goal and the microscope setup within reach, a proper choice of probe should be made, as addressed below.

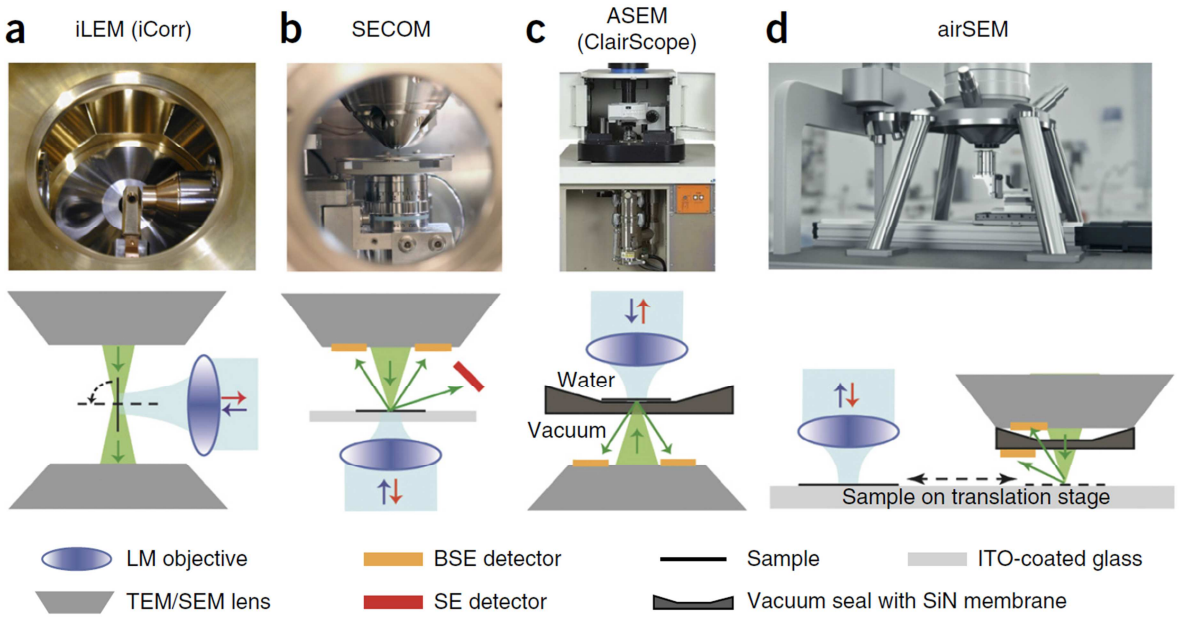

Figure 4 | Commercial integrated CLEM microscopes. The integrated systems (top) and schematic configuration (bottom) are shown. (**a**) The iLEM, commercialized as the iCorr, comprises an integrated FM microscope in a TEM. Optical imaging is followed by sample rotation for TEM acquisition. (**b**) SECOM has an integrated FM microscope in an SEM and inverted FM objective underneath the sample holder paraxial to the SEM column. (**c**) ASEM, commercialized as the ClairScope, has an FM microscope and SEM in paraxial configuration, with the FM microscope and sample under atmospheric conditions, sample cultured on a silicon nitride membrane with inverted SEM column underneath. (**d**) With airSEM, the sample is mounted on a translation stage for FM and scanning EM separated from the silicon nitride membrane; therefore, the electron beam travels a short distance through air. SE, secondary electrons; BSE, back-scattered electrons; ITO, indium tin oxide. Photographs reproduced from ref. 32, Elsevier (**a**); ref. 31, Wiley and the Royal Microscopical Society (**b**); Jeol Ltd. (**c**); and B-nano Ltd. (**d**).

Probes for CLEM

Specific probes in microscopy typically consist of an affinity-based or genetically encoded targeting part, which identifies the protein of interest, linked to a label that is used for detection. CLEM has been pioneered by overlaying fluorescence images on top of the same region imaged by EM. All fluorescent markers available, including FPs, can be used to perform this kind of CLEM. This allows users to identify the underlying ultrastructure of the fluorescence label (**Figs. 2** and **5**). Higher-precision localization of the target proteins can be obtained by also visualizing the probe with EM through, for example, a sequential labeling step such as immunogold detection of GFP. Over the past two decades, probes, tags and other approaches have been developed to visualize molecules in both LM and EM (**Fig. 5**). These can be applied to the samples in either a pre-embedding or a post-embedding step.

A major advantage for immune-targeted affinity approaches is that they can be used to detect endogenous molecules in many contexts, including human tissue. However, fixation and permeabilization of cells to allow entrance of reagents is a prerequisite for these approaches, and these may cause obvious changes at the ultrastructural level[1]. Genetic tagging allows for non-invasive labeling, thereby opening the door to a range of live-cell imaging applications[40, 41], and is typically compatible with strong fixation to retain cellular systems intact, if fluorescence of the tag need not be retained[1]. Post-embedding immunolabeling of GFP with electron-dense particles, such as gold, can introduce EM contrast[13], but epitope availability upon EM preparation is often compromised[1]. Sequential LM and EM contrast can also be introduced in the form of osmiophilic diaminobenzidine (DAB) polymers, with polymerization induced by photo-oxidation, or enzymatically by peroxidases, as explained below. The benefit of CLEM is that fluorescence does not obscure any ultrastructural detail, whereas labeling with heavy metals (DAB, osmium or immunogold, or QDs) by definition will locally add label intensity to the original structural EM contrast (see, for example, the QDs in **Fig. 2c** versus fluorescence in **Fig. 2e**). We discuss the specific properties of the various probe types in more detail below.

Genetically encoded probes for pre-embedded labeling

***Photo-oxidation*.** In the vicinity of a fluorophore, molecular dioxygen can be converted to singlet oxygen via excited-state energy transfer[42]. Upon addition of DAB, this singlet oxygen locally oxidizes the DAB, resulting in polymerization. Enhancement of DAB polymers with osmium creates an electron-dense label. Photo-oxidation has been pioneered using injected Lucifer yellow to label entire neurons[3]. Since then, molecules have been targeted using labeled lipids[43] or with antibodies[2].

The first genetically encoded system for CLEM using photo-oxidation was the tetracysteine tag, which could be incorporated into the protein of interest and then complexed with the biarsenical ReAsH; this approach has allowed for dynamic multicolor pulse-chase analysis, wherein a green dye is bound to all proteins of interest present. After washing and allowing time for new protein synthesis, the new, unlabeled, protein can then be identified by adding red dye. Because, in this case, only the red dye is photoconverted, the pulse-chase experiments allow for spatiotemporal analysis of the protein in EM[44] (**Fig. 5b**). However, improvement of other probes, including photoactivatable FPs that can also be used for pulse chase[45] (**Fig. 5d**), has limited the broad implementation of tetracysteine tagging, which is now used mainly when a small tag is needed to avoid interference with protein function. Also, synthetic fluorophores bound to genetically encoded tags (such as HaloTag and Snap-tag) are used for pulse chase[46], sometimes even allowing fluorescence

preservation after embedding[47]. Finally, the mini singlet oxygen generator (miniSOG) system has been engineered as an entirely genetically encoded photo-oxidation CLEM probe[48, 49] (**Fig. 5c**). A limitation of photo-oxidation is the requirement for light irradiation, which limits the volumes that can be analyzed and may be problematic for imaging thick tissues and organisms.

***Peroxidases*.** Enzymatic DAB conversion by horseradish peroxidase (HRP) conjugated to antibodies has been widely used for labeling in EM[50]. However, implementation of genetically targeted HRP is limited to labeling proteins within the secretory route[51-53] because the active site of HRP does not form in the reducing environment of the mammalian cytosol. To bypass this limitation, researchers monomerized the cytosolic heme-dependent ascorbate peroxidase (APX), a plant homodimeric oxidase, and the active site was optimized for efficient DAB conversion, resulting in enhanced APX (APEX)[54] (**Fig. 5e**). APEX targeted to different cellular compartments, including the cytosol, nucleus and mitochondria, provides EM contrast[54]. However, expression levels of APEX that allow detectable DAB conversion have toxic side effects[55]. Improved APEX (APEX2) with higher DAB-conversion capability was developed[55] that can be used in lower concentrations to visualize targets, thus preventing cellular toxicity. APEX has also been combined with GFP tagging of connexin43 (ref. [54]; **Fig. 5e**), providing a powerful probe for CLEM. APEX2 and miniSOG may also be targeted to proteins of interest using fluorescently labeled single-chain antibodies—as pioneered with 'fluobodies'[56], which are fusions of single-chain variable fragments and GFP—although the use of fluobody-like approaches for CLEM remains to be demonstrated[57].

***Metal tagging*.** Metallothionein and ferritin can be used as genetically encoded EM probes that bind to exogenously added metal atoms to form electron-dense clusters[58, 59]. Implementation of these probes is uncommon because cells are grown under toxic, metal-rich conditions. Although metal tagging is usually applied in bacteria, which are more tolerant to heavy metals[59, 60], this technique recently succeeded in mammalian cells for which a reduced metal-incubation time was used to prevent cellular toxicity[61].

Non-genetically encoded probes for pre-embedding labeling

Particles that are identifiable in EM but that are not genetically encoded, such as gold nanoparticles and QDs, can also be delivered to living cells. These may be taken up by cells: for example, by phagocytosis of nanoparticles or by endocytosis of ligand-bound particles. Alternatively, cells may first be more mildly fixed and permeabilized to immunolabel proteins inside[50], which can be beneficial for retaining epitopes or labeling in a 3D volume. However, good preservation of ultrastructure—a major benefit of pre-embedding labeling—is lost without strong fixation or when samples are permeabilized. Mild fixation and permeabilization can also lead to protein extraction or relocalization[1]. Typically, immunolabeling is performed after embedding of samples.

Post-embedding labeling for fluorescence in EM sections

With post-embedding labeling, fluorescence can be added directly on the EM-embedded sections via immunolabeling (**Fig. 3**), but the antigenicity of target proteins can be compromised as a consequence of fixation with glutaraldehyde and resin infiltration. Post-embedding immunolabeling on EM sections can also be performed using the cryo-based Tokuyasu method optimized for CLEM[13]. With the Tokuyasu method, samples are fixed with aldehydes, dehydrated using sucrose as a cryoprotectant and frozen in liquid nitrogen in order to allow ultrathin cryo-sectioning. Subsequently, sections are thawed for immunolabeling. Of all the immunolabeling approaches, generally the Tokuyasu method is used because it yields good morphology and epitope presentation and is relatively easy to use. An advantage of using ultrathin (~60-nm) sections is that fluorescence is

emitted with better *z* resolution than those attainable with optical techniques such as confocal microscopy[24, 62].

As a more advanced but also more time-consuming technique (sample preparation takes >1 week), high-pressure freezing (HPF) followed by freeze substitution (FS) and either plastic embedding or the Tokuyasu procedure may also be applied. This typically provides better preservation of ultrastructure and epitopes[63] than traditional chemical fixation, including Tokuyasu alone and epoxy embedding. In the case when pre-embedding FPs have been used, HPF-FS best preserves fluorescence. Sections may then be immunolabeled with FluoroNanogold and QDs, which are well-suited for combinatorial CLEM (**Fig. 5f**), although FluoroNanogold may require silver enhancement to increase EM contrast after FM acquisition[23, 50]. The size-dependent emission spectra of QDs allow up to three targets to be distinguished at both the LM and EM levels[4]. The number of identifiable targets may be increased using shape-diverse nanoparticle probes[64] or by combining different probes. QDs can also be used for analysis of metal replicas when studying cell surface molecules or structures underneath the plasma membrane after either extraction by detergents or use of an ultrasonic burst—so-called unroofing of cells—to expose the adherent membrane[26, 65].

Super-resolution fluorescence CLEM

A major limitation of localization of molecules by LM is the diffraction limit of light, which precludes localization at the biomolecular (i.e., nanometer) scale. A number of super-resolution techniques have been developed that allow localization with resolution below 50 nm, approaching EM scales[66, 67]. Super-resolution techniques either (i) exploit shaped illumination beams that control depletion or saturation of molecular fluorescence energy levels or (ii) use stochastic or photoactivated switching of fluorophores in wide-field FM followed by post-acquisition localization. However, as with diffraction-limited microscopy, only labeled proteins or structures are visible in super-resolution FM, leaving the necessary cellular context in the dark. The first approaches to study this cellular context used sequential super-resolved FM and EM[68] (**Fig. 6**). FP photoactivation–based super-resolution CLEM on thin sections requires preservation of FP fluorescence during sample preparation for EM. Several approaches to achieve preservation have been reported. The first is to reduce the osmium tetroxide (OsO_4) concentration to a level that prevents fluorescence quenching but still provides sufficient membrane fixation and contrast, and to also optimize the embedding resin for fluorescence preservation[8]. This approach was used with both PALM (photoactivated localization microscopy) [68] and STED (stimulated emission depletion)[8, 9]. Imaging was later improved using HPF and further uranylacetate staining after PALM to improve SEM contrast[9]. The second approach is to perform PALM, or STORM (stochastic optical reconstruction microscopy)[69], after Tokuyasu sectioning and to increase EM contrast of the sections after PALM with OsO_4 (refs. [25, 29]). Most recently, preservation of the fluorescence and photoswitching properties of the FP mEos4 was achieved after 0.5–1% OsO_4 treatment and resin embedding[11]. Cryofixation prevents fluorescence quenching and has been exploited for super-resolution CLEM. To avoid laser-induced heating during fluorescence imaging and subsequent ice crystallization within the sample, researchers have used cryoprotectants and pulsed laser illumination to allow heat dissipation[70]. Another concern for cryo-PALM is the reduced photoactivation and photobleaching rates under cryogenic temperature (80 K) conditions. So far, only photoactivatable GFP has been seen to retain its photoswitching capability under cryogenic conditions[70], and unless new photoactivatable FPs are developed, multicolor cryo-PALM is beyond reach.

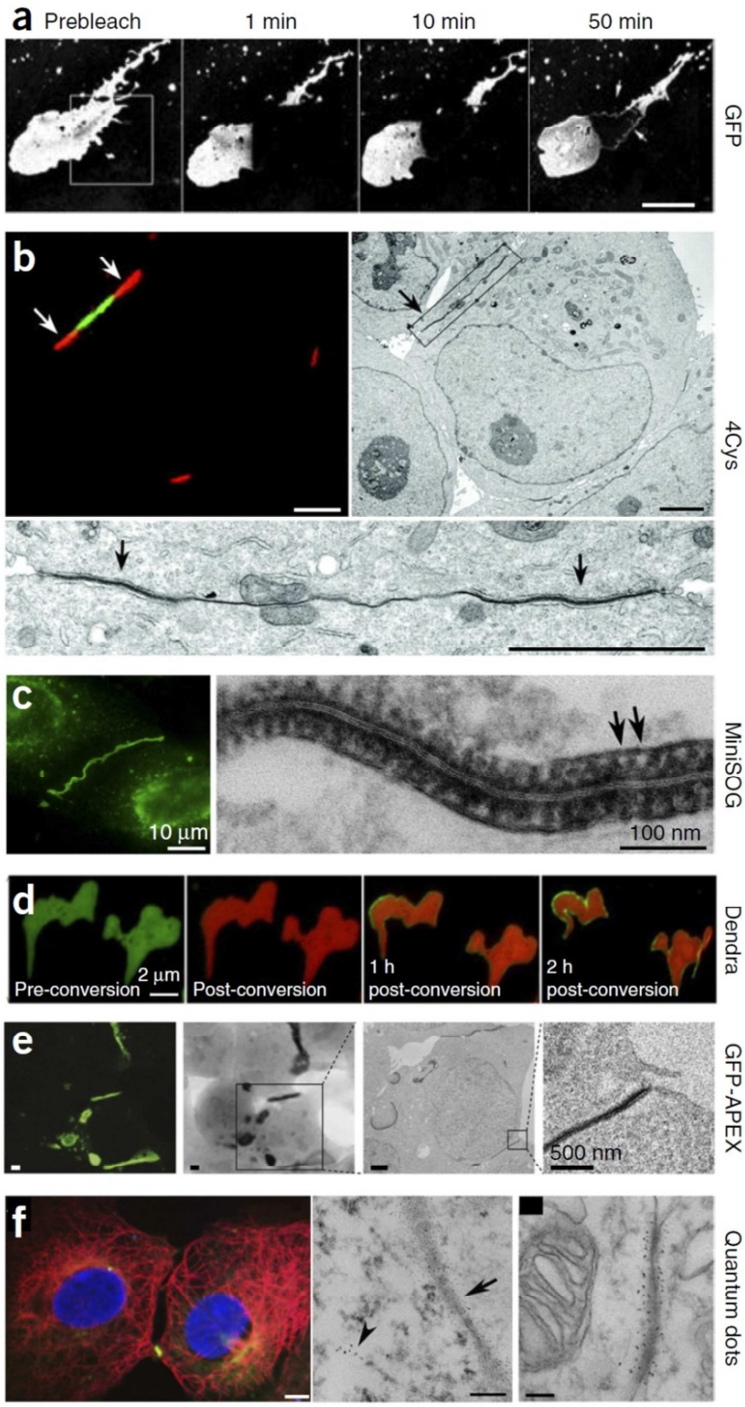

Figure 5 | **Cx43 as a 'guinea pig' in CLEM probe development**. Cx43 (connexin 43) forms gap junctions that allow diffusion of small molecules between cells. (**a**) Fluorescence recovery after photobleaching of GFP-tagged Cx43 revealed that gap junctions are reconstituted from the periphery. (**b**) Top left: tetracysteine-tagged Cx43 was labeled with FlAsH (green) for 4 h, and then newly synthesized protein was labeled with ReAsH (red) to reveal the same result. In this case, the older protein is not photobleached, and photoconversion of ReAsH allows for imaging with CLEM (top right). A concentrated precipitate of osmiophilic DAB polymers is present only at the edge of the gap junction (bottom), indicated with arrows. Note that four point mutations allow tetracysteine-labeling of Cx43 (ref. 111). (**c**) MiniSOG-tagged Cx43 allows for fluorescence inspection (left) followed by photoconversion and EM examination (right). Arrows indicate single connexons. (**d**) Pulse-chase analysis with photoactivatable FPs. Following expression (far left), conversion (center left) and chase for 1 h (center right) to 2 h (far right), gap junction plaque growth is detected at the periphery. With functional photoactivatable FPs in EM sections, the newly synthesized protein could be localized with high precision. (**e**) Imaging of Cx43 with APEX. APEX does not need an affinity step, nor photoconversion, for Cx43 analysis using EM. For LM analysis, a GFP tag was used in tandem, making the complete tag larger than Cx43. (**f**) Endogenous Cx43 (green; arrow) visualized with QDs and counterstained with QDs for microtubules (red; arrowhead) and Hoechst (blue). In cell culture the ultrastructure is affected by permeabilization and milder fixation compared to in the genetic approaches in **a**–**e**. However, tissue analysis with immunolabeling is most generic and most straightforward (right, mouse cerebellum). Scale bars: 3 µm (**a**), 0.5 µm (**b**), 1 µm (**f**, FM), 0.1 µm (**f**, EM). Images reproduced from ref. 112, copyright (2002) National Academy of Sciences, USA (**a**); ref. 44, AAAS (**b**); ref. 48 (**c**); ref. 45 (**d**); ref. 54, Nature Publishing Group (**e**); ref. 113, Springer (**f**, left and center); and ref. 4, Nature Publishing Group (**f**, right).

Matching scales and volumes

Whereas super-resolution FM is moving LM resolution toward that of EM, progress in large-scale and 3D EM[71] has further bridged the two microscopy modalities (**Fig. 1**). EM data are typically represented as snapshots of cells or structures of interest with high resolution. This intrinsically restricts the FOV of the resulting image, which can, however, be overcome by manually stitching these snapshots together. Only recently, specific protocols have been developed to allow 2D automated TEM acquisition and stitching of areas up to 1 mm^2 at macromolecular resolution[52, 72, 73], an approach also referred to as nanotomy (for nano-anatomy; http://www.nanotomy.org/). With scanning-based detection (scanning EM), even larger FOVs (for example, 32,000 × 32,000 pixels) can be acquired with quality similar to that of transmission EM[74, 75]. Analysis of these large data sets remains a bottleneck; this is still typically done by manual annotation, sometimes by many people[76]. In the future, automated data analysis will be guided by, and benefit from, applying CLEM to identify cellular or subcellular details or molecules.

Improvements in throughput of EM in the *z* direction are also critical for development of 3D CLEM. Volume reconstructions with EM[77] can be achieved with array tomography using serial sections[62] but also with serial block-face scanning EM (SBEM)[78] or focused-ion-beam scanning EM (FIB-SEM)[77]. With the latter two techniques, the upper surface of the sample is imaged and is then removed using an integrated ultramicrotome (SBEM) or an ion beam (FIB-SEM); this is followed by another imaging step, and the process is repeated until the entire sample is imaged. A similar procedure has recently been used in LM to allow *ex vivo* FM of a whole mouse brain[79] by combining block-face imaging using two-photon excitation and subsequent removal of the acquired area with an ultramicrotome to access the next section. FIB-SEM has also been used to sculpt thin lamellae out of a 3D block for electron tomography[80]. Both SBEM and FIB-SEM can potentially be combined with CLEM.

Although a comprehensive review of 3D methods is out of the scope of this manuscript, common 3D CLEM approaches are (i) pre-embedding FM before EM processing and 3D analysis using either serial sections or block-face methods[81-83]; (ii) post-embedding labeling of serial sections[23, 62]; and (iii) preservation of fluorescence upon EM preparation, either for serial sections (**Fig. 2d**,**e**) or for *en bloc* confocal microscopy followed by SBEM or FIB-SEM[21, 23, 83] (**Fig. 3**). With both pre-embedding and *en bloc* FM, fluorescence resolution along the *z* axis is limited (~1 µm). When serial ultrathin (40- to 100-nm) sections are labeled[62], this is improved to the section thickness. For samples prepared cryogenically to preserve FP fluorescence[6, 7, 10, 12, 16], integrated serial 3D CLEM using EM sections allows simultaneous matching of multiple FM and EM scales (**Fig. 2d**,**e**) both toward higher FM resolution and larger EM volumes, thus narrowing the volume gap in CLEM (**Fig. 1**). This enables diffraction-limited analysis of volumes of ~1 cm^3 by LM[79, 84] and several cubic millimeters by EM. Note that scanning these volumes will take typically several hours to weeks, mainly depending on the voxel size and volume imaged.

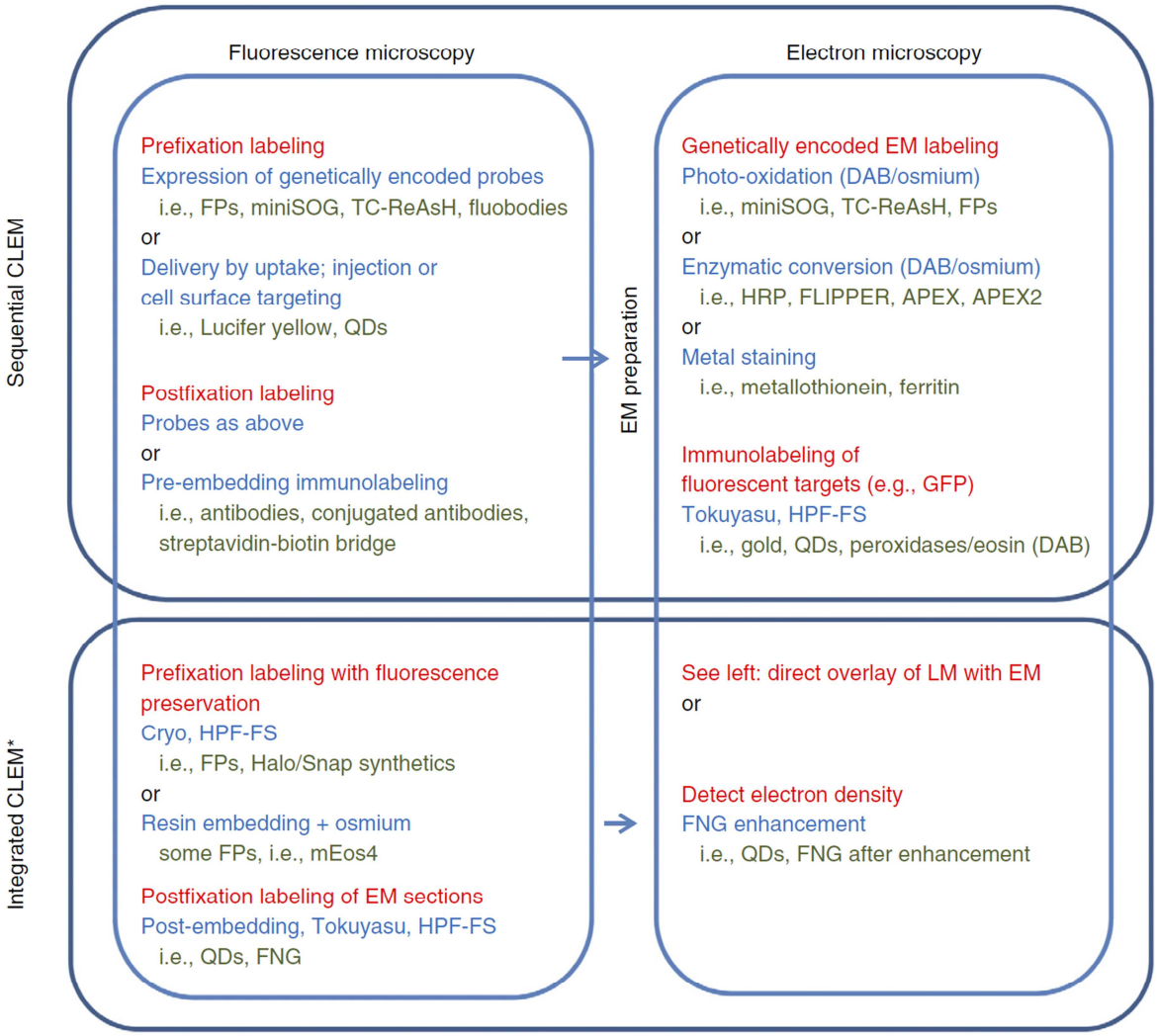

Figure 6 | **Sequential versus integrated CLEM**. Labeling and preparation approaches compatible with sequential (top) or integrated (bottom) CLEM inspection are compared. FM (left) is generally performed before EM (right). The opportunities have been grouped according to approaches (red); where sample preparation or labeling method (blue) and the choice of the right probes (green) is crucial to reach one's goal. *All samples for integrated microscopy can be used for sequential CLEM. FNG, FluoroNanogold.

Guidelines, tips and tricks

Human tissue

The most versatile method to target endogenous proteins within human tissue is immunolabeling. The major question is whether to perform the labeling pre-embedding or post-embedding or to use a combination of methods. Pre-embedding labeling with an antibody with a small fluorophore permits 3D or large-area FM and may also be used for super-resolution FM. In pre-embedding labeling, label penetration is an issue and will typically require permeabilization, relatively mild fixation (no or low glutaraldehyde) and prolonged incubation to get reagents inside[1]. The penetration efficiency

depends on which tissue is probed, which permeabilization reagents are used and the size of probes. Whereas antibodies conjugated to small fluorophores or to HRP will typically penetrate tens of micrometers, larger particles such as QDs will be limited to several micrometers, and immunogold will not penetrate at all[4].

Post-embedding labeling may be a better option when the ROI does not require prior FM-based examination and selection or when colloidal gold is being used. The limiting step here is typically antigen recognition by the antibodies. Cryo-EM and Tokuyasu labeling is still the gold standard for identifying targets[13]. In addition, plastic-embedded material may be etched and subsequently used for immunolabeling (**Fig. 2**). The major decision will depend on what approach preserves epitope recognition, which typically needs to be addressed empirically—for example, by testing multiple antibodies against the same target, as they may react completely differently. As for pre-embedding labeling, the use of non-optimal concentrations of glutaraldehyde to preserve ultrastructure may help to retain antigenicity. Detection can then be achieved using labels visible by both FM and EM, such as QDs or FluoroNanogold. If LM is needed for a study but a fluorescence signal is not additive, consider using conventional histochemistry or nonfluorescent labels that are readily identifiable with LM, such as detection of colloidal gold using reflection microscopy or deposition of osmiophilic DAB polymers using HRP-conjugated antibodies. In select cases research is performed on *ex vivo* living human material, which allows for genetically encoded tag delivery using transfection or transduction or by mechanical means (such as microinjection of material or gene gun–based delivery)[85].

Nonhuman tissue

In principle, all approaches discussed for human tissue can be used—and one is usually limited to these approaches—when studying endogenous proteins in nonhuman samples as well. A major benefit of using tissue samples from organisms that can be genetically modified, however, is the ability to use genetically encoded tags (**Supplementary Table 1c**). For CLEM of genetically modified organisms, overlaying the FP signal with EM, or the Tokuyasu-FP combination discussed above, is most commonly used.

Mammalian cell culture

Mammalian cells under *in vitro* culture conditions are well suited for immunobased approaches, especially to detect endogenous proteins. Alternatively, genetically encoded probes can be introduced. Genetically encoded CLEM probes, such as tetracysteines[86], APEX2[55], HRP[53] or miniSOG[48] fused to FPs, are suitable for live-cell imaging followed by EM analysis; ultrastructural preservation is uncompromised owing to the use of high glutaraldehyde and osmium concentrations[44, 48, 53, 55, 86]. Mammalian cells are also used in super-resolution FM followed by overlay with EM, for example with PALM[68], including the use of the optimized photoswitchable Eos4 protein[11]. With optimized protocols for fluorescence retention in thin sections, including the aforementioned cryotechniques[6, 7, 10, 12], sample preparation resulting in deformation is no longer needed. This makes image registration less troublesome, and the samples may be used in integrated systems.

Microorganisms and viruses

For microorganisms such as yeast, bacteria and viruses, high resolution, but not tissue context, is typically needed, precluding the need for large FOVs. Imaging such microorganisms may be achieved by all CLEM approaches discussed above. In addition, bacteria have been used to pioneer toxic regiments such as metal tagging[59, 60]. The small size of microorganisms makes them well suited for cryo-EM[59]. In some cases, the size of introduced genetically encoded tags may raise issues, in

addition to problems that may arise from protein fusion and overexpression. For small, compact units, such as viruses, the use of peptide tags[87] may be preferred over protein tags to allow a normal life cycle.

Hardware

On the basis of the sample-preparation approach, one may be bound to sequential acquisition or instead have a choice between sequential or integrated CLEM (**Figs. 3** and **6**). When tissue samples are evaluated with sequential acquisition, it may not be necessary to turn to fiducials or finder grids if submicrometer overlay accuracy is not needed. Instead, during LM, pay attention to structures such as blood vessels or nuclei to help relocate the ROI, or turn to automated commercial solutions (see above: Data acquisition and overlay). When fluorescence is used, we recommend a nuclear stain, such as Hoechst or 4',6-diamidino-2-phenylindole (DAPI), which will help to locate the nuclei in FM, as these organelles are easily recognized in EM (**Fig. 2**). For cellular samples, it is advisable to use marked grids or any of the available commercial systems for ROI retrieval. If an integrated approach is feasible, this may speed up acquisition time and improve throughput, but it imposes restrictions on the available sample-preparation techniques that need to preserve fluorescence and restricts FM and EM modalities to those present in the integrated system. iCorr is the only system available for TEM inspection, whereas SECOM fits with a current trend toward SEM use in biological applications, notably in high-content EM. Sample translation systems (iCorr or airSEM) need fiducials for high-accuracy overlay; in paraxial systems (SECOM or ClairScope) these can be omitted. In the SEM systems, the fluorescence microscope can be relatively freely operated, which may make the need for an advanced stand-alone microscope redundant. Also, systems such as airSEM and SECOM can be used upstream of other approaches, allowing additional results to be obtained[39, 88] (**Fig. 6**). The ClairScope seems most suitable for inspection of cells in culture medium, staying close to live-cell FM. Importantly, although it is feasible to image live cells with these systems, it should be noted that electron irradiation during EM is highly toxic and will kill the cells. Nevertheless, this and other possibilities offered by integrated microscopes may provide novel roads for CLEM development.

Opportunities, considerations and limitations

CLEM adds resolution and cellular context to LM observations and adds dynamics and target identification to EM observations. Super-resolution LM techniques need EM to provide context to either pointillist PALM images[8, 11, 25, 29, 68] or STED data[8]. As a result, experiments based on CLEM are beginning to provide insight in several biological contexts.

For instance, gap junction turnover using pulse-chase labeling combined with dynamic imaging revealed the growth of these channels from the outside of the plaque at the EM and LM level (**Fig. 5** and references therein). Also, surprising variation in nuclear pore symmetry has been uncovered by applying fluorescence for quantification in a CLEM approach[89]. Similarly, not only the birth of the Golgi apparatus[86] but also trafficking of Golgi intermediates as tubular-saccular structures[90] have been clarified using LM dynamics and EM resolution in CLEM. The approach is also being used to study biology at the tissue level, such as understanding the sub-diffraction-limited connections in neuronal networks[91].

As CLEM paves the way for adding dimensions to data sets, choices for CLEM (**Fig. 3**) should be made according to the kind and size of material, whether pre- or post-embedding labeling applies,

epitope recognition, and/or availability of genetically encoded tags. Thus, implementation of CLEM is guided by several considerations—mainly based on the research question at stake and models available, as well as access to microscopes. The benefits and limitations in a CLEM workflow are highlighted in **Figure 3** and discussed in more detail in earlier paragraphs. As a starting point, we suggest implementation of CLEM techniques used by others in the same research field or using similar models (**Supplementary Table 1** and references therein).

Future outlook

Probes and live-cell electron microscopy

In most genetically encoded approaches, the protein of interest is tagged and overexpressed, which may cause artifacts. Efforts to minimize such artifacts are ongoing: detrimental effects of genetically encoded tags may be prevented by improving their photophysical properties, thus requiring fewer labeled molecules to visualize targets, as shown with APEX2 improvement over APEX in cells[55]. Recently, fluorescence preservation of the newly developed photoactivatable FP mEos4 was shown[11]. With new targeted gene-modification tools such as the CRISPR (clustered, regularly interspaced, short palindromic repeats)-Cas9 system[92], the introduction of genetically encoded tags on endogenous proteins is becoming increasingly feasible. Further developments in fluobodies and the metallothionein approach are also being explored[61].

Cryo-EM comes the closest to imaging samples in a state similar to that observed with live-cell FM; however, the time needed for vitrification reduces FM-EM temporal correlation. Systems for rapid freezing of small samples during live-cell observation are in development[93]. Alternatively, liquid EM, in which ultrastructural analysis on cells in their original state is performed, is also being developed. In this approach, cells are cultured in a microfluidic chamber containing silicon nitride membranes that allow the electron beam to pass. Gold-conjugated ligand-receptor interactions over the complete cell surface have been observed with liquid scanning transmission EM[94]. The ultimate future perspective with combined FM and scanning EM in liquid would be to correlate live-cell imaging directly with an ultrastructural snapshot, the recording of which will deliver a lethal dose to the system under study. Liquid CLEM can be conducted by quickly transferring the microfluidic chamber between microscopes[95], but instrumentation for integrated liquid CLEM, to match the EM snapshot with FM acquisitions in time, is also emerging[34].

Development of vital EM probes would benefit CLEM not only for ‘wet’ EM but also for intravital applications. For instance, multiphoton microscopy, which achieves relatively deep penetration, may be used for intravital imaging of animal models and correlated to a later acquired EM image[96, 97]. Improvements of intravital FM—including fast, high-throughput 3D fluorescence imaging approaches such as light-sheet microscopy[84]—may be applied, and relocating ROIs using laser-based marks (‘tattooing’)[96] will be important for intravital CLEM. With EM, structural information within whole living organisms can be obtained, as has been applied to study zebrafish[98-100], mouse neuronal circuits[101] and tumor cell invasion in mice[97].

Hardware and software solutions

High-content EM imaging (large FOV, high resolution, 3D) is still limited by acquisition time. Although obtaining serial sections for 3D imaging has been facilitated by developments such as an automatic tape-collecting microtome[102], and although, with SBEM and FIB-SEM, serial sectioning may be

bypassed, faster approaches for data collection are still needed and are ongoing. For instance, multibeam scanning EM[103, 104] and multi-energy deconvolution scanning EM[103] lead to an increase of at least one order of magnitude in acquisition speeds. High-content machines typically run 24/7, thereby limiting the number of samples that can be analyzed. Although application of high-content 2D and 3D CLEM is increasing, software development for reconstruction and analysis is required. In order to obtain high-content CLEM data, where the extent of EM analysis matches the FM scale, researchers can apply large-scale 2D and 3D EM reconstruction approaches. For recognition of EM structures, semiautomated software is being developed, such as Ilastik[101] and TrakEM2 (ref.[105]), but a routine automated solution is not available yet.

Closing the mesoscale gap

A recent development in 3D imaging is the application of soft X-ray microscopy to biological samples[106, 107]; 40-nm^3-resolution images with a lateral FOV of 20 µm and 10-µm depth have been obtained using this approach. By correlating soft X-ray microscopy with FM, researchers could image endosomes and phagosomes in cryofixed cells with high resolution[108]. Further correlation with high-magnification EM will create another way to cross scales from large-volume whole-organism FM to ultrastructural EM detail. In addition, integrated microscopes allow for cathodoluminescence (CL) examination, with which EM beam excitation of a probe results in light emission[109]. The emitted light spot can be correlated to the position of the electron beam, providing optimal simultaneous CLEM and making it possible to define the underlying structure. Application of this method will require biofunctionalization of CL probes, which should be pioneered in fixed specimens. Nanoparticles with distinct CL emission spectra[109] and CL protocols[110] will aid in future application of CL-CLEM in the biosciences.

Concluding remarks

Imaging molecules in time and 3D space has transformed LM into a powerful biological research tool. With the development of combinatorial probes, tags, approaches and microscopes—including integrated systems—for CLEM, these experiments can be further put in their ultrastructural context. In parallel, super-resolution fluorescence techniques have moved FM resolution, now up to 20 nm, toward that of EM, allowing for higher-resolution localization solely with fluorescent probes. Conversely, with the increasing use of automated transmission EM, scanning EM and automated tiling software, EM acquisition size can match scales with conventional LM in both the planar and *z* directions, providing high-content CLEM images. Given these ongoing developments, we foresee broad implementation and a bright future for CLEM.

Acknowledgments

We thank C.J. Peddie and L.M. Collinson for providing **Figure 2d**,**e** and our departmental members for feedback. We acknowledge financial support for our CLEM work from the Netherlands Organization for Scientific Research (ZonMW91111006; “Microscopy Valley” STW12718 and STW12714; NWO175-010-2009-023), the NanoNextNL innovation programme (09A.04) and a Marie Curie International Reintegration Grant within the 7th European Community Framework Program.

Reference

1. Schnell, U., Dijk, F., Sjollema, K. A. & Giepmans, B. N. Immunolabeling artifacts and the need for live-cell imaging. *Nat. Methods* 9, 152-158 (2012).

2. Deerinck, T. J. *et al*. Fluorescence photooxidation with eosin: a method for high resolution immunolocalization and in situ hybridization detection for light and electron microscopy. *J. Cell Biol.* 126, 901-910 (1994).

3. Maranto, A. R. Neuronal mapping: a photooxidation reaction makes Lucifer yellow useful for electron microscopy. *Science* 217, 953-955 (1982).

4. Giepmans, B. N., Deerinck, T. J., Smarr, B. L., Jones, Y. Z. & Ellisman, M. H. Correlated light and electron microscopic imaging of multiple endogenous proteins using Quantum dots. *Nat Methods* 2, 743-9 (2005).

5. Karreman, M. A. *et al*. Optimizing immuno-labeling for correlative fluorescence and electron microscopy on a single specimen. *J. Struct. Biol.* 180, 382-386 (2012).

6. Kukulski, W. *et al*. Precise, correlated fluorescence microscopy and electron tomography of lowicryl sections using fluorescent fiducial markers. *Methods Cell Biol.* 111, 235-257 (2012).

7. Kukulski, W. *et al*. Correlated fluorescence and 3D electron microscopy with high sensitivity and spatial precision. *J. Cell Biol.* 192, 111-119 (2011).

8. Watanabe, S. *et al*. Protein localization in electron micrographs using fluorescence nanoscopy. *Nat. Methods* 8, 80-84 (2011).

9. Watanabe, S. *et al*. Nano-fEM: protein localization using photo-activated localization microscopy and electron microscopy. *J. Vis. Exp.* (70):e3995. doi, e3995 (2012).

10. Peddie, C. J. *et al*. Correlative and integrated light and electron microscopy of in-resin GFP fluorescence, used to localise diacylglycerol in mammalian cells. *Ultramicroscopy* 143, 3-14 (2014).

11. Paez-Segala, M. G. *et al*. Fixation-resistant photoactivatable fluorescent proteins for CLEM. *Nat. Methods* 12, 215-218 (2015).

12. Nixon, S. J. *et al*. A single method for cryofixation and correlative light, electron microscopy and tomography of zebrafish embryos. *Traffic* 10, 131-136 (2009).

13. van Rijnsoever, C., Oorschot, V. & Klumperman, J. Correlative light-electron microscopy (CLEM) combining live-cell imaging and immunolabeling of ultrathin cryosections. *Nat. Methods* 5, 973-980 (2008).

14. Karreman, M. A. *et al*. Discovery of a new RNA-containing nuclear structure in UVC-induced apoptotic cells by integrated laser electron microscopy. *Biol. Cell.* 101, 287-299 (2009).

15. Liv, N. *et al*. Simultaneous Correlative Scanning Electron and High-NA Fluorescence Microscopy. *PLoS One* 8, e55707 (2013).

16. Faas, F. G. *et al*. Localization of fluorescently labeled structures in frozen-hydrated samples using integrated light electron microscopy. *J. Struct. Biol.* 181, 283-290 (2013).

17. Schorb, M. & Briggs, J. A. Correlated cryo-fluorescence and cryo-electron microscopy with high spatial precision and improved sensitivity. *Ultramicroscopy* 143, 24-32 (2014).

18. van Driel, L. F., Valentijn, J. A., Valentijn, K. M., Koning, R. I. & Koster, A. J. Tools for correlative cryo-fluorescence microscopy and cryo-electron tomography applied to whole mitochondria in human endothelial cells. *Eur. J. Cell Biol.* 88, 669-684 (2009).

19. Sartori, A. *et al*. Correlative microscopy: bridging the gap between fluorescence light microscopy and cryo-electron tomography. *J. Struct. Biol.* 160, 135-145 (2007).

20. Schwartz, C. L., Sarbash, V. I., Ataullakhanov, F. I., McIntosh, J. R. & Nicastro, D. Cryo-fluorescence microscopy facilitates correlations between light and cryo-electron microscopy and reduces the rate of photobleaching. *J. Microsc.* 227, 98-109 (2007).

21. Müller-Reichert, T. & Verkade, P. Methods in Cell Biology. 124, 442 (2014).

22. Spiegelhalter, C., Laporte, J. F. & Schwab, Y. Correlative light and electron microscopy: from live

cell dynamic to 3D ultrastructure. *Methods Mol. Biol.* 1117, 485-501 (2014).

23. Müller-Reichert, T. & Verkade, P. Methods in Cell Biology. 111, 445 (2012).

24. Bishop, D. *et al*. Near-infrared branding efficiently correlates light and electron microscopy. *Nat. Methods* 8, 568-570 (2011).

25. Kopek, B. G., Shtengel, G., Xu, C. S., Clayton, D. A. & Hess, H. F. Correlative 3D superresolution fluorescence and electron microscopy reveal the relationship of mitochondrial nucleoids to membranes. *Proc. Natl. Acad. Sci. U. S. A.* 109, 6136-6141 (2012).

26. Sochacki, K. A., Shtengel, G., van Engelenburg, S. B., Hess, H. F. & Taraska, J. W. Correlative super-resolution fluorescence and metal-replica transmission electron microscopy. *Nat. Methods* 11, 305-308 (2014).

27. Masich, S., Ostberg, T., Norlen, L., Shupliakov, O. & Daneholt, B. A procedure to deposit fiducial markers on vitreous cryo-sections for cellular tomography. *J. Struct. Biol.* 156, 461-468 (2006).

28. Schellenberger, P. *et al*. High-precision correlative fluorescence and electron cryo microscopy using two independent alignment markers. *Ultramicroscopy* 143, 41-51 (2014).

29. Kopek, B. G., Shtengel, G., Grimm, J. B., Clayton, D. A. & Hess, H. F. Correlative photoactivated localization and scanning electron microscopy. *PLoS One* 8, e77209 (2013).

30. Koning, R. I., Kutchoukov, V. G., Hagen, C. W. & Koster, A. J. Nanofabrication of a gold fiducial array on specimen support for electron tomography. *Ultramicroscopy* 135, 99-104 (2013).

31. Zonnevylle, A. C. *et al*. Integration of a high-NA light microscope in a scanning electron microscope. *J. Microsc.* 252, 58-70 (2013).

32. Agronskaia, A. V. *et al*. Integrated fluorescence and transmission electron microscopy. *J. Struct. Biol.* 164, 183-189 (2008).

33. Nishiyama, H. *et al*. Atmospheric scanning electron microscope observes cells and tissues in open medium through silicon nitride film. *J. Struct. Biol.* 169, 438-449 (2010).

34. Maruyama, Y., Ebihara, T., Nishiyama, H., Suga, M. & Sato, C. Immuno EM-OM correlative microscopy in solution by atmospheric scanning electron microscopy (ASEM). *J. Struct. Biol.* 180, 259-270 (2012).

35. Nawa, Y. *et al*. Multi-color imaging of fluorescent nanodiamonds in living HeLa cells using direct electron-beam excitation. *Chemphyschem* 15, 721-726 (2014).

36. Ring, E. A., Peckys, D. B., Dukes, M. J., Baudoin, J. P. & de Jonge, N. Silicon nitride windows for electron microscopy of whole cells. *J. Microsc.* 243, 273-283 (2011).

37. Nishiyama, H. *et al*. Atmospheric scanning electron microscope system with an open sample chamber: Configuration and applications. *Ultramicroscopy* 147C, 86-97 (2014).

38. Solomonov, I. *et al*. Introduction of correlative light and airSEM microscopy imaging for tissue research under ambient conditions. *Sci. Rep.* 4, 5987 (2014).

39. Vidavsky, N. *et al*. Initial stages of calcium uptake and mineral deposition in sea urchin embryos. *Proc. Natl. Acad. Sci. U. S. A.* 111, 39-44 (2014).

40. Giepmans, B. N., Adams, S. R., Ellisman, M. H. & Tsien, R. Y. The fluorescent toolbox for assessing protein location and function. *Science* 312, 217-24 (2006).

41. Shaner, N. C. *et al*. Improved monomeric red, orange and yellow fluorescent proteins derived from Discosoma sp. red fluorescent protein. *Nat Biotechnol* 22, 1567-72 (2004).

42. Ogilby, P. R. Singlet oxygen: there is indeed something new under the sun. *Chem. Soc. Rev.* 39, 3181-3209 (2010).

43. Pagano, R. E., Sepanski, M. A. & Martin, O. C. Molecular trapping of a fluorescent ceramide analogue at the Golgi apparatus of fixed cells: interaction with endogenous lipids provides a trans-Golgi marker for both light and electron microscopy. *J. Cell Biol.* 109, 2067-2079 (1989).

44. Gaietta, G. *et al*. Multicolor and electron microscopic imaging of connexin trafficking. *Science* 296, 503-507 (2002).

45. Baker, S. M., Buckheit, R. W.,3rd & Falk, M. M. Green-to-red photoconvertible fluorescent proteins: tracking cell and protein dynamics on standard wide-field mercury arc-based microscopes. *BMC Cell Biol.* 11, 15-2121-11-15 (2010).

46. Jansen, L. E., Black, B. E., Foltz, D. R. & Cleveland, D. W. Propagation of centromeric chromatin requires exit from mitosis. *J. Cell Biol.* 176, 795-805 (2007).

47. Perkovic, M. *et al*. Correlative light- and electron microscopy with chemical tags. *J. Struct. Biol.* 186, 205-213 (2014).

48. Shu, X. *et al*. A genetically encoded tag for correlated light and electron microscopy of intact cells, tissues, and organisms. *PLoS Biol.* 9, e1001041 (2011).

49. Boassa, D. *et al*. Mapping the subcellular distribution of alpha-synuclein in neurons using genetically encoded probes for correlated light and electron microscopy: implications for Parkinson's disease pathogenesis. *J. Neurosci.* 33, 2605-2615 (2013).

50. Sosinsky, G. E., Giepmans, B. N., Deerinck, T. J., Gaietta, G. M. & Ellisman, M. H. Markers for correlated light and electron microscopy. *Methods Cell Biol* 79, 575-91 (2007).

51. Li, J., Wang, Y., Chiu, S. L. & Cline, H. T. Membrane targeted horseradish peroxidase as a marker for correlative fluorescence and electron microscopy studies. *Front. Neural Circuits* 4, 6 (2010).

52. Atasoy, D. *et al*. A genetically specified connectomics approach applied to long-range feeding regulatory circuits. *Nat. Neurosci.* 17, 1830-1839 (2014).

53. Kuipers, J. *et al*. FLIPPER, a combinatorial probe for quantitative correlated live imaging and electron microscopy. *Cell & Tissue Research* 360, 61-70 (2015).

54. Martell, J. D. *et al*. Engineered ascorbate peroxidase as a genetically encoded reporter for electron microscopy. *Nat. Biotechnol.* 30, 1143-1148 (2012).

55. Lam, S. S. *et al*. Directed evolution of APEX2 for electron microscopy and proximity labeling. *Nat. Methods* 12, 51-54 (2015).

56. Rothbauer, U. *et al*. Targeting and tracing antigens in live cells with fluorescent nanobodies. *Nat Methods* 3, 887-9 (2006).

57. Mironova, K. E. *et al*. Genetically encoded immunophotosensitizer 4D5scFv-miniSOG is a highly selective agent for targeted photokilling of tumor cells in vitro. *Theranostics* 3, 831-840 (2013).

58. Mercogliano, C. P. & DeRosier, D. J. Concatenated metallothionein as a clonable gold label for electron microscopy. *J. Struct. Biol.* 160, 70-82 (2007).

59. Wang, Q., Mercogliano, C. P. & Lowe, J. A ferritin-based label for cellular electron cryotomography. *Structure* 19, 147-154 (2011).

60. Diestra, E., Fontana, J., Guichard, P., Marco, S. & Risco, C. Visualization of proteins in intact cells with a clonable tag for electron microscopy. *J. Struct. Biol.* 165, 157-168 (2009).

61. Risco, C. *et al*. Specific, sensitive, high-resolution detection of protein molecules in eukaryotic cells using metal-tagging transmission electron microscopy. *Structure* 20, 759-766 (2012).

62. Micheva, K. D. & Smith, S. J. Array tomography: a new tool for imaging the molecular architecture and ultrastructure of neural circuits. *Neuron* 55, 25-36 (2007).

63. McDonald, K. L. Rapid embedding methods into epoxy and LR White resins for morphological and immunological analysis of cryofixed biological specimens. *Microsc. Microanal.* 20, 152-163 (2014).

64. Philimonenko, V. V. *et al*. Simultaneous detection of multiple targets for ultrastructural immunocytochemistry. *Histochem. Cell Biol.* 141, 229-239 (2014).

65. Collins, A., Warrington, A., Taylor, K. A. & Svitkina, T. Structural organization of the actin cytoskeleton at sites of clathrin-mediated endocytosis. *Curr. Biol.* 21, 1167-1175 (2011).

66. Deschout, H. *et al*. Precisely and accurately localizing single emitters in fluorescence microscopy. *Nat. Methods* 11, 253-266 (2014).

67. Schermelleh, L., Heintzmann, R. & Leonhardt, H. A guide to super-resolution fluorescence microscopy. *J. Cell Biol.* 190, 165-175 (2010).

68. Betzig, E. *et al*. Imaging Intracellular Fluorescent Proteins at Near-Molecular Resolution. *Science* 313, 1642-1645 (2006).

69. Suleiman, H. *et al*. Nanoscale protein architecture of the kidney glomerular basement membrane. *Elife (Cambridge)* 2, e01149 (2013).

70. Chang, Y. W. *et al*. Correlated cryogenic photoactivated localization microscopy and cryo-electron tomography. *Nat. Methods* 11, 737-739 (2014).

71. Patwardhan, A. *et al*. A 3D cellular context for the macromolecular world. *Nat. Struct. Mol. Biol.* 21, 841-845 (2014).

72. Faas, F. G. *et al*. Virtual nanoscopy: Generation of ultra-large high resolution electron microscopy maps. *J. Cell Biol.* 198, 457-469 (2012).

73. Ravelli, R. B. *et al*. Destruction of tissue, cells and organelles in type 1 diabetic rats presented at macromolecular resolution. *Sci. Rep.* 3, 1804 (2013).

74. Kuwajima, M., Mendenhall, J. M., Lindsey, L. F. & Harris, K. M. Automated transmission-mode scanning electron microscopy (tSEM) for large volume analysis at nanoscale resolution. *PLoS One* 8, e59573 (2013).

75. Sokol, E. *et al*. Large-Scale Electron Microscopy Maps of Patient Skin and Mucosa Provide Insight into Pathogenesis of Blistering Diseases. *J. Invest. Dermatol.* 135, 1763-1770 (2015).

76. Briggman, K. L., Helmstaedter, M. & Denk, W. Wiring specificity in the direction-selectivity circuit of the retina. *Nature* 471, 183-188 (2011).

77. Briggman, K. L. & Bock, D. D. Volume electron microscopy for neuronal circuit reconstruction. *Curr. Opin. Neurobiol.* 22, 154-161 (2012).

78. Denk, W. & Horstmann, H. Serial block-face scanning electron microscopy to reconstruct three-dimensional tissue nanostructure. *PLoS Biol.* 2, e329 (2004).

79. Ragan, T. *et al*. Serial two-photon tomography for automated ex vivo mouse brain imaging. *Nat. Methods* 9, 255-258 (2012).

80. Rigort, A. *et al*. Focused ion beam micromachining of eukaryotic cells for cryoelectron tomography. *Proc. Natl. Acad. Sci. U. S. A.* 109, 4449-4454 (2012).

81. Murphy, G. E. *et al*. Correlative 3D imaging of whole mammalian cells with light and electron microscopy. *J. Struct. Biol.* 176, 268-278 (2011).

82. Maco, B., Holtmaat, A., Jorstad, A., Fua, P. & Knott, G. W. Correlative in vivo 2-photon imaging and focused ion beam scanning electron microscopy: 3D analysis of neuronal ultrastructure. *Methods Cell Biol.* 124, 339-361 (2014).

83. Narayan, K. *et al*. Multi-resolution correlative focused ion beam scanning electron microscopy: applications to cell biology. *J. Struct. Biol.* 185, 278-284 (2014).

84. Chen, B. C. *et al*. Lattice light-sheet microscopy: imaging molecules to embryos at high spatiotemporal resolution. *Science* 346, 1257998 (2014).

85. Arsenault, J. & O'Brien, J. A. Optimized heterologous transfection of viable adult organotypic brain slices using an enhanced gene gun. *BMC Res. Notes* 6, 544-0500-6-544 (2013).

86. Gaietta, G. M. *et al*. Golgi twins in late mitosis revealed by genetically encoded tags for live cell imaging and correlated electron microscopy. *Proc Natl Acad Sci U S A* 103, 17777-177782 (2006).

87. Lanman, J. *et al*. Visualizing flock house virus infection in Drosophila cells with correlated fluorescence and electron microscopy. *J. Struct. Biol.* 161, 439-446 (2008).

88. Voorneveld, P. W. *et al*. Loss of SMAD4 alters BMP signaling to promote colorectal cancer cell metastasis via activation of Rho and ROCK. *Gastroenterology* 147, 196-208.e13 (2014).

89. Loschberger, A., Franke, C., Krohne, G., van de Linde, S. & Sauer, M. Correlative super-resolution fluorescence and electron microscopy of the

nuclear pore complex with molecular resolution. *J. Cell. Sci.* 127, 4351-4355 (2014).

90. Polishchuk, R. S. *et al*. Correlative light-electron microscopy reveals the tubular-saccular ultrastructure of carriers operating between Golgi apparatus and plasma membrane. *J. Cell Biol.* 148, 45-58 (2000).

91. Bock, D. D. *et al*. Network anatomy and in vivo physiology of visual cortical neurons. *Nature* 471, 177-182 (2011).

92. Mali, P., Esvelt, K. M. & Church, G. M. Cas9 as a versatile tool for engineering biology. *Nat. Methods* 10, 957-963 (2013).

93. Koning, R. I. *et al*. MAVIS: an integrated system for live microscopy and vitrification. *Ultramicroscopy* 143, 67-76 (2014).

94. Peckys, D. B., Dukes, M. J. & de Jonge, N. Correlative fluorescence and electron microscopy of quantum dot labeled proteins on whole cells in liquid. *Methods Mol. Biol.* 1117, 527-540 (2014).

95. Dukes, M. J., Peckys, D. B. & de Jonge, N. Correlative fluorescence microscopy and scanning transmission electron microscopy of quantum-dot-labeled proteins in whole cells in liquid. *ACS Nano* 4, 4110-4116 (2010).

96. Ritsma, L., Vrisekoop, N. & van Rheenen, J. In vivo imaging and histochemistry are combined in the cryosection labelling and intravital microscopy technique. *Nat. Commun.* 4, 2366 (2013).

97. Karreman, M. A. *et al*. Correlating intravital multi-photon microscopy to 3D electron microscopy of invading tumor cells using anatomical reference points. *PLoS One* 9, e114448 (2014).

98. Armer, H. E. *et al*. Imaging transient blood vessel fusion events in zebrafish by correlative volume electron microscopy. *PLoS One* 4, e7716 (2009).

99. van Ham, T. J. *et al*. Intravital correlated microscopy reveals differential macrophage and microglial dynamics during resolution of neuroinflammation. *Dis. Model. Mech.* 7, 857-869 (2014).

100. Hosseini, R. *et al*. Correlative light and electron microscopy imaging of autophagy in a zebrafish infection model. *Autophagy* 10, 1844-1857 (2014).

101. Maco, B. *et al*. Semiautomated correlative 3D electron microscopy of in vivo-imaged axons and dendrites. *Nat. Protoc.* 9, 1354-1366 (2014).

102. Hayworth, K. J. *et al*. Imaging ATUM ultrathin section libraries with WaferMapper: a multi-scale approach to EM reconstruction of neural circuits. *Front. Neural Circuits* 8, 68 (2014).

103. Marx, V. Neurobiology: Brain mapping in high resolution. *Nature* 503, 147-152 (2013).

104. Eberle, A. L. *et al*. High-resolution, high-throughput imaging with a multibeam scanning electron microscope. *J. Microsc.* (2015).

105. Cardona, A. *et al*. TrakEM2 software for neural circuit reconstruction. *PLoS One* 7, e38011 (2012).

106. Duke, E., Dent, K., Razi, M. & Collinson, L. M. Biological applications of cryo-soft X-ray tomography. *J. Microsc.* 255, 65-70 (2014).

107. Smith, E. A. *et al*. Correlative cryogenic tomography of cells using light and soft x-rays. *Ultramicroscopy* 143, 33-40 (2014).

108. Duke, E. M. *et al*. Imaging endosomes and autophagosomes in whole mammalian cells using correlative cryo-fluorescence and cryo-soft X-ray microscopy (cryo-CLXM). *Ultramicroscopy* 143, 77-87 (2014).

109. Glenn, D. R. *et al*. Correlative light and electron microscopy using cathodoluminescence from nanoparticles with distinguishable colours. *Sci. Rep.* 2, 865 (2012). 0. Narváez, A. C., Weppelman, I. G. C., Moerland, R. J., Hoogenboom J.P. & Kruit P. Confocal filtering in cathodoluminescence microscopy of nanostructures. *Applied physics letters* 104 (2014).

111. Giepmans, B. N. Bridging fluorescence microscopy and electron microscopy. *Histochem Cell Biol* 130, 211-7 (2008).

112. Lauf, U. *et al*. Dynamic trafficking and delivery of connexons to the plasma membrane and accretion to gap junctions in living cells. *Proc Natl Acad Sci U S A* 99, 10446-51 (2002).

Supplementary information

Supplementary table 1 | Overview of CLEM implementation – Selected studies on different biomaterials and in different research fields as a reference when implementing CLEM.

Field & use	CLEM approach or specifics	Ref
A. Human tissue		
Identifying axillary sweat gland structures	En bloc CLSM, serial section TEM	[1]
Skin (also connections and protrusion in colon cancer cells)	Integrated microscopy – FM-SEM	[2]
Reconstruction of kidney glomerular basement membrane	STORM-SEM	[3]
B. Non-human tissue		
Visualizing different cell types in mouse cerebellum	Pre-embedding QD-labeling	[4]
Golgi intermediates trafficking	GFP – HRP immunolabeling	[5]
Architecture and ultrastructure of neural circuits (mouse)	Array tomography (IF)	[6]
Wheat in intestine and peroxidases in liver (rat)	Integrated FM-TEM	[7]
Anatomy and physiology of visual cortex neurons	Intravital - large-scale 2D/ 3D CLEM	[8]
Mitochondria in *C. elegans* and synaptic adhesion (mouse)	MiniSOG	[9]
Visualization of pre-synaptic proteins in brain (rat)	GFP photo-oxidation	[10]
Calcium uptake and deposition in embryos (sea urchin)	iM – AirSEM	[11]
Macrophages vs. microglia in neuro-inflammation (zebrafish)	Intravital	[12]
Tumor cell invasion (mouse)	Intravital 3D CLEM	[13]
C.1 Eukaryotic cells – Primary cells		
RNA-containing nuclear structure in early apoptosis	iM – FM-TEM Tokuyasu labeling	[14]
α-synuclein localization in neurons	Tetracysteine/MiniSOG	[15]
Neuron differentiation, networking, phagocytosis	iM – ASEM fluorescent beads	[16]
C.2 Eukaryotic cells – Cell-lines		
Dynamics and trafficking of gap junctions	Pulse-chase TC-ReAsH/FlAsH	[17]
In mitotic cells four Golgi's are present	TC-ReAsH	[18]
Mitochondrial transformation during apoptosis	Live-cell, TC-FlAsH, TMRE; (3D) TEM	[19]
Identification of detergent resistant membrane rafts	Pre-embedding IF, TEM	[20]
Actin structure and clathrin mediated endocytosis	IF, metal-replica EM	[21]
Ca^{2+} sensor in ER; Cytoskeleton in growth cones and synapses	iM – ASEM, FNG immunolabeling	[22]
Diacylglycerol and nuclear envelope/ER reorganization in mitosis	Pre-embedding FM, TEM	[23]
Adhesion by synaptic neurexin and neuroligin	Pre-embedding FM, TEM	[24]
Mitochondrial structure and membrane relationship	PALM, followed by FIB-SEM	[25]
Connexin43 imaging	APEX-GFP fusion tag	[26]
mAtg9 in autophagy regulation	Combinatorial FPs + immunogold	[27]
Von Willebrand Factor remodeling during exocytosis	GFP, IF, TEM, tomography	[28]
CCCP as trigger for mitophagy	Live-cell CLSM, followed by TEM	[29]
GLUT4 expression, localization and quantification in adipocytes	Combinatorial GFP + immunogold	[30]
Autophagosome formation	Combinatorial GFP + immunogold	[31]
Diacylglycerol in nuclear envelope, reticulum and Golgi	iM – FM-SEM with GFP	[32]
Identification of endosomes and autophagosomes	cryo-FM and cryo-soft X-ray	[33]
Variation nuclear pore symmetrie	STORM – SEM	[34]
3D position of epsin on clathrin-coated structures	PALM – metal-replica EM	[35]
C.3 Eukaryotic cells – Unicellular organisms		
Plasma membrane reshaping during endocytosis in yeast	FPs; 3D EM, with fluorescence	[36]
Type VI secretion system of *Myxococcus xanthus*	Correlated 3D-PALM cryo-EM	[37]
Detailed Golgi architecture in *Saccharomyces cerevisiae*	3D CLEM by serial Tokuyasu	[38]
Polarized actin for sorting axonal and dendritic proteins	Membranes: phalloidin and SEM	[39]
D.1 Micro-organisms and viruses		
Chemosensory machinery and cell division in *e. coli*	GFP-ferritin	[40]
D.2 Micro-organisms and viruses – In cells		
Virus infection of mammalian cells	Fluorescent HIV, live-cell; FIB-SEM	[41]
Rubella virus-induced cell structures	Metallothionein tagging	[42]
Dynamics of HIV-containing compartments in macrophages	Live-cell FM; TEM	[43]
Infection of human skeletal muscle cells by Influenza A	Pre-embedding IF; TEM	[44]
Yersinia pseudotuberculosis during host infiltration	Pre-embedding fluorescence; TEM	[45]
D.3 Micro-organisms and viruses – In organisms		
Mycobacterium marinum containing granulomas in zebrafish	Pre-embedding FM; TEM	[46]
Requirement of importin-α7 for Influenza A replication (mice)	GFP-virus. CLSM, ESEM, TEM	[47]
E. Method books for CLEM		
Methods in Cell Biology volume 111, 2012	Various techniques	[48]
Methods in Cell Biology volume 124, 2014	Various techniques	[49]
Methods in Molecular Biology volume 1117, 2014	Various techniques	[50]

References

1. Wilke, K. *et al*. A strategy for correlative microscopy of large skin samples: towards a holistic view of axillary skin complexity. *Exp. Dermatol.* **17**, 73-81 (2008).

2. Liv, N. *et al*. Simultaneous Correlative Scanning Electron and High-NA Fluorescence Microscopy. *PLoS One* **8**, e55707 (2013).

3. Suleiman, H. *et al*. Nanoscale protein architecture of the kidney glomerular basement membrane. *Elife (Cambridge)* **2**, e01149 (2013).

4. Giepmans, B. N., Deerinck, T. J., Smarr, B. L., Jones, Y. Z. & Ellisman, M. H. Correlated light and electron microscopic imaging of multiple endogenous proteins using Quantum dots. *Nat Methods* **2**, 743-9 (2005).

5. Polishchuk, R. S. *et al*. Correlative light-electron microscopy reveals the tubular-saccular ultrastructure of carriers operating between Golgi apparatus and plasma membrane. *J. Cell Biol.* **148**, 45-58 (2000).

6. Micheva, K. D. & Smith, S. J. Array tomography: a new tool for imaging the molecular architecture and ultrastructure of neural circuits. *Neuron* **55**, 25-36 (2007).

7. Agronskaia, A. V. *et al*. Integrated fluorescence and transmission electron microscopy. *J. Struct. Biol.* **164**, 183-189 (2008).

8. Bock, D. D. *et al*. Network anatomy and in vivo physiology of visual cortical neurons. *Nature* **471**, 177-182 (2011).

9. Shu, X. *et al*. A genetically encoded tag for correlated light and electron microscopy of intact cells, tissues, and organisms. *PLoS Biol.* **9**, e1001041 (2011).

10. Horstmann, H., Vasileva, M. & Kuner, T. Photooxidation-guided ultrastructural identification and analysis of cells in neuronal tissue labeled with green fluorescent protein. *PLoS One* **8**, e64764 (2013).

11. Vidavsky, N. *et al*. Initial stages of calcium uptake and mineral deposition in sea urchin embryos. *Proc. Natl. Acad. Sci. U. S. A.* **111**, 39-44 (2014).

12. van Ham, T. J. *et al*. Intravital correlated microscopy reveals differential macrophage and microglial dynamics during resolution of neuroinflammation. *Dis. Model. Mech.* **7**, 857-869 (2014).

13. Karreman, M. A. *et al*. Correlating intravital multi-photon microscopy to 3D electron microscopy of invading tumor cells using anatomical reference points. *PLoS One* **9**, e114448 (2014).

14. Karreman, M. A. *et al*. Discovery of a new RNA-containing nuclear structure in UVC-induced apoptotic cells by integrated laser electron microscopy. *Biol. Cell.* **101**, 287-299 (2009).

15. Boassa, D. *et al*. Mapping the subcellular distribution of alpha-synuclein in neurons using genetically encoded probes for correlated light and electron microscopy: implications for Parkinson's disease pathogenesis. *J. Neurosci.* **33**, 2605-2615 (2013).

16. Hirano, K. *et al*. Electron microscopy of primary cell cultures in solution and correlative optical microscopy using ASEM. *Ultramicroscopy* **143**, 52-66 (2014).

17. Gaietta, G. *et al*. Multicolor and electron microscopic imaging of connexin trafficking. *Science* **296**, 503-507 (2002).

18. Gaietta, G. M. *et al*. Golgi twins in late mitosis revealed by genetically encoded tags for live cell imaging and correlated electron microscopy. *Proc Natl Acad Sci U S A* **103**, 17777-177782 (2006).

19. Sun, M. G. *et al*. Correlated three-dimensional light and electron microscopy reveals transformation of mitochondria during apoptosis. *Nat. Cell Biol.* **9**, 1057-1065 (2007).

20. Jahn, K. A. & Braet, F. Monitoring membrane rafts in colorectal cancer cells by means of correlative fluorescence electron microscopy (CFEM). *Micron* **39**, 1393-1397 (2008).

21. Collins, A., Warrington, A., Taylor, K. A. & Svitkina, T. Structural organization of the actin cytoskeleton at sites of clathrin-mediated endocytosis. *Curr. Biol.* **21**, 1167-1175 (2011).

22. Maruyama, Y., Ebihara, T., Nishiyama, H., Suga, M. & Sato, C. Immuno EM-OM correlative microscopy in solution by atmospheric scanning electron microscopy (ASEM). *J. Struct. Biol.* **180**, 259-270 (2012).

23. Domart, M. C. *et al*. Acute manipulation of diacylglycerol reveals roles in nuclear envelope assembly & endoplasmic reticulum morphology. *PLoS One* **7**, e51150 (2012).

24. Tanaka, H. *et al*. Higher-order architecture of cell adhesion mediated by polymorphic synaptic adhesion molecules neurexin and neuroligin. *Cell. Rep.* **2**, 101-110 (2012).

25. Kopek, B. G., Shtengel, G., Xu, C. S., Clayton, D. A. & Hess, H. F. Correlative 3D superresolution fluorescence and electron microscopy reveal the relationship of mitochondrial nucleoids to membranes. *Proc. Natl. Acad. Sci. U. S. A.* **109**, 6136-6141 (2012).

26. Martell, J. D. *et al*. Engineered ascorbate peroxidase as a genetically encoded reporter for electron microscopy. *Nat. Biotechnol.* **30**, 1143-1148 (2012).

27. Orsi, A. *et al*. Dynamic and transient interactions of Atg9 with autophagosomes, but not membrane integration, are required for autophagy. *Mol. Biol. Cell* **23**, 1860-1873 (2012).

28. Mourik, M. J. *et al*. von Willebrand factor remodeling during exocytosis from vascular endothelial cells. *J. Thromb. Haemost.* **11**, 2009-2019 (2013).

29. Padman, B. S., Bach, M., Lucarelli, G., Prescott, M. & Ramm, G. The protonophore CCCP interferes with lysosomal degradation of autophagic cargo in yeast and mammalian cells. *Autophagy* **9**, 1862-1875 (2013).

30. Hodgson, L., Tavare, J. & Verkade, P. Development of a quantitative Correlative Light Electron Microscopy technique to study GLUT4 trafficking. *Protoplasma* **251**, 403-416 (2014).

31. Uemura, T. *et al*. A cluster of thin tubular structures mediates transformation of the endoplasmic reticulum to autophagic isolation membrane. *Mol. Cell. Biol.* **34**, 1695-1706 (2014).

32. Peddie, C. J. *et al*. Correlative and integrated light and electron microscopy of in-resin GFP fluorescence, used to localise diacylglycerol in mammalian cells. *Ultramicroscopy* **143**, 3-14 (2014).

33. Duke, E. M. *et al*. Imaging endosomes and autophagosomes in whole mammalian cells using correlative cryo-fluorescence and cryo-soft X-ray microscopy (cryo-CLXM). *Ultramicroscopy* **143**, 77-87 (2014).

34. Loschberger, A., Franke, C., Krohne, G., van de Linde, S. & Sauer, M. Correlative super-resolution fluorescence and electron microscopy of the nuclear pore complex with molecular resolution. *J. Cell. Sci.* **127**, 4351-4355 (2014).

35. Sochacki, K. A., Shtengel, G., van Engelenburg, S. B., Hess, H. F. & Taraska, J. W. Correlative super-resolution fluorescence and metal-replica transmission electron microscopy. *Nat. Methods* **11**, 305-308 (2014).

36. Kukulski, W. *et al*. Precise, correlated fluorescence microscopy and electron tomography of lowicryl sections using fluorescent fiducial markers. *Methods Cell Biol.* **111**, 235-257 (2012).

37. Chang, Y. W. *et al*. Correlated cryogenic photoactivated localization microscopy and cryo-electron tomography. *Nat. Methods* **11**, 737-739 (2014).

38. Mari, M., Geerts, W. J. & Reggiori, F. Immuno- and correlative light microscopy-electron tomography methods for 3D protein localization in yeast. *Traffic* **10**, 1164-1178 (2014).

39. Watanabe, K. *et al*. Networks of polarized actin filaments in the axon initial segment provide a mechanism for sorting axonal and dendritic proteins. *Cell. Rep.* **2**, 1546-1553 (2012).

40. Wang, Q., Mercogliano, C. P. & Lowe, J. A ferritin-based label for cellular electron cryotomography. *Structure* **19**, 147-154 (2011).

41. Murphy, G. E. *et al*. Correlative 3D imaging of whole mammalian cells with light and electron microscopy. *J. Struct. Biol.* **176**, 268-278 (2011).

42. Risco, C. *et al*. Specific, sensitive, high-resolution detection of protein molecules in

eukaryotic cells using metal-tagging transmission electron microscopy. *Structure* **20**, 759-766 (2012).

43. Gaudin, R. *et al*. Dynamics of HIV-containing compartments in macrophages reveal sequestration of virions and transient surface connections. *PLoS One* **8**, e69450 (2013).

44. Desdouits, M. *et al*. Productive infection of human skeletal muscle cells by pandemic and seasonal influenza A(H1N1) viruses. *PLoS One* **8**, e79628 (2013).

45. Ligeon, L. A. *et al*. Role of VAMP3 and VAMP7 in the commitment of Yersinia pseudotuberculosis to LC3-associated pathways involving single- or double-membrane vacuoles. *Autophagy* **10**, 1588-1602 (2014).

46. Fenaroli, F. *et al*. Nanoparticles as Drug Delivery System against Tuberculosis in Zebrafish Embryos: Direct Visualization and Treatment. *ACS Nano* **8**, 7014-7026 (2014).

47. Resa-Infante, P. *et al*. Importin-alpha7 is required for enhanced influenza A virus replication in the alveolar epithelium and severe lung damage in mice. *J. Virol.* **88**, 8166-8179 (2014).

48. Müller-Reichert, T. & Verkade, P. Methods in Cell Biology. **111**, 445 (2012).

49. Müller-Reichert, T. & Verkade, P. Methods in Cell Biology. **124**, 442 (2014).

50. Kuo, J. Electron microscopy. **1117** (2014).

Chapter 3

Scanning EM of non-heavy metal stained biosamples: Large-field of view, high contrast and highly efficient immunolabeling

Pascal de Boer[#], Jeroen Kuipers[#], Ben N.G. Giepmans

Department of Cell Biology, University Medical Center Groningen, Groningen, the Netherlands

[#] Denotes equal contribution

Experimental Cell Research (2015) 337(2): 202-207

Abstract

Scanning electron microscopy (SEM) is increasing its application in life sciences for electron density measurements of ultrathin sections. These are traditionally analyzed with transmission electron microscopy (TEM); by most labs, SEM analysis still is associated with surface imaging only. Here we report several advantages of SEM for thin sections over TEM, both for structural inspection, as well as analyzing immuno-targeted labels such as quantum dots (QDs) and gold, where we find that QD-labeling is ten times more efficient than gold-labeling. Furthermore, we find that omitting post-staining with uranyl and lead leads to QDs readily detectable over the ultrastructure, but under these conditions ultrastructural contrast was even almost invisible in TEM examination. Importantly, imaging in SEM with STEM detection leads to both outstanding QDs and ultrastructural contrast. STEM imaging is superior over back-scattered electron imaging of these non-contrasted samples, whereas secondary electron detection cannot be used at all. We conclude that examination of ultrathin sections by SEM, which may be immunolabeled with QDs, will allow rapid and straightforward analysis of large fields with more efficient labeling than can be achieved with immunogold. The large fields of view routinely achieved with SEM, but not with TEM, allows straightforward raw data sharing using virtual microscopy, also known as nanotomy when this concerns EM data in the life sciences.

1. Introduction

Conventional transmission electron microscopy (TEM), i.e. operation around 100 kV, has been the standard to analyze cross sections of biological samples for decades. The high energy of the electrons used in TEM enabled high resolution imaging. A drawback of TEM is the need for contrasting the sample with heavy metals, typically uranyl and lead, since the biological sample itself hardly scatters the high energy electrons resulting in low contrast. Scanning electron microscope (SEM) with a transmitted electron detector has been used for imaging ultrathin sections of tissues as an alternative for TEM. With the availability of field emission SEMs with high beam currents the image quality nowadays competes with that of TEM [1, 2]. The use of low energy scanning transmission EM (STEM) has also been shown to be useful in imaging of unstained biological samples [3]. The back scattered detector (BSD) in SEM is increasingly used for its ability to image ultrastructure of in plastic embedded tissue, so-called blockface, prior to sectioning, or for imaging of collected sections on a solid support [4]. This recently has been explored to generate 3D techniques like focused ion beam milling [5] or imaging of a large amount of serial sections [6, 7]. But the 3D techniques rely on the introduction of as much as possible heavy metals to prevent the samples from charging as well as for high yields of back-scattered electrons. Often multiple layers of osmium plus *en-bloc* staining with uranyl, lead and copper salts are used [8], giving almost binary images with outstanding membrane contrast. This is for example necessary for tracing neurons in consecutive images of 20 µm thick volumes [9]. The contrasting agents mask the intrinsic electron scattering differences of the biological sample itself. These properties can be useful to discriminate the different structures, for example the distinct secretory granules in pancreas. Another advantage of using unstained samples is that low contrast EM probes are more easily visible. Quantum dots (QDs) are not generally used in EM, probably because they are less electron dense than gold particles [10, 11]. However, they are advantageous over gold since the shelf-life is longer, penetrates better [11], can be used for correlated microscopy (reviewed in [12]) and label up to 10-fold more efficient than immunogold (below). We compared standard contrasting method with non-contrasted samples and immunolabeling followed by TEM and SEM acquisition with different detectors. STEM imaging of these non-contrasted QD labeled sections is superior over TEM imaging and is therefore a great

alternative, even more so when imaging large areas, or when other electron detectors or even optical detectors are used.

2. Materials and methods

2.1. Tissue and sample preparation

Rat pancreas was used as described before [13]. Briefly, fresh pancreas was cut into small pieces and fixed in 4% para-formaldehyde and 0.1% glutaraldehyde in 0.1 M sodiumcacodylate buffer, pH 7.4. 40 µm Vibratome sections were cut and selected for presence of islets of Langerhans. Those were postfixed with 1% osmiumtetroxide/1.5% potassiumferrocyanide in 0.1 M sodiumcacodylate, dehydrated through ethanol and embedded in EPON (Serva). Ultrathin sections (80 nm) were cut and collected on form-var coated nickel grids (electron microscopy sciences, Hatfield, Pennsylvania).

2.2. Post-embedding immunolabeling

Grids were incubated (room temperature) with tissue facing down on droplets on parafilm. First, samples were etched with 1% periodic acid (Merck, New Jersey) in milliQ water for 10 minutes to increase antigenicity. This was followed by 30 min blocking with 1% bovine serum albumin (BSA; Sanquin, The Netherlands) in tris-buffered saline (TBS), pH 7.4. Next, anti-insulin (guinea pig; 1:1000 in 1% BSA/TBS, Life Technologies) was incubated for 2 h, followed by four washes of 5 min with TBS and subsequent incubation for 1 h with biotinylated secondary antibody (donkey-anti-guinea pig; 1:400 in 1% BSA/TBS, Jackson Immunoresearch, UK) followed by four washes in TBS. Finally, streptavidin conjugated QD655 (1 µM; 1:1000 unless noted otherwise, in 1% BSA/TBS, Life Technologies) or 10 nm gold (various concentrations, BBI solutions, United Kingdom) were added for 1 h followed by four washes in TBS and two in 0.1 M sodiumcacodylate. Subsequently, samples were either post-stained with 2% uranyl-acetate in methanol and Reynold's lead-citrate or left untreated. Labeling efficiency was quantified by counting the number of particles (gold or QDs) per fifty insulin granules of a similar size with the counting tool in Photoshop (Adobe).

2.3. Transmission EM

Imaging of the samples was in a FEI CM100bio TEM at 80 KV equipped with a digital camera (Morada, OlympusSIS). The resolution of the camera was set on 3072×2304 pixels to match the resolution of the SEM.

2.4. Scanning (transmission) EM

If feasible, the same area recorded in the TEM was imaged in a Zeiss Supra55 SEM equipped with a 100 nano-Ampere anode. Because the magnification in SEM differs from the TEM, the SEM magnification is determined by the scanned area related to output on polaroid format, we adjusted magnification and rotation to match the field of view. STEM detection with a four quadrant STEM detector used in inverted darkfield mode, was done at 29 kV with 30 µm aperture at 3.5 mm working distance. BSD detection was done at 5 kV with 60 µm aperture at 6.5 mm working distance using high current mode. Secondary electron detection using the Everhart–Thornley detector or an inLens detector was done at 5 kV, 30 µm aperture at 3.5 mm working distance. All images were recorded at the same scan speed (cycle time 1.5 minute at 3072×2304 pixels). Contrast and brightness were set based on a live histogram. High resolution large-scale STEM images of approximately 40×50 µm at 2.5 nm pixel size were generated with the external scan generator ATLAS (Fibics, Canada), individual tiles were stitched in VE viewer (Fibics, Canada) and exported as a single tif file or an html file. All data is available through virtual microscopy or www.nanotomy.org.

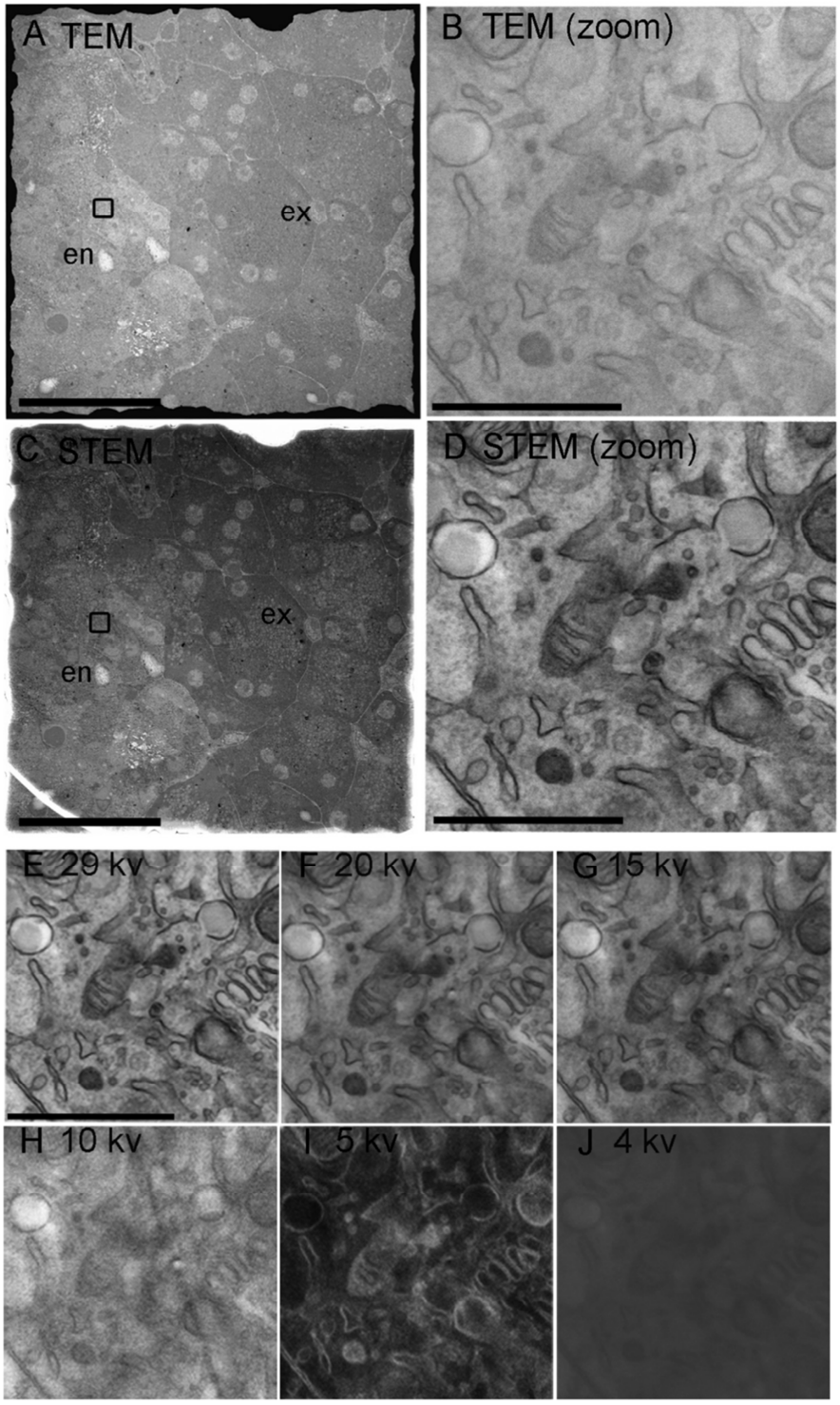

Figure 1 | STEM imaging provides better tissue contrast in the absence of post-staining compared to TEM. (A–D) TEM versus STEM imaging of an unstained rat pancreas 80 nm section containing both endocrine (en) and exocrine (ex) tissue. Compared to TEM (A and B), the STEM images (C and D) show more details and show better contrast. Bars in A and C 50 µm, B and D 1 µm. (E–J) Effect of different acceleration voltages on STEM image quality. 15 KV (G) gives still a good image, comparable to 29 KV (E). Going to 10 KV (H) gives a strong reduction of both contrast and resolution. Going down to 5 KV (I) results in a revival of image resolution and contrast, but also an unexpected inversion of the contrast which is lost at 4 kV (J). Bars: 1 µm

3. Results

Image acquisition was first with TEM followed by SEM. In samples without heavy metal post-staining, it was practically impossible to localize the islet of Langerhans on the phosphorescence screen of the TEM, because of lack of contrast. Furthermore, this lack of contrast impeded sharp focusing. Only after taking a digital image and setting white point and block points in the live image histogram, resulting in a grey level distribution covering only 10% of the dynamic range, endocrine cells could be

recognized from exocrine tissue (Fig. 1A). The same area was recorded in the SEM with STEM detection. Tracing back the area during live scanning was easy because the contrast could be controlled to yield an image covering the full dynamic range of 8 bits 256 grey values (Fig. 1C and D). Since the better contrast in STEM can be explained to some extend by the lower energy of the electrons, lower acceleration voltages were applied (Fig. 1E–J). Going down to 15 kV the tissue contrast was comparable or maybe even a bit less than at 29 kV. The image was more noisy and fine details in the cytoplasm disappeared. Still the image quality was good enough to recognize details as mitochondrial cristae, endocytic vesicles and stacks of the Golgi apparatus. Applying 10 kV acceleration voltage lead to a sharp drop in image quality. Low contrast and high noise preclude recognition of the aforementioned subcellular details. Remarkably, at 5 kV image quality improved, but grey levels were inverted. Going down to 4 kV still yielded low contrast, which needed the maximal STEM detector gain. Using even lower acceleration voltages, no electrons passed through the section making it impossible to obtain a STEM image. In conclusion, standard analysis of non-contrasted ultrathin sections is best performed with STEM at relative high (29 kV in our case) acceleration voltage.

Since heavy metal contrasting is not necessary for STEM [3], nanoparticles with less electron density than gold, such as QDs [10], will have sufficient contrast compared to surrounding tissue. Indeed, QD655 is hardly visible in heavily contrasted samples on the insulin granules, both in TEM and STEM and can only be detected at high magnification (Fig. 2A–D). Omitting the traditional post-staining with uranyl/lead (U/Pb) leads to outstanding QD655 contrast (Fig. 2E and F), but ultrastructural contrast was low in TEM, in agreement with our previous results (Fig. 1). On the other hand, STEM imaging showed high QD655 contrast in combination with good ultrastructural context, even at low magnifications (Fig. 2G and H). Since BSD is more often used and more often available than STEM detection, we also compared BSD signal on the non-contrasted QD655 labeled sample, as well as secondary electron detection by both the InLens detector, and the Everhart–Thornley detector (Fig. S1). BSD detection using the U/Pb contrasted sample showed even less outstanding QD contrast compared to STEM, whereas on non-contrasted sample this was similar. However the images were more noisy and showed less details as can be seen for example by the mitochondrial cristae being not resolved where they are in the STEM image (Fig. S1F). Secondary electron detection with the in lens detector gave similar pattern but with much less tissue contrast. The conventional SE2 detection with a Everhart–Thornley detector showed even less contrast and when omitting U/Pb no image was obtained (Fig. S1G and H). We conclude STEM detection is the best choice for imaging non-contrasted samples. Thus, in general tissue contrast was better with U/Pb post-staining, but masks the QDs and omitting U/Pb staining lead to improved QD contrast. Immunogold labeling is better identifiable than QDs, probably because of higher electron density. However QDs are advantageous as they are more stable during storage, are also well observable when U/Pb contrasting is omitted (see above) but also penetrate better [10]. Therefore, we compared labeling efficiency of QDs (QD655, Fig. 3A) and 10 nm gold (Fig. 3B). A striking ~10 times higher labeling efficiency was observed with QD655 compared to 10 nm gold (Fig. 3C). Using different concentrations of QD or gold reagents similar labeling densities were quantified, so excluding a concentration effect.

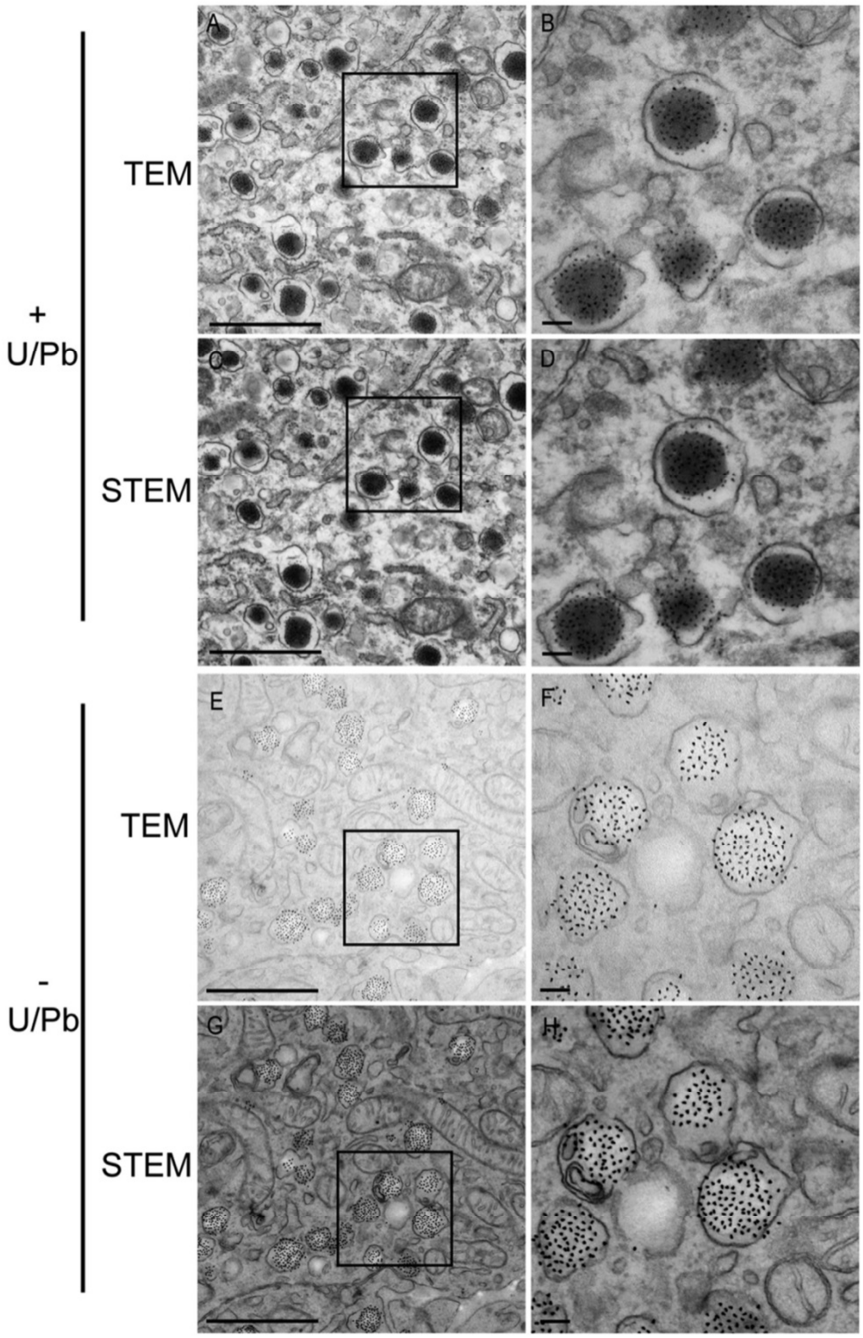

Figure 2 | Detection of QD655 with STEM is superior over TEM in the absence of U/Pb contrasting. (A–D) With uranyl and lead post-staining QDs are barely visible on insulin granules of rat pancreas, without differences between TEM and STEM. (E–H) Omitting U/Pb gives outstanding QD655 contrast, but with TEM the contrast of the tissue is very low (E and F). In STEM both the QD655 and the tissue show good contrast (G and H). Bars 1 µm (left panels) or 0.1 µm (right panels).

4. Discussion

Scanning EM imaging of biological samples is getting more popular for imaging electron density instead of surface information. Beneficially, SEM allows relative straightforward 3D analysis by serial section array tomography, focused ion beam milling or even serial blockface imaging with a microtome inside the SEM (for recent reviews see [14, 15]). These techniques in general use BSD, which requires extensive heavy metal staining with multiple layers of osmium and *en-bloc* uranyl and lead staining, all for enhancing conductivity and contrast [8]. Using the transmission detector, STEM, for ultrathin sections single-frame images of more than sixty times the size of TEM can be acquired in

the SEM [1]. Adding automated STEM mosaic acquisition and stitching allows imaging of extreme large areas at high resolution [1, 2, 16]. We find that STEM acquisition of these non-contrasted samples gives higher contrast than TEM imaging, with the added benefit that intrinsic differences in electron density within biological samples can be better observed (Fig. 3C). Omitting heavy metal post-staining of biological samples in routine TEM is rarely done [3], majorly because of the lack of contrast (Fig. 2A and B; mind that on the phosphorescence screen samples were almost undetectable). However, uranyl/lead post-staining of samples obscure signals of nanoparticles such as QDs. Without U/Pb, the contrast seen with both TEM and S(T)EM mostly comes from membranes due to osmium fixation, with these membranes much more pronounced in S(T)EM (Fig. 1). It should be noted that contrast formation in STEM, based on forward scattering, is widely different from that in TEM which uses phase contrast. Nevertheless, we observe that under the typical imaging conditions used here STEM holds a benefit for unstained sections over TEM. For STEM, the number of scattering events within the 80 nm section determines the contrast. Above 15 kV, this apparently stays constant (Fig. 1B), which is not unreasonable given that the total electron interaction volume at these energies would be a micrometer or larger. Surprisingly, a STEM image with an acceleration voltage as low as 5 kV could be obtained using an unstained 80 nm section showing more details and less noise than at 10 kV. Here, the image contrast was inverted with membranes being white instead of black. This might because below 5 kV the entire interaction volume falls within the section and no electrons penetrate. 5 kV Maybe the point where osmium-rich parts block all electrons, but through carbon forward-scattered electrons can still escape, leading to a black–white contrast. At 10 kV almost all electrons might undergo multiple scattering events and the signal becomes blurred. We note that, in contrast to STEM, BSD typically uses lower energy (<5 kV) electrons. With a circular BSD detector, contrast and resolution is less in BSD than STEM detection (Fig. S1E and F), but note that this may be different on microscopes with more elaborate BSD detector configurations or when imaging under immersion or stage-bias.

The label stands out in unstained samples, because differences in electron scattering between the label and surrounding tissue is higher. Indeed QDs, which are less electron dense than immunogold, only are easily detectable in the absence of U/Pb, with a superior contextual contrast with STEM over TEM (Fig. 2). Moreover, the QD-labeling beats conventional immunogold-labeling by a factor of 10 in these conditions (Fig. 3), which also accounts for other epitopes (data not shown). Quantification of EM data is often a hurdle as single snapshots by TEM at a high resolution are limited to a small field of view [17]. Automated large-scale 2D imaging with STEM has shown its value before for quantification [18]. Additional to efficient quantification, large-scale EM is less biased [19] and enables the observation of rare or interesting events unrelated to the research question as it does not depend on the selection of small regions of interest. These benefits are best harvested when sharing data open access via virtual microscopy or nanotomy. Interpretation of our data is open to all other, non-selected areas (www.nanotomy.org).

In conclusion, imaging of non-contrasted samples to observe intrinsic contrast differences or label identification, can best be performed in STEM. In addition, the efficient QDs labeling opens new avenues for successful postembedding labeling where gold labeling failed. STEM imaging also has the big advantage that large areas can be scanned as can be seen in the online datasets, typically resulting in data of approximately 40×50 μm^2 with a 2.5 nm pixel resolution, whereas digital TEM provides a field of view of just a few µm square at this resolution. Large area recordings facilitate data recognition of rare events and/or labeling more easy, quantification, and diminishes bias during selection of region of interest.

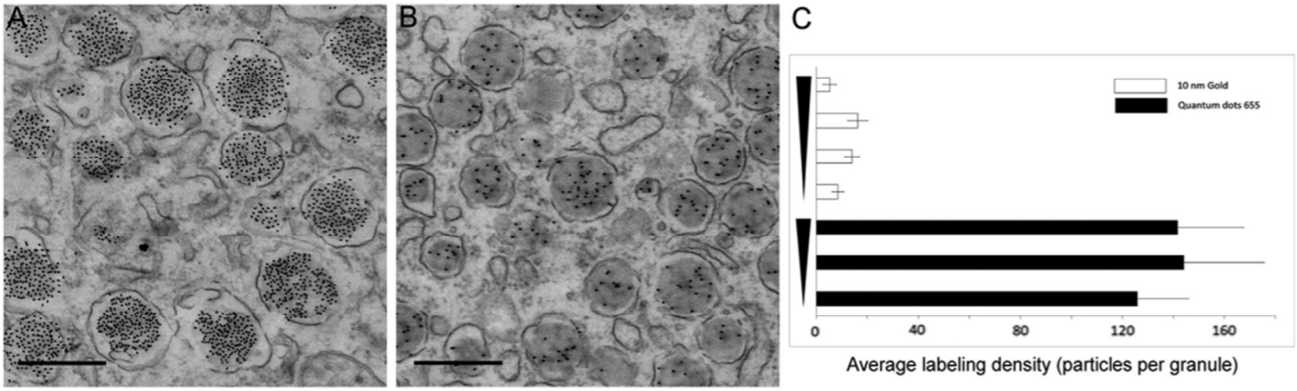

Figure 3 | QD655 labeling is more efficient than 10 nm immunogold. Post-embedding immunolabeling for insulin with QD655 (A) or 10 nm gold (B) detection on rat pancreas. QD655 gives ten times more label density of insulin granules of similar sizes compared to 10 nm gold without the influence of label concentration (C). Different concentrations tested, from top to bottom are streptavidin QD655 1:500 (1), 1:1000 (2) and 1:2000 (3), and streptavidin 10 nm gold 1:50 (1), 1:100 (2), 1:200 (3) and 1:500 (4). Large-scale datasets per label concentration are provided online. Scale bars are 200 nm

Acknowledgments

We thank our departmental members and Jacob P. Hoogenboom (Delft University of Technology, The Netherlands) for feedback and acknowledge financial support from the Netherlands Organization for Scientific Research (ZonMW91111006; “Microscopy Valley” STW12718; NWO175-010-2009-023).

References

[1] M. Kuwajima, J.M. Mendenhall, L.F. Lindsey, K.M. Harris, Automated transmission-mode scanning electron microscopy (tSEM) for large volume analysis at nanoscale resolution, PLoS One. 8 (2013) e59573.

[2] M. Kuwajima, J.M. Mendenhall, K.M. Harris, Large-volume reconstruction of brain tissue from high-resolution serial section images acquired by SEM-based scanning transmission electron microscopy, Methods Mol. Biol. 950 (2013) 253-273.

[3] A. Takaoka, T. Hasegawa, Observations of unstained biological specimens using a low-energy, high-resolution STEM, J. Electron. Microsc. (Tokyo). 55 (2006) 157-163.

[4] K.L. Briggman, D.D. Bock, Volume electron microscopy for neuronal circuit reconstruction, Curr. Opin. Neurobiol. 22 (2012) 154-161.

[5] G. Knott, H. Marchman, D. Wall, B. Lich, Serial section scanning electron microscopy of adult brain tissue using focused ion beam milling, J. Neurosci. 28 (2008) 2959-2964.

[6] H. Horstmann, C. Korber, K. Satzler, D. Aydin, T. Kuner, Serial section scanning electron microscopy (S3EM) on silicon wafers for ultra-structural volume imaging of cells and tissues, PLoS One. 7 (2012) e35172.

[7] M. Reichelt, L. Joubert, J. Perrino, A.L. Koh, I. Phanwar, A.M. Arvin, 3D reconstruction of VZV infected cell nuclei and PML nuclear cages by serial section array scanning electron microscopy and electron tomography, PLoS Pathog. 8 (2012) e1002740.

[8] J.C. Tapia, N. Kasthuri, K.J. Hayworth, R. Schalek, J.W. Lichtman, S.J. Smith, J. Buchanan, High-contrast en bloc staining of neuronal tissue for field emission scanning electron microscopy, Nat. Protoc. 7 (2012) 193-206.

[9] K.J. Hayworth, C.S. Xu, Z. Lu, G.W. Knott, R.D. Fetter, J.C. Tapia, J.W. Lichtman, H.F. Hess, Ultrastructurally smooth thick partitioning and volume stitching for large-scale connectomics, Nat. Methods. 12 (2015) 319-322.

[10] B.N. Giepmans, T.J. Deerinck, B.L. Smarr, Y.Z. Jones, M.H. Ellisman, Correlated light and electron microscopic

imaging of multiple endogenous proteins using quantum dots, Nat Methods. 2 (2005) 743-9.

[11] R. Nisman, G. Dellaire, Y. Ren, R. Li, D.P. Bazett-Jones, Application of quantum dots as probes for correlative fluorescence, conventional, and energy-filtered transmission electron microscopy, J. Histochem. Cytochem. 52 (2004) 13-18.

[12] P. de Boer, J.P. Hoogenboom, B.N. Giepmans, Correlated light and electron microscopy: Ultrastructure lights up! Nat. Methods. 12 (2015) 503-513.

[13] R.B. Ravelli, R.D. Kalicharan, M.C. Avramut, K.A. Sjollema, J.W. Pronk, F. Dijk, A.J. Koster, J.T. Visser, F.G. Faas, B.N. Giepmans, Destruction of tissue, cells and organelles in type 1 diabetic rats presented at macromolecular resolution, Sci. Rep. 3 (2013) 1804.

[14] L. Hughes, C. Hawes, S. Monteith, S. Vaughan, Serial block face scanning electron microscopy--the future of cell ultrastructure imaging, Protoplasma. 251 (2014) 395-401.

[15] C.J. Peddie, L.M. Collinson, Exploring the third dimension: Volume electron microscopy comes of age, Micron. 61 (2014) 9-19.

[16] E. Sokol, D. Kramer, G.F. Diercks, J. Kuipers, M.F. Jonkman, H.H. Pas, B.N. Giepmans, Large-scale electron microscopy maps of patient skin and mucosa provide insight into pathogenesis of blistering diseases, J. Invest. Dermatol. 135 (2015) 1763-1770.

[17] T.M. Mayhew, Quantitative immunocytochemistry at the ultrastructural level: A stereology-based approach to molecular nanomorphomics, Cell Tissue Res. 360 (2015) 43-59.

[18] J. Kuipers, T.J. van Ham, R.D. Kalicharan, A. Veenstra-Algra, K.A. Sjollema, F. Dijk, U. Schnell, B.N.G. Giepmans, FLIPPER, a combinatorial probe for quantitative correlated live imaging and electron microscopy, Cell & Tissue Research. 360 (2015) 61-70.

[19] F.G. Faas, M.C. Avramut, B. M van den Berg, A.M. Mommaas, A.J. Koster, R.B. Ravelli, Virtual nanoscopy: Generation of ultra-large high resolution electron microscopy maps, J. Cell Biol. 198 (2012) 457-469.

Supplementary information

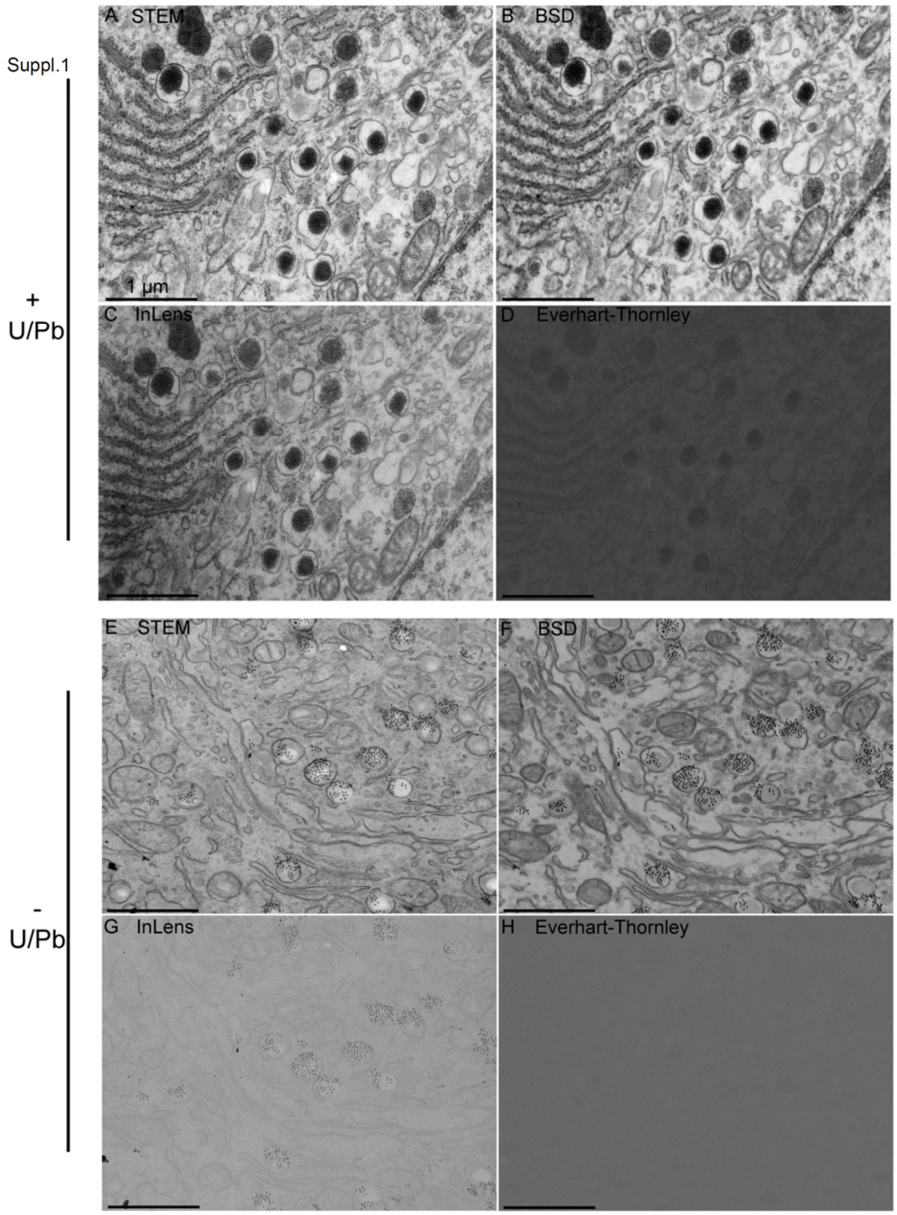

Supplementary figure 1 | STEM detection is superior for imaging of non-contrasted samples compared to other available SEM detectors. Different SEM detectors imaging of U/Pb contrasted (A–D) and non-contrasted (E–H) samples. U/Pb provides good tissue contrast when STEM (A), BSD (B) and InLens (C) detection is used, but with a slightly lower resolution compared to STEM (eg. mitochondrial cristae). However, QDs are again masked with BSD and InLens detection in the presence of U/Pb (B and C) similar to STEM detection (A). SE2 detection with the Everhart-Thornley detector gives very poor contrast (D). In non-contrasted samples, QDs also stand out when imaged with BSD (F) and InLens detection of secondary electrons (G). However, tissue contrast and resolution with BSD (F) is less compared with STEM (E) and no tissue is observed with InLens (G). Note that mitochondrial cristae are not observed with BSD at this magnification (F). SE2 detection with the Everhart-Thornley detector gives no tissue or QD contrast at all (H). The InLens and SE2 images (C and D, G and H) are displayed here with inverted contrast. Scale bars are 1 µm.

Chapter 4

Electron beam induced colorEM

Chapter 4a

Nanodiamonds as multi-purpose labels for microscopy

P. de Boer[2#], S.R. Hemelaar[1#], M. Chipaux[1], W. Zuidema[3], T. Hamoh[1], F. Perona Martinez[1], A. Nagl[1], J.P. Hoogenboom[3], B.N.G. Giepmans[2] and R. Schirhagl[1]

[1]Department of Biomedical Engineering, University Medical Center Groningen, Groningen the Netherlands; [2]Department of Cell Biology, University Medical Center Groningen, Groningen, the Netherlands; [3]Department of Imaging Physics, Delft University of Technology, Delft, the Netherlands

[#] Denotes equal contribution

Scientific Reports (2017) 7(1): 720-729

Abstract

Nanodiamonds containing fluorescent nitrogen-vacancy centers are increasingly attracting interest for use as a probe in biological microscopy. This interest stems from (i) strong resistance to photobleaching allowing prolonged fluorescence observation times; (ii) the possibility to excite fluorescence using a focused electron beam (cathodoluminescence; CL) for high-resolution localization; and (iii) the potential use for nanoscale sensing. For all these schemes, the development of versatile molecular labeling using relatively small diamonds is essential. Here, we show the direct targeting of a biological molecule with nanodiamonds as small as 70 nm using a streptavidin conjugation and standard antibody labelling approach. We also show internalization of 40 nm sized nanodiamonds. The fluorescence from the nanodiamonds survives osmium-fixation and plastic embedding making them suited for correlative light and electron microscopy. We show that CL can be observed from epon-embedded nanodiamonds, while surface-exposed nanoparticles also stand out in secondary electron (SE) signal due to the exceptionally high diamond SE yield. Finally, we demonstrate the magnetic read-out using fluorescence from diamonds prior to embedding. Thus, our results firmly establish nanodiamonds containing nitrogen-vacancy centers as unique, versatile probes for combining and correlating different types of microscopy, from fluorescence imaging and magnetometry to ultrastructural investigation using electron microscopy.

Introduction

In correlative microscopy, a comprehensive view on a specimen is acquired by combining information obtained with different modalities of microscopy. Arguably, correlative light and electron microscopy (CLEM)[1] constitutes the most widespread form of correlative microscopy. In CLEM, fluorescence microscopy (FM) prior to EM acquisition is used, e.g., to visualize fluorescently labeled molecules within the nano-structural environment imaged with EM. Alternatively one can pinpoint a region of interest for high-resolution EM investigation using live-cell or *in vivo* FM. However, the intrinsic resolution gap between FM and EM limits the degree to which molecules can be localized within the structural EM images. Preferably, this localization would be at the level of EM resolution. A major challenge in CLEM is thus to find approaches and labels that allow live-cell or *in vivo* observation, maintain their fluorescence during EM sample preparation, and can be localized with near-EM resolution.

Direct electron-beam fluorescence excitation, or cathodoluminescence (CL), provides a solution that allows EM localization, but standard organic or biological fluorophores are instable under electron beam exposure[2]. In addition, most fluorescent labels do not survive the sample preparation needed for EM. Colloidal quantum dots are fluorescent, can be used in live cell experiments, and they can be precisely located in EM thanks to their electron dense core[3, 4]. However, CL from bio-conjugated quantum dots, which would allow distinguishing multiple quantum dot labels in color, has not yet been shown. This is probably due to bleaching of quantum dot fluorescence under electron exposure. With phosphor nanoparticles, CL from particles with <50 nm diameter has been observed[5-7], but application in an EM-prepared sample has to our knowledge not yet been demonstrated. Larger phosphor particles doped with rare-earth atoms have also been explored for upconversion luminescence[8], which may be attractive in combination with *in vivo* imaging. CL from such particles after cellular uptake and sectioning for EM has been shown[9, 10]. However, so far only particles of >100 nm have been reported, which precludes their use as a molecular label, and conjugation schemes for these particles have not yet been reported.

In recent years diamond nanoparticles containing defect centers have attracted increasing interest[11] for use as a molecular label because of their excellent photostability. These fluorescent nanodiamonds (FNDs) are also bio-compatible[12, 13] and can be internalized in cells[14-18]. Further interest in the FNDs stems from the fact that they can be used as local sensors of magnetic[19] or electric fields[20], temperature[21], or strain[22], which could enable multi-parameter correlative microscopy. Moreover, stable CL from FNDs containing nitrogen-vacancy (NV) centers[5], as well as silicon-vacancy centers[23] has been demonstrated, for the NV-FNDs even after cellular uptake and embedding and sectioning for scanning transmission EM[24] or in live-cell EM studies[25]. However, in these studies the FNDs are large (100–150 nm), limiting the use to cell uptake studies only.

Here, we take the step towards FNDs that are 40 nm and 70 nm in size on average. We show that fluorescence, optically detected magnetic resonance (ODMR), and CL can be recorded from these particles after internalization. Moreover, we present antibody-targeted labelling using the 70 nm FNDs, and demonstrate that these FNDs, targeted to a specific protein can be detected in tissue sections fixed and stained for EM using a standard protocol that allows ultrastructural preservation. Combined with live-cell fluorescence and optical recording of magnetic resonance spectra, our results demonstrate the unique potential of FNDs as biomolecular targets for multi-parameter correlative microscopy.

Material and methods

Nanodiamonds

Fluorescent nanodiamonds of 40 nm (FND40) and 70 nm (FND70) contain 10–15 and >300 NV centers, respectively as stated by the supplier (Adamas Nanotechnologies, NC, USA). FNDs were drop-casted on ITO-coated cover glasses (Optics Balzers, Liechtenstein) and subsequently air-dried. FNDs were analyzed with EM using secondary electron (SE) detection for size and dispersity on a FEI Verios scanning EM. The optimal excitation wavelength was assessed using a scanning confocal system (Zeiss LSM 780, Plan-Apochromat 63x/1.40 lens). Using lambda mode, emission spectra were recorded creating intensity profiles between 571 and 687 nm with 9 nm intervals upon excitation with 405, 440, 488, 514, 561 and 594 nm lasers with appropriate beam splitters. Intensities were measured by comparing grey values of the individual images at the 9 nm intervals using Matlab and plotted in arbitrary units. For the size measurements, images were analyzed using ImageJ. In total 5051 particles were analyzed for FND70, and 1141 for FND40. As the particles were markedly non-spherical[26], we defined the size as the square root of the surface area of FNDs as detected with secondary electrons. We note that this is an over-estimation as the shortest particle axis will mostly be perpendicular to the surface because of the drop-casting and drying. For the analysis of particle size versus CL intensity, the secondary electron images were used as a mask for the CL signal and the CL intensity of the FND was taken to be the mean signal in the mask areas. To find FNDs with zero CL intensity, the background signal plus one standard deviation was subtracted from the mean CL intensity of each ND, which was normalized afterwards.

FND40 uptake by J774 macrophages

J774A.1 macrophages (LGC Standards, Germany) which play an important role in the immune system, were cultured in Dulbecco's Modified Eagle Medium (DMEM) with high glucose, supplemented with 10% FBS, 1% Penicillin/streptomycin and 1% Glutamax (Gibco, ThermoFisher Scientific, The Netherlands). Cells were incubated with 1 ug/ml FND40 in cell culture medium for 5 hours at 37 °C and 5% CO_2. After removal of culture medium with FNDs, cells were fixed with 4%

paraformaldehyde/0.1% glutaraldehyde in 0.1 M cacodylate buffer, pH 7.4 (CaCO) for 30 minutes at room temperature (RT). Nuclei were counterstained with 4',6-diamidino-2-phenylindole (DAPI). Before optically detected magnetic resonance (ODMR) measurements we used phalloidin-FITC (Sigma-Aldrich, The Netherlands) to label f-actin to visualize the cells. Samples were analyzed using a Zeiss LSM780 confocal microscope using 405 nm and 561 nm excitation. The amount of particles taken up by the cells was estimated using a home written script for the image analysis software FIJI (Fiji Is Just ImageJ, see supplementary information for a detailed explanation). Next the same samples were prepared for EM (see below).

FND immunolabeling of HT29-EpCAM-GFP cells

HT29 is a human epithelial colon carcinoma cell line, and HT29-EpCAM-GFP stable cells were engineered that overexpress the epithelial cell adhesion molecule (EpCAM) fused to GFP[27]. These were also cultured in DMEM complete medium. Cells were seeded in gamma irradiated 35 mm glass bottom collagen coated dishes (MatTek corporation, MA, USA) until clusters of at least 10 cells grew. Cells were fixed in 4% paraformaldehyde/0.1% glutaraldehyde in 0.1 M cacodylate (15 min, RT) and subsequently blocked in PBS with 5% BSA (PBSA). Then cells were incubated (1 hr RT) with an antibody against the extracellular domain of EpCAM, namely MOC31[27, 28]. After washing in 1% PBSA, samples were incubated with rabbit-anti-mouse-biotin (Dako Netherlands) in 1% PBSA. Cells were washed in 0.1 M cacodylate and incubated with a premixed solution of FNDs and Streptavidin (Sigma-Aldrich, Zwijndrecht, the Netherlands) on a 1:20 weight ratio in 0.1 M cacodylate. As a positive control, cells were incubated with streptavidin-conjugated quantum dots (QD655, Life Technologies, The Netherlands). After washing, cells were imaged using a Zeiss LSM780 confocal microscope using a 488 nm and 561 nm laser. For every sample at least 3 different cell clusters were imaged at 3 different times. Confocal images were analyzed and processed (brightness and contrast) using Fiji[29]. EpCAM and FND signal overlap was calculated by manually removing GFP signal coming from membranes inside the cluster using FIJI software. Next the signals were subjected to a threshold and converted into binary values. Next the percentage of FND positive EpCAM pixels was calculated and related to the total of EpCAM positive pixels.

Sample preparation for integrated light and electron microscopy

We proceeded with the J774 and HT29 EpCAM-GFP cells described above. After washing with 0.1 M cacodylate buffer, cells were incubated with 1% osmiumtetroxide/1.5% potassiumferrocyanide in 0.1 M cacodylate buffer (30 min on ice), followed by washing with water. Next, the cells were dehydrated through an increasing graded ethanol series and left overnight in 1:1 ethanol and Epon (Serva) mixture at room temperature, which was replaced by pure Epon (4 times) and finally polymerized overnight at 58 °C. The cover glass of the imaging dish was removed using hydrogen fluoride. Areas containing cells were selected using a stereo microscope and sawn from the Epon block. Subsequently, 300 nm sections were cut with an ultramicrotome (Leica EM UC7) using a glass knife and put on an ITO coated cover glass. Subsequently, sections were counterstained with Hoechst.

Integrated light and electron microscopy

Fluorescence preservation was checked using the Zeiss LSM780. Next, the same sections were imaged under high vacuum using a SECOM integrated microscope (Delmic, The Netherlands) in a Zeiss Supra55 scanning EM. The SECOM is equipped with a four color LED, a dichroic mirror (Di01-R405/488/561/635, Semrock, NY, USA), a filter wheel and a CCD camera. Fluorescence of both Hoechst and FNDs was recorded using a 20x/0.75 vacuum compatible objective. EM of the same ROI was acquired using a back scattered electron detector at 10 kV with 60 µm aperture at 9.7 mm

working distance. Overlays were created using the SECOM software (Odemis). CL was recorded using a SECOM platform, only equipped with a vacuum compatible plan APO 40x/0.95 light objective and a photomultiplier tube (PMT), retrofitted to a Verios scanning EM (FEI, Eindhoven, The Netherlands). Simultaneously, CL, using the PMT, backscattered electrons, using a circular backscattered electron detector, and secondary electrons, using a through-lens detector, were recorded at either 3 keV and 0.8 nA at a 7 mm working distance. Images were processed and analyzed using Fiji and overlays were created using Adobe Photoshop.

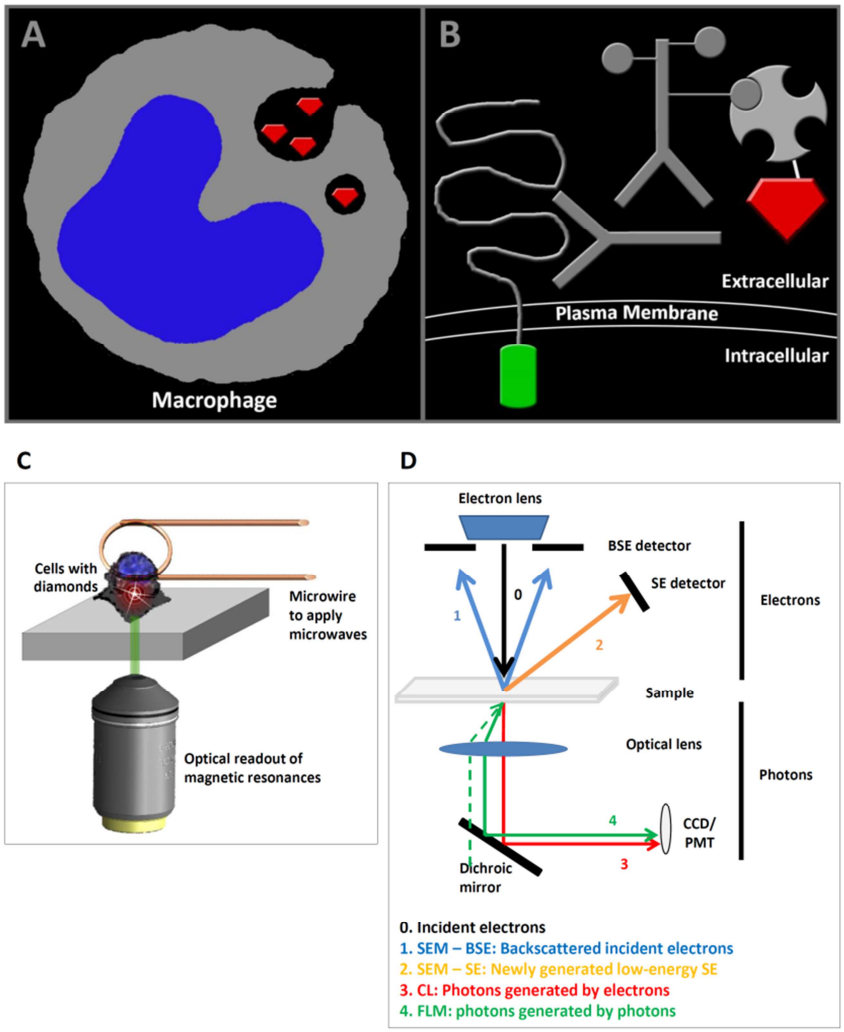

Figure 1 | FND applications in this study. (**a**) Representation of FND40 uptake by macrophages. The diamond particles are phagocytosed by the macrophages and are transported in intracellular vesicles. (**b**) Immunolabeling approach: (1) the extracellular domain of EpCAM, with an intracellular GFP domain, is targeted by a monoclonal antibody (MOC-31); (2) biotinylated rabbit anti mouse IgG is used as a linker for labeling with (3) streptavidin-conjugated FND70 particles. (**c**) Schematic overview of the sample area of a diamond magnetometer for intracellular sensing. The cells, which contain diamond nanoparticles, are in a glass bottom petri dish. A microwire in close proximity is used to excite in the microwave regime. Simultaneously, fluorescence is collected through a microscope objective and a subsequent confocal microscope. (**d**) Schematic overview of integrated light and scanning EM and cathodoluminescence. (0) Primary incident electrons generate (1) backscattered electrons (BSE) and (2) secondary electrons (SE) which can be imaged in a SEM with the respective detectors. Also photons can be generated upon electron beam excitation called (3) cathodoluminescence (CL). Via an optical lens, these photons can be detected with for example a CCD camera or photo multiplier tube (PMT). Furthermore, with an integrated light and electron microscope (4) regular fluorescence imaging can be performed with photon excitation.

Optically detected magnetic resonance (ODMR) measurements

These measurements allow using the FND to read out their magnetic surrounding. Additionally, they offer a way to undoubtedly identify bright spots as FND defects. For magnetic resonance measurements a home built diamond magnetometer (similar to what is used in the community[30, 31], see Fig. 1c for a schematic representation), which is a confocal microscope with built-in microwave electronics, has been used. As described previously macrophage cells where stained to identify cell borders. Borders of HT29 cells where identified via their intrinsic GFP signal. To separate the FNDs signal from the other fluorescent staining a 550 nm long pass filter was used. Signal above 550 nm was attributed to the FNDs. A laser power of 1 mW was used. After scanning an area with cells and identifying FND particles we focused on the FND spots and recorded an optically detected magnetic resonance. The frequency was swept around the expected resonance frequency of the NV centre at 2,87 GHz. This microwave signal was produced with a microwave synthesizer (Hittite HMC-T2100) sending to a homemade antenna (short circuit of a copper wire at the end of a coaxial cable[32], a few micrometer from the sample). Simultaneously, light intensity was collected using an Olympus UPLSAP40x2 NA = 1,3 objective and an Avalanche photodiode (SPCM-AQRF-15-FC) in single photon counting mode. The microwave power was 27 dBm and the acquisition time was 13 min.

Results and discussions

Properties of sub-100 nm FNDs

Recently, attention has gone to relatively large FNDs[33, 34] which show high fluorescent and CL signals[24]. However, for bio-applications small FNDs, approaching the size of biomolecules, are preferred. First, we set out to characterize the FND40 and FND70 dispersions. When imaged with EM using secondary electron (SE) detection, the different FND types indeed show different sizes when spotted on ITO glass. However, both samples also show a substantial size variation, as can be seen for the FND70 in Fig. 2a. Figure 2b shows the size distributions measured over 5051 and 1141 particles for FND70 and FND40 respectively, which confirm the observed size polydispersity. Distributions are markedly non-Gaussian with average sizes of 54 ± 2 6 nm and 67 ± 37, respectively. Next, fluorescence characteristics were assessed. Excitation with 561 nm laser gave the highest emission intensity, within the red spectrum with a maximum around 660 nm. Furthermore, emission intensity increases with FND size, which can be explained by the higher amount of NV-centers in FND70 (>300) compared to FND40 (10–15). Besides light-excited fluorescence, also electron-excited CL is observed from the FNDs. CL intensity measurements (Fig. 2c) were performed simultaneously with the size measurements. These also displayed strong variations, with a few very bright FNDs and a majority of weak to dim FNDs. Note that fluorescence originates from both neutral (NV°) and negatively charged (NV^-) vacancy centers, while CL has been reported to only originate from NV° centers. Spectral measurements (see Supplementary Fig. S1) confirmed NV°-only CL. FND size to CL intensity correlation (Fig. 2d) shows that brightest CL originates from the relatively larger FNDs, as may be expected from a larger number of NV-centers in bigger particles together with reduced surface quenching of excitations. However, it is also observed that through the entire size range strong particle-to-particle variations in CL intensity occur. Thus, there are relatively CL-bright small FNDs together with relatively CL-dim larger FNDs. Factors accounting for this may be the unknown out-of-plane diameter of the non-spherical FNDs (although we note that we did not observe correlation between CL and SE intensity), variation in the number of vacancy centers per particle and/or different interparticle ratios of NV° vs NV^-. Despite the relatively low fluorescence of FND40, the signal/noise measurements as performed on spotted FNDs directed us to evaluate the benefits of smaller size for bio-applications.

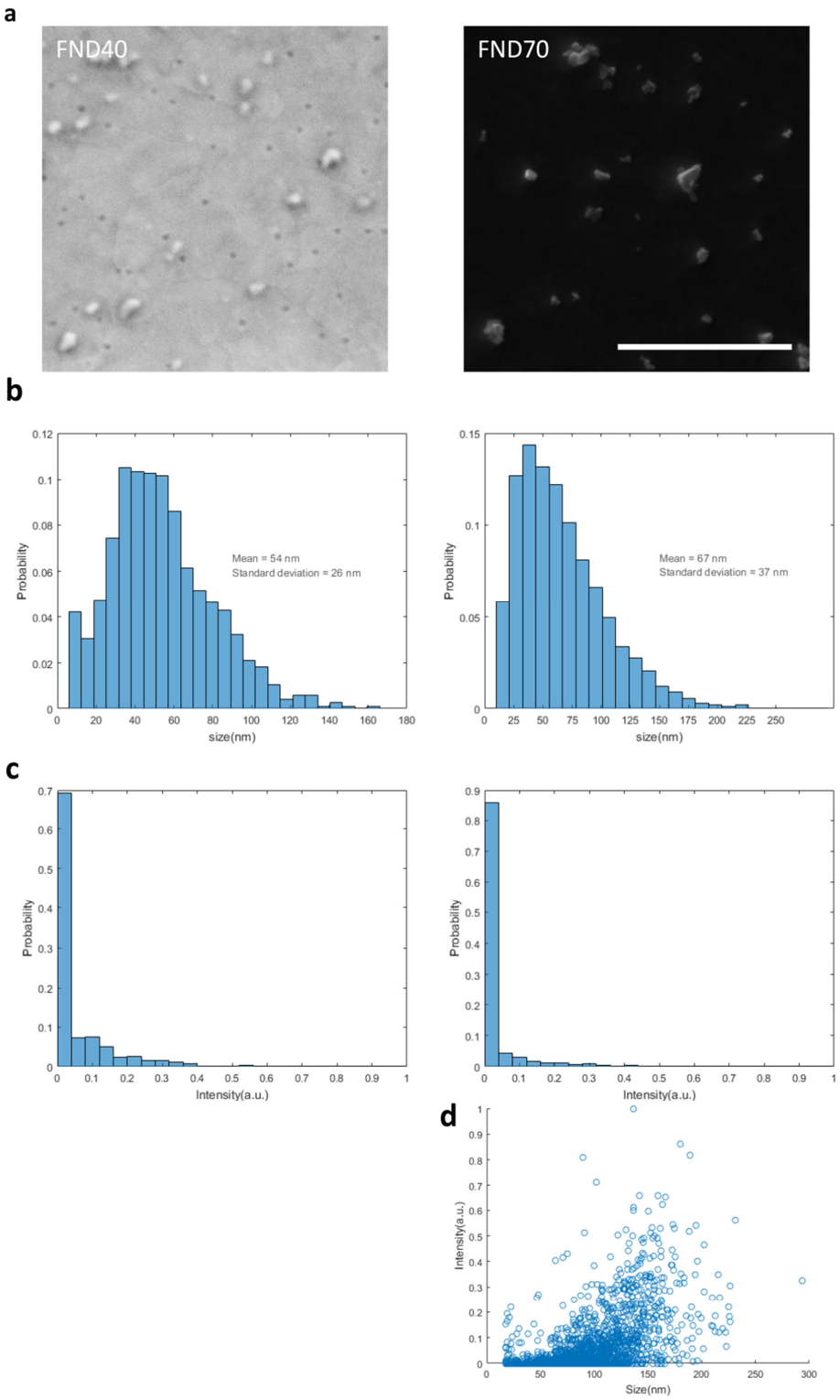

Figure 2 | Properties of two different sizes sub 100 nm FNDs. (**a**) Secondary electron images of 40 nm and 70 nm FNDs. (**b**) Size distributions of FND40 (left) and FND70 (right) were defined as the square root of the surface area of the diamonds as detected with secondary electrons as shown in A. (**c**) CL intensity. (**d**) The correlation of diamond size with CL intensity for FND70. Bar: 1 µm.

FND40 uptake by macrophages visible with EM and CL

Recently, FND ingested by different cell types have been shown[9, 10]. We used macrophages for their uptake efficiency as a proof of principle set up for our different imaging approaches (Fig. 1). Indeed, FND40 are taken up by macrophages as assessed by their fluorescence from within the cells (Fig. 3a). Using our home written script for the FIJI software we estimated an average of 210 internalized particles per cell. The identity of the 40 nm diamonds was further confirmed by ODMR measurements revealing the presence of FND40 particles inside the cells (Fig. 3b). The characteristic NV spectrum (a double dip at the resonance frequency of 2.87 GHz) uniquely identifies diamond particles. Next, these macrophages were embedded for subsequent EM. The fluorescence of the FNDs was preserved after conventional epon embedding, including post fixation using 1% osmiumtetroxide (Fig. 3c). The retention of fluorescence could be explained since their NV-centres are embedded in the diamond structure and therefore not accessible for osmium quenching. Loss of fluorescence is often a hurdle in CLEM and maintenance is highly desired especially when an integrated light and electron microscopy approach is used (reviewed in de Boer *et al*.[1]). Although engineered osmium-resistant fluorescent proteins and dedicated embedding protocols for fluorescence preservation exist[35-38] this may come at the expense of the ultrastructure preservation. Here, however, ultrastructure is preserved, since we used conventional osmium post-fixation and epon embedding (Fig. 3d,e). Fluorescence from the EM samples is however still diffraction limited, precluding precise localization when overlaid with EM data. In order to achieve high resolution localization we utilized the CL properties of the FNDs which have been shown before with single nanodiamonds and for larger FND150 in cells[5, 24, 25]. Clearly, FND40 show up in CL on a dark background (Fig. 3d,e). Variations in CL intensity between different FND40 are observed, e.g., in Fig. 3d where two diamonds stand out and others appear dimmer, likely due to variations in size and number of NV centers contained in the particles. An advantage of SEM is that low energy SEs can be detected simultaneously. As diamond has an exceptionally high SE yield at few keV electron energy, which may even be more pronounced for defected diamond[39], and SEs can readily escape from the small particles, the FND40 stand out particularly well in the SE image (Fig. 3d). This confirms that the higher CL originates from the relatively larger particles. Compared to the SE image, a halo around the diamonds appears in CL, which we attribute to proximity excitation due to BSE or SE excited in the tissue. When overlaid with backscattered electron (BSE) data we find localisation of FND40 particles within the ultrastructure context of macrophages. This approach reveals different stages of phagocytosis including engulfment as the plasma membrane extrudes around the particles, which are still extracellular (Fig. 3d), and FNDs in phagosomes shown by the presence of a membrane around the particles (Fig. 3e).

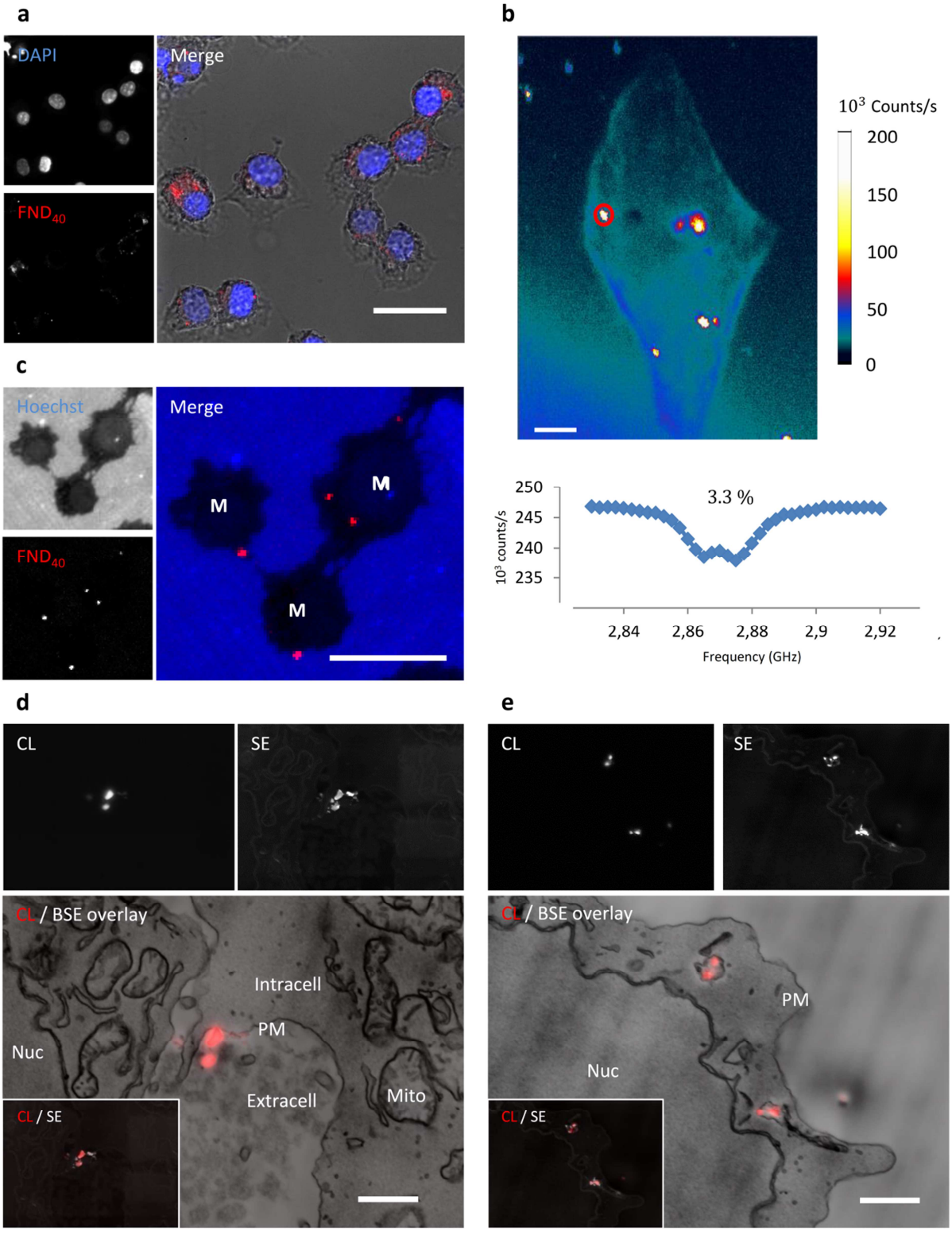
a
DAPI
Merge
FND40
b
10³ Counts/s
200
150
100
50
0
c
Hoechst
Merge
FND40
M
M
M
250
245
240
235
10³ counts/s
3.3 %
2,84
2,86
2,88
2,9
2,92
Frequency (GHz)
d
CL
SE
CL / BSE overlay
Intracell
PM
Nuc
Extracell
Mito
CL / SE
e
CL
SE
CL / BSE overlay
PM
Nuc
CL / SE

Figure 3 | FND40 uptake by macrophages assessed by fluorescence microscopy, EM, magnetic resonance and CL. (**a**) Pre-embedding fluorescence of FND40 internalized by macrophages as seen in the diffraction interference contrast (DIC) merged picture. Nuclei are counterstained with DAPI. (**b**) Magnetic resonance spectra where taken at the bright spots identified as diamonds. The graph shows the spectrum taken at the red circle. 3,3% is the contrast between the resonance line and the background for 1 run. (**c**) Fluorescence from FND40 in a 300 nm semi-thin epon section from macrophages (M). Nuclei are counterstained with Hoechst; blue outside the cells is autofluorescence caused by epon. (**d**,**e**) CL, SE and the CL overlaid with BSE images of FND40 particles. (**d**) extracellular of the plasma membrane during engulfing. The lower left corner shows an overlay of CL and SE of the same image. Some particles are clearly observed with SE and not with CL. (**e**) FND40 particles internalized by the macrophage as they are inside vesicles. The lower left corner shows an overlay of CL and SE of the same image. Some particles are observed with SE and not with CL, but also particles observed with CL are not visible with SE. Note that single FND40 particles within one vesicle can be resolved by CL. M: macrophage; Nuc: nucleus; Intra: intracellular; Extra: extracellular; PM: plasma membrane; Mito: mitochondria; CL: cathodoluminescence; SE: secondary electrons; BSE: Backscattered electrons. Bars: (**a**) 10 µm, (**b**) 12 µm, (**c**), 10 µm, (**d**,**e**) 1 µm.

FND70 allow immunolabeling and superresolution detection

Given the notion that FND40 particles are detectable with CL and EM at high resolution in uptake assays, FND70 was conjugated to streptavidin for generic immunolabeling application. As a proof of principle we immuno-targeted the extracellular domain of EpCAM-GFP expressed by HT29 cells[27] (Fig. 4a) using a pre-embedding approach without permeabilization to maintain both antigenicity and ultrastructure. Immunolabeling was successful as compared to non-EpCAM-GFP expressing control cells, but sparse compared to smaller QD655 particles (~10 nm). On the other hand, FND70 can be used in ODMR (Fig. 4b). Overlap of the EpCAM positive and FND positive pixels for the cell cluster of Fig. 4a was 22.9%. This imaging mode not only allows proofing that the optical signal comes from diamond particles but also opens up the possibility to measure chemicals or certain properties in the surrounding of the particles via ODMR. Moreover, immunolabeling was detected with CL in EM samples and overlaid with BSE data for high resolution localization (Fig. 4c). Again, FNDs also stand out in SE detection (Fig. 4c). Also very dim or even non-fluorescent nanodiamonds, e.g., due to a lack of CL-active defect centers, show up in SE. On the other hand, only surface exposed particles, would be visible in SE, as for deeper (>few nanometers) lying FNDs, the low energy SEs cannot escape the sample. CL of FNDs for superresolution imaging has mostly been explored using single particles[5, 40] even with detecting individual defect centers within one nanodiamonds[39]. Here, we show for the first time CL of relatively small-sized FNDs within a biological context (Figs 1d,e and 3c), compared to what others have shown before[24] to achieve superresolution imaging. Bio-application of CL correlation with EM has been applied before with different nanoparticles, but size is often an issue[9, 10].

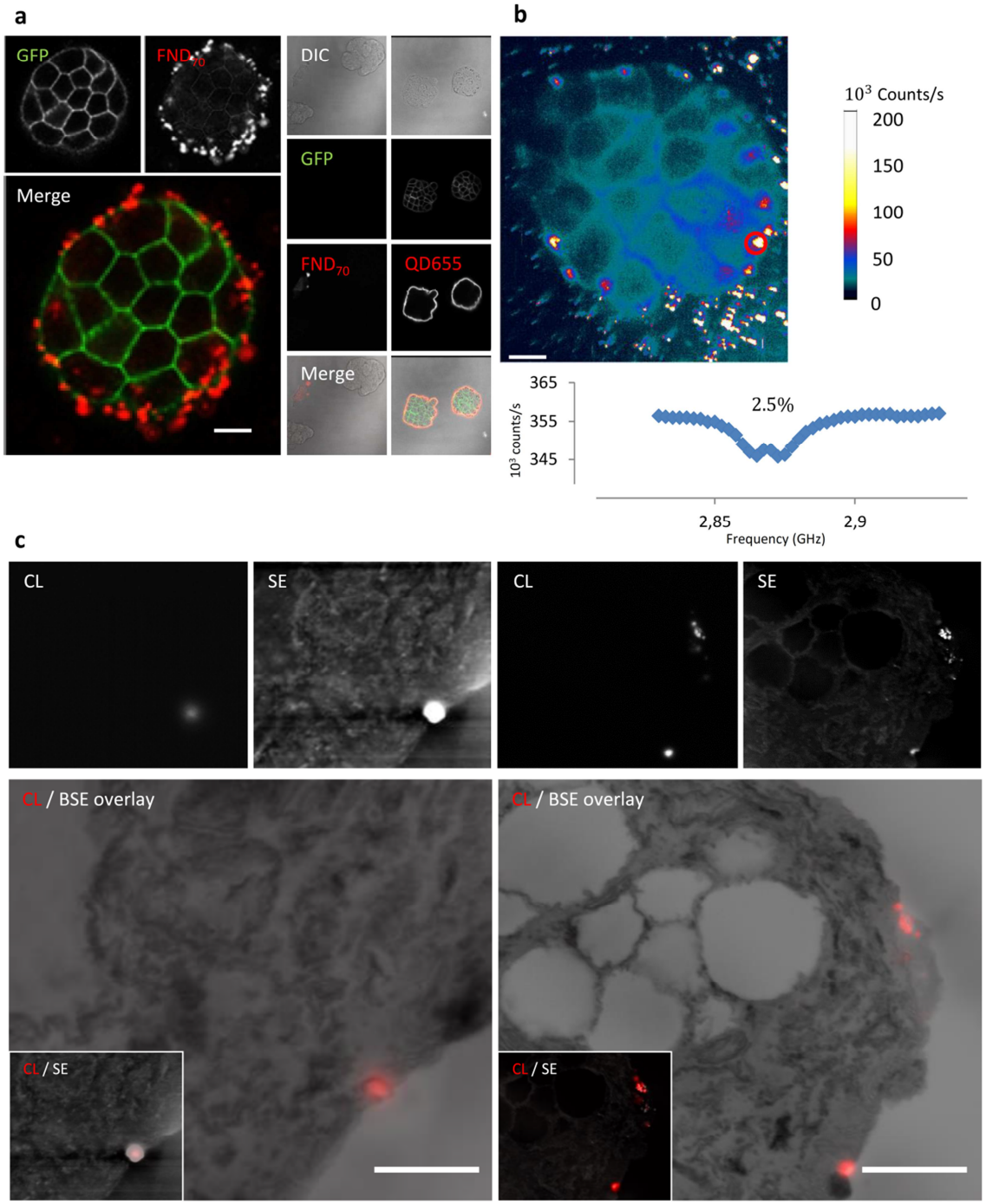

Figure 4 | Multimodal analysis of FND70 immunolabeling of EpCAM-GFP HT29 cells. (**A**) Streptavidin-conjugated FND70 labels at the outside of a HT29 cell cluster. The context of different cells within the cluster is shown by GFP. Negative controls (left column) and positive controls (right column; QD655) are shown. No FND70 labeling of non-transfected negative controls is observed, context is shown by diffraction interference contrast (DIC) as EpCAM-GFP is absent. (**B**) Magnetic resonance spectra where taken at the bright spots identified as diamonds. The lower part of the figure shows the spectrum taken at the circled spot. 2,5% is the contrast between the resonance line and the background for 1 run. (**C**) CL, SE and the CL overlaid with BSE images of FND70 labeling an HT29 cell cluster at the cell surface. Note that in the right image single FND70 particles are resolved with CL. Abbreviations as in Fig. 3. Bars: (**A**,**B**) 25 µm, (**C**) 1 µm.

Conclusions

FNDs have the advantage that they are stable and bleach resistant. They remain fluorescent after osmium fixation, and can also be detected using CL in samples for analysis with EM or integrated microscopes. The CL allows better localization based on the electron beam excitation rather than on the diffraction-limited light detection. Also, FNDs can be used to generate optically detected magnetic resonance signals allowing nanoscale magnetometry. We show proof-of-principle that all these FND properties can be used with small 40 nm and 70 nm particles using uptake assays or immunolabeling. Given the progress made in the last 10 years with using other nanoparticle, e.g., quantum dots, and labels for bioapplications, our results provide a first lead to further develop FNDs for life science research. This might include smaller, differently conjugated or more homogenous particle distributions. Our proof-of-principle of using multi-modal imaging with small FNDs demonstrates (i) fluorescence in EM prepared samples, (ii) CL, (iii) SE and BSD detection, and (iv) magnetometry detection, which will open up possibilities to gain additional information on the magnetic surrounding of the particles.

Acknowledgments

R.S. acknowledges financial support from FOM projectruimte grant number FOM-G-36. F.P.M. is grateful for a CONICYT scholarship from the Chilean Government. We acknowledge financial support from the Netherlands Organization for Scientific Research (ZonMW91111006; “Microscopy Valley” STW12714; STW12718; NWO175-010-2009-023).

References

1. de Boer, P., Hoogenboom, J. P. & Giepmans, B. N. Correlated light and electron microscopy: ultrastructure lights up! *Nat. Methods* **12**, 503-513 (2015).

2. Niitsuma, J., Oikawa, H., Kimura, E., Ushiki, T. & Sekiguchi, T. Cathodoluminescence investigation of organic materials. *J. Electron. Microsc. (Tokyo)* **54**, 325-330 (2005).

3. Nisman, R., Dellaire, G., Ren, Y., Li, R. & Bazett-Jones, D. P. Application of quantum dots as probes for correlative fluorescence, conventional, and energy-filtered transmission electron microscopy. *J. Histochem. Cytochem.* **52**, 13-18 (2004).

4. Giepmans, B. N., Deerinck, T. J., Smarr, B. L., Jones, Y. Z. & Ellisman, M. H. Correlated light and electron microscopic imaging of multiple endogenous proteins using Quantum dots. *Nat Methods* **2**, 743-9 (2005).

5. Glenn, D. R. *et al*. Correlative light and electron microscopy using cathodoluminescence from nanoparticles with distinguishable colours. *Sci. Rep.* **2**, 865 (2012).

6. Narvaez, A. C. *et al*. Cathodoluminescence Microscopy of nanostructures on glass substrates. *Opt. Express* **21**, 29968-29978 (2013).

7. Morrison, I. E. G. *et al*. Multicolour correlative imaging using phosphor probes. *Journal of Chemical Biology* **8**, 169-177 (2015).

8. Furukawa, T. *et al*. High-resolution microscopy for biological specimens via cathodoluminescence of Eu- and Zn-doped Y2O3 nanophosphors. *Opt. Express* **21**, 25655-25663 (2013).

9. Fukushima, S. *et al*. Y2O3:Tm,Yb nanophosphors for correlative upconversion luminescence and cathodoluminescence imaging. *Micron* **67**, 90-95 (2014).

10. Fukushima, S. *et al*. Correlative near-infrared light and cathodoluminescence microscopy using Y2O3:Ln, Yb (Ln = Tm, Er) nanophosphors for multiscale, multicolour bioimaging. *Sci. Rep.* **6**, 25950 (2016).

11. Schirhagl, R., Chang, K., Loretz, M. & Degen, C. L. Nitrogen-vacancy centers in diamond: nanoscale sensors for physics and biology. *Annu. Rev. Phys. Chem.* **65**, 83-105 (2014).

12. Zhu, Y. *et al*. The biocompatibility of nanodiamonds and their application in drug delivery systems. *Theranostics* **2**, 302-312 (2012).

13. Mohan, N., Chen, C. S., Hsieh, H. H., Wu, Y. C. & Chang, H. C. In vivo imaging and toxicity assessments of fluorescent nanodiamonds in Caenorhabditis elegans. *Nano Lett.* **10**, 3692-3699 (2010).

14. Nagl, A., Hemelaar, S. R. & Schirhagl, R. Improving surface and defect center chemistry of fluorescent nanodiamonds for imaging purposes--a review. *Anal. Bioanal Chem.* **407**, 7521-7536 (2015).

15. Faklaris, O. *et al*. Detection of single photoluminescent diamond nanoparticles in cells and study of the internalization pathway. *Small* **4**, 2236-2239 (2008).

16. McGuinness, L. P. *et al*. Quantum measurement and orientation tracking of fluorescent nanodiamonds inside living cells. *Nat. Nanotechnol* **6**, 358-363 (2011).

17. Pope, I. *et al*. Coherent anti-Stokes Raman scattering microscopy of single nanodiamonds. *Nat. Nanotechnol* **9**, 940-946 (2014).

18. Hemelaar, S. R. *et al*. The interaction of fluorescent nanodiamond probes with cellular media. *Mikrochim. Acta* **184**, 1001-1009 (2017).

19. Balasubramanian, G. *et al*. Nanoscale imaging magnetometry with diamond spins under ambient conditions. *Nature* **455**, 648-651 (2008).

20. Van Oort, E. & Glasbeek, M. Electric-field-induced modulation of spin echoes of N-V centers in diamond. *Chemical Physics Letters* **168**, 529-532 (1990).

21. Acosta, V. M. *et al*. Temperature dependence of the nitrogen-vacancy magnetic resonance in diamond. *Phys. Rev. Lett.* **104**, 070801 (2010).

22. Maze, J. R. *et al*. Properties of nitrogen-vacancy centers in diamond: the group theoretic approach. *New Journal of Physics* **13**, 025025 (2011).

23. Zhang, H. *et al*. Silicon-vacancy color centers in nanodiamonds: cathodoluminescence imaging markers in the near infrared. *Small* **10**, 1908-1913 (2014).

24. Nagarajan, S. *et al*. Simultaneous cathodoluminescence and electron microscopy cytometry of cellular vesicles labeled with fluorescent nanodiamonds. *Nanoscale* **8**, 11588-11594 (2016).

25. Nawa, Y. *et al*. Multi-color imaging of fluorescent nanodiamonds in living HeLa cells using direct electron-beam excitation. *Chemphyschem* **15**, 721-726 (2014).

26. Ong, S. Y., Chipaux, M., Nagl, A. & Schirhagl, R. Shape and crystallographic orientation of nanodiamonds for quantum sensing. *Phys. Chem. Chem. Phys.* **19**, 10748-10752 (2017).

27. De Leij, L., Helrich, W., Stein, R. & Mattes, M. J. SCLC-cluster-2 antibodies detect the pancarcinoma/epithelial glycoprotein EGP-2. *Int J Cancer Suppl* **8**, 60-3 (1994).

28. Schnell, U., Kuipers, J. & Giepmans, B. N. EpCAM proteolysis: new fragments with distinct functions? *Biosci. Rep.* (2013).

29. Schindelin, J. *et al*. Fiji: an open-source platform for biological-image analysis. *Nat. Methods* **9**, 676-682 (2012).

30. Loretz, M., Pezzagna, S., Meijer, J. & Degen, C. L. Nanoscale nuclear magnetic resonance with a 1.9-nm-deep nitrogen-vacancy sensor. *Appl. Phys. Lett.* **104**, 033102 (2014).

31. Ofori-Okai, B. K. *et al*. Spin properties of very shallow nitrogen vacancy defects in diamond. *Phys. Rev. B* **86**, 081406 (2012).

32. Chipaux, M. *et al*. Magnetic imaging with an ensemble of nitrogen-vacancy centers in diamond. *The European Physical Journal D* **69**, 166 (2015).

33. Lin, H. H. *et al*. Tracking and Finding Slow-Proliferating/Quiescent Cancer Stem Cells with Fluorescent Nanodiamonds. *Small* **11**, 4394-4402 (2015).

34. Chu, Z. *et al*. Rapid endosomal escape of prickly nanodiamonds: implications for gene delivery. *Sci. Rep.* **5**, 11661 (2015).

35. Peddie, C. J. *et al*. Correlative and integrated light and electron microscopy of in-resin GFP fluorescence, used to localise diacylglycerol in mammalian cells. *Ultramicroscopy* **143**, 3-14 (2014).

36. Paez-Segala, M. G. *et al*. Fixation-resistant photoactivatable fluorescent proteins for CLEM. *Nat. Methods* **12**, 215-218 (2015).

37. Kukulski, W. *et al*. Correlated fluorescence and 3D electron microscopy with high sensitivity and spatial precision. *J. Cell Biol.* **192**, 111-119 (2011).

38. Kukulski, W. *et al*. Precise, correlated fluorescence microscopy and electron tomography of lowicryl sections using fluorescent fiducial markers. *Methods Cell Biol.* **111**, 235-257 (2012).

39. Ascarelli, P. *et al*. Secondary electron emission from diamond: Physical modeling and application to scanning electron microscopy. *J. Appl. Phys.* **89**, 689-696 (2001).

40. Tizei, L. H. & Kociak, M. Spectrally and spatially resolved cathodoluminescence of nanodiamonds: local variations of the NV(0) emission properties. *Nanotechnology* **23**, 175702-4484/23/17/175702. Epub 2012 Apr 5 (2012).

41. Torrano, A. A. *et al*. A fast analysis method to quantify nanoparticle uptake on a single cell level. *Nanomedicine (Lond)* **8**, 1815-1828 (2013).

Supplementary information

Quantification of diamonds in cells

In order to quantify internalized particles we have developed a script to be used in the image analysis software FIJI (Fiji Is Just ImageJ, https://fiji.sc/). The analysis was divided into three phases: Cell Selection, Masking and Particle Analysis. During the first phase, the images were visually inspected and random cells were selected for the analysis. Cells which aggregates associated with the cell membrane were rejected to prevent false positive results. The images were composed of several slices (z-stacks), the cell's region was defined in all the three dimensions. In the horizontal plane, the selection considered an area containing only the cell of interest. In the height, the first and last slices containing the cell were identified. As a result, the first phase defines a volume that holds only the cell of interest. In the Masking phase, that volume is molded in order to resemble the shape of the cell. The image is converted to binary (using the Isodata algorithm to calculate the threshold)[41] then the cell's perimeter is detected in every slice. To find the inner volume of the cell, the program shrinks the cell's region in order to exclude the cell membrane from the analysis. The final step uses a special function of Fiji, which analyzes the particles found in a region. Applying this function to the masked image, it is possible to directly obtain the amount of particles (connected components) in the specified region. The performance of this process is set mainly by the parameter "threshold". The threshold is used to separate the background light from the signal emitted by the FNDs. Every pixel with intensity less than the threshold is assumed as background and deleted from the image (set as black) while every pixel with an intensity greater or equal than the threshold is assumed as part of a particle. To find an adequate value for this parameter, the image was visually inspected and different values were probed. Finally, the election was made in favor removing more background signal, but without deleting particles clearly identified, which showed no signal inside yeast cells without FNDs. As a result, the process provides the number of particles, which are found in every analyzed cell.

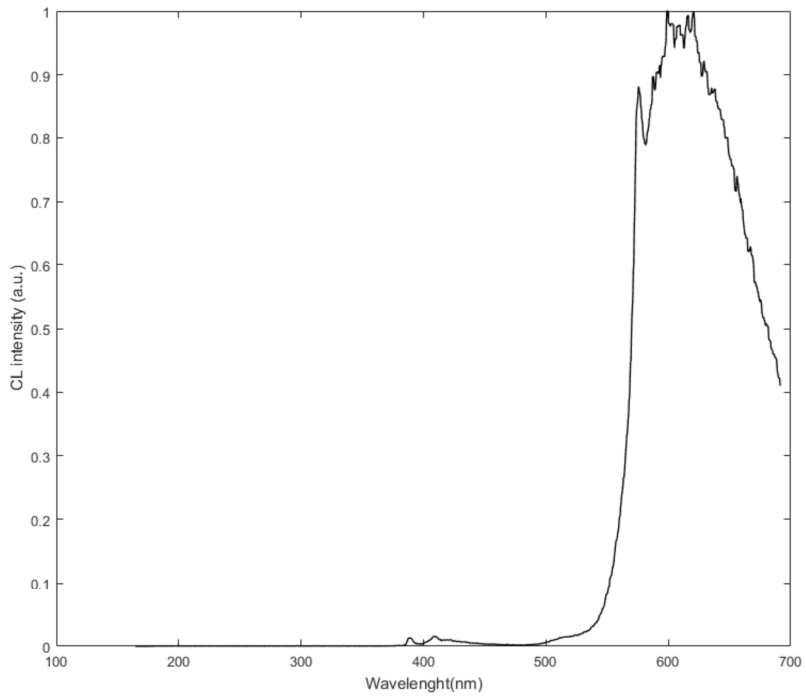

Figure S1 | Cathodoluminescence spectrum from NV0 recorded while excited with the electron beam.

Chapter 4b

Multi-color electron microscopy by element-guided identification of cells, organelles and molecules

Marijke Scotuzzi[1#], Jeroen Kuipers[2#], Dasha I. Wensveen[1#], Pascal de Boer[2], Kees (C.)W. Hagen[1], Jacob P. Hoogenboom[1#] and Ben N.G. Giepmans[2#]

[1]Department of Imaging Physics, Delft University of Technology, Delft, The Netherlands, [2]Department of Cell Biology, University Medical Center Groningen, Groningen, The Netherlands.

[#] Denotes equal contribution

Scientific Reports (2017) 7;7:45970. doi: 10.1038/srep45970

Abstract

Cellular complexity is unraveled at nanometer resolution using electron microscopy (EM), but interpretation of macromolecular functionality is hampered by the difficulty in interpreting grey-scale images and the unidentified molecular content. We perform large-scale EM on mammalian tissue complemented with energy-dispersive X-ray analysis (EDX) to allow EM-data analysis based on elemental composition. Endogenous elements, labels (gold and cadmium-based nanoparticles) as well as stains are analyzed at ultrastructural resolution. This provides a wide palette of colors to paint the traditional grey-scale EM images for composition-based interpretation. Our proof-of-principle application of EM-EDX reveals that endocrine and exocrine vesicles exist in single cells in Islets of Langerhans. This highlights how elemental mapping reveals unbiased biomedical relevant information. Broad application of EM-EDX will further allow experimental analysis on large-scale tissue using endogenous elements, multiple stains, and multiple markers and thus brings nanometer-scale 'color-EM' as a promising tool to unravel molecular (de)regulation in biomedicine.

Introduction

Precise identification and localization of molecules, organelles, cells and other biological structures is a key step to unravel how these act to regulate biology. Electron microscopy (EM) provides nanometer-resolution images of the cellular ultrastructure, which can be automatically collected to allow large field-of-view or three-dimensional imaging at high magnification[1]. However, data analysis is hampered by visual interpretation of grey-scale images, especially for rare finding or unanticipated events in large datasets. Fluorescence microscopy aids to identify biomolecules[2-5], but lacks structural context. Correlated light microscopy and EM (CLEM)[6, 7] allows fluorescence-guided analysis of EM data, but fluorescence retention during EM sample preparation and overlay of images differing order-of-magnitude in resolution may be technically challenging[6, 7]. In search for a broadly implementable technique to define molecules, organelles and cells at high resolution within mammalian tissue, we decided to implement element-guided identification using energy dispersive X-ray analysis (EDX). In mammalian tissue, detection sensitivity of typically low percent elements in combination with high count rates from carbon and oxygen as well as radiation damage have limited broad application of EDX imaging for a long time. EDX spectroscopy and imaging on cryo-fixed tissue has been pioneered by Somlyo and coworkers[8-10], and pioneering studies have mainly focused on detection of a few selected elements in small regions at relatively low resolution (see for example[11, 12]). Leapman and co-workers applied and pioneered electron energy loss spectroscopy (EELS) in transmission EM to discriminate cells based on sequential analysis of three elements[13], and recently Tsien and coworkers presented EELS-based two-color discrimination of localized deposits of lanthanides[14]. EDX allows direct identification of many elements in parallel, either present endogenously and/or introduced by staining or labeling, at high count rates using the latest generation of silicon drift detectors (SDD). We find that this paves the way for straight-forward high-resolution elemental mapping in mammalian tissue compatible with standard EM protocols. The resulting elemental color-maps can be overlaid with the conventional EM data to allow data-mining based on composition *and* structure, rather than morphology only. We apply this approach in large field-of-view EM ("nanotomy")[15-17] on pancreas from a rat model for Type 1 diabetes (T1D). EDX not only allows us to identify organelles and biomolecular labels at high resolution, but also to show that distinct granules have typical elemental fingerprints. EDX-guided elemental fingerprinting in combination with large-scale EM reveals cells that contain both hormones and exocrine granules in the pancreas. Given that a sensitive EDX SDD is a standard retrofit add-on to electron microscopes, we foresee broad application of such a technique in both label free and studies using exogenous tracers. This approach is applicable to both life science and biomedical research. Such a technique increases the depth of information with the color coding of structures based on their elemental profile and brings an objective analysis tool to EM imaging.

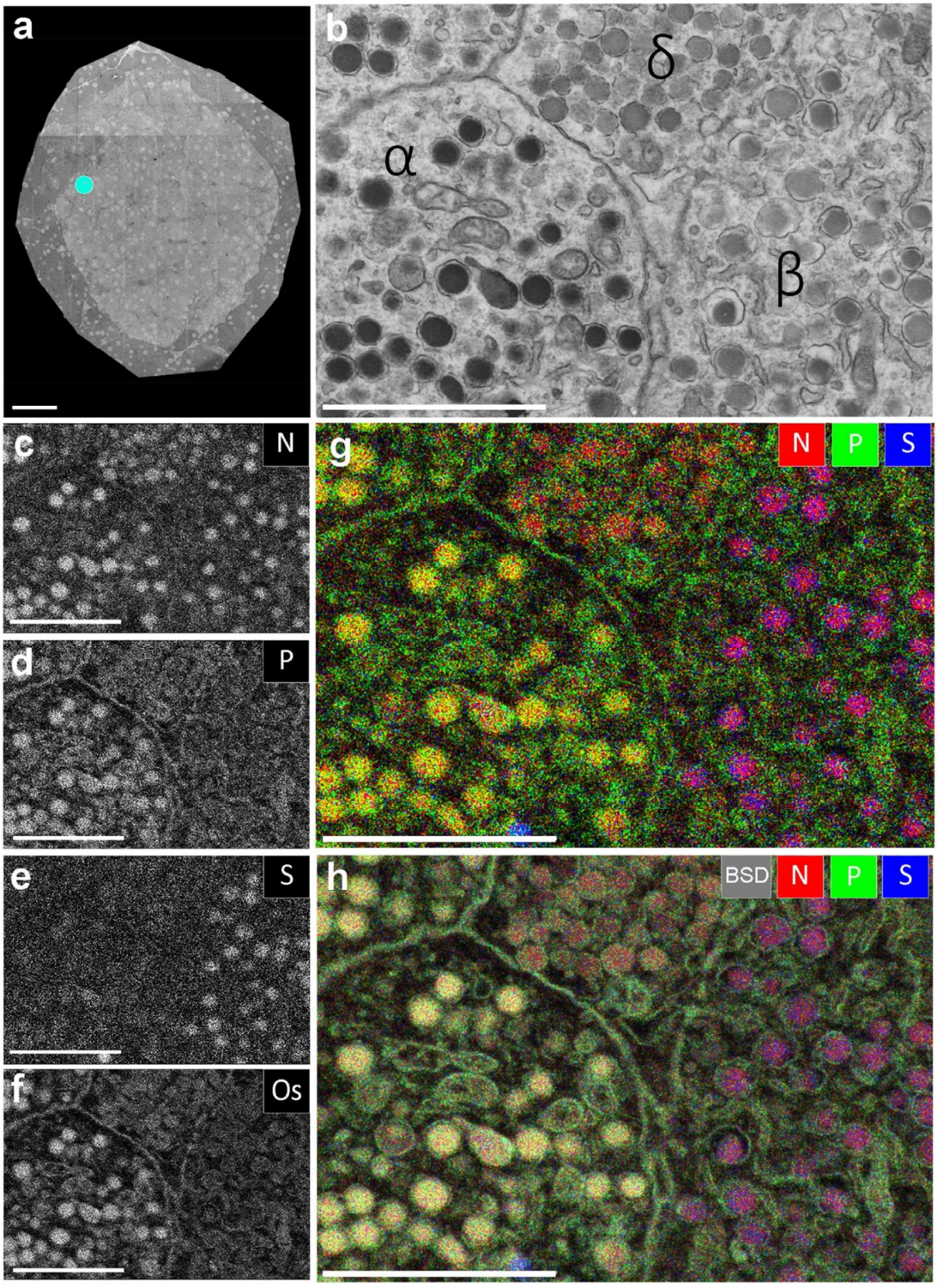

Figure 1 | EDX defines cell-types and subcellular structures and organelles in EM images. (**a**) 100 nm thin cross-section of an entire rat islet of Langerhans imaged at 2.5 nm pixel size (STEM). Full high-resolution data is available via nanotomy.org (see suppl. material). (**b**) Area of interest (indicated in a; cyan dot) shows parts of four cells with different granules based on grey levels and morphology. (**c–f**) Elemental content in the ROI as indicated. (**g**) Overlay of N (red), P (green) and S (blue) allows identification of cells and granules based on elemental content. (**h**) Overlay of back scatter ICD image (greyscale) over the color-image of g. Bars: 50 µm (**a**) and 2 µm (**b–h**). Maps of other elementals are available as Fig.S1.

Results

Large-scale EM of standard prepared rat pancreas fixed with aldehydes and osmium, embedded in epon (Fig. 1a; full resolution at www.nanotomy.org) was recorded using scanning transmission EM[17, 18]. An endocrine area with three different cell types was selected (Fig. 1b). Traditional visual grey-scale analysis presumptively identifies these as a somatostatin-producing delta cell (top middle), a glucagon-producing alpha cell (left) and an insulin-producing beta cell (right). EDX analysis reveals informative maps of nitrogen, phosphor, sulphur and osmium (N, P, S, Os respectively) localization (Fig. 1c–f; and Fig. 1g,h for overlays; see Fig. S1 for more elemental results). N is abundant in all granules, as expected for highly concentrated peptides, irrespective of presumed cell identity. S is most abundant in insulin granules, as expected from the high cysteine content. The glucagon granules are found to stand out in the P map, whereas somatostatin shows neither pronounced S or P and is thus recognized on the sole presence of N. These compositional differences between granules are also revealed in qualitative comparison of the full EDX spectra (Fig. S4) and are furthermore reproduced using alternative, osmium-free sample preparation (Fig. S5). P maps also show condensed heterochromatin in the nucleus and the very dense endoplasmic reticulum network of the exocrine cells where P-rich RNA is translated. At high resolution also mitochondria are in the P map, which may reflect the abundance of phospholipids and ATP production. Overlay of the N, P, and S maps (Fig. 1g) clearly discriminates, in color indicating their elemental fingerprint, the separate granules. Not surprisingly, addition of the Os map, used as fixative and the only EM contrasting agent, adds the electron density determined by back scattered electron detection (BSD) from the EM image (Fig. 1h).

High-resolution definition of targets by EDX can further aid in molecular identification or assist in validation when applied to the recognition of elements specifically deposited at biomolecules of interest using antibody labeling. We choose a 1H6 monoclonal antibody that was raised against guanine quadruplexes (G4)[19] and an anti-insulin antibody[18], for which we previously established immunolabeling on epon sections[18]. Primary antibodies were subsequently labeled with secondary antibodies conjugated to gold (Au) and Cadmium-Selenide (CdSe)-based quantum dots (QDs), elements that are (nearly) absent in mammals[20]. Nanotomy was performed (Fig. 2a; www.nanotomy.org) and an area was selected for EDX analysis (Fig. 2b). Shown is part of an insulin-producing beta cell, with in the top left a nucleus with euchromatin (white, light grey) and darker heterochromatin, especially present near the nuclear envelope. The 1H6 antibody developed against G4 structures shows strong reactivity in areas of heterochromatin[19], as also can be deducted from the electron-dense gold particles. In the cytosol, the presence of mitochondria and insulin-granules is clearly seen, the latter decorated with the electron-dense quantum dots (Fig. 2b). EDX analysis for Cd-based QDs, S-enriched insulin, Au (G4) and P-rich heterochromatin (Fig. 2c–f respectively; Fig. S4 for full elemental results) reveals that both Au and QDs are readily detected by EDX. Thus unambiguous identification of targets in biosamples by elemental analysis can be performed in addition to analysis by grey levels, size, or shape[21, 22]. Note the high signal to noise ratio and co-localization of Cd (QDs; green) with S (insulin; blue), but not Au (1H6 antibody raised against G4; red) in the overlay (Fig. 2g). Similarly, Au (G4, red) localizes to P-rich areas in the nucleus (heterochromatin, blue; see also spectral data in Fig. S5), whereas the Cd (QDs, green) signal is enclosed within P rings (blue) that likely represent phospholipid membranes of the vesicles (Fig. 2h). Thus, EDX analysis allows for high resolution identification of targets in conjunction to endogenous elemental composition in mammalian tissues.

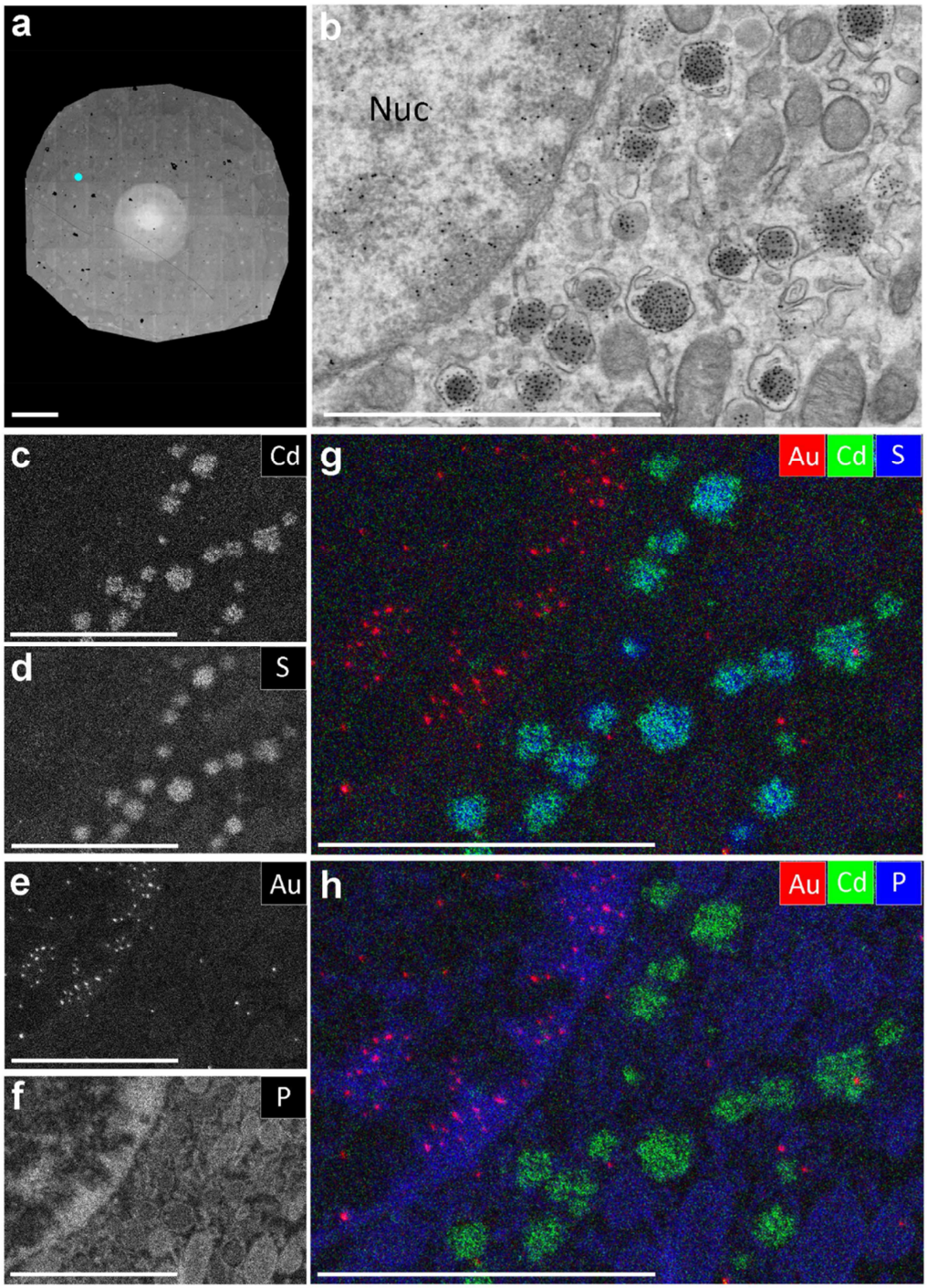

Figure 2 | Immuno-based identification of peptides and G4-DNA structures and endogenous elements. (**a**) Section of an islet immuno-labeled for G4 (10 nm immunogold) and insulin (QD655). The white area in the middle is an electron-beam pre-exposure artefact, but not hampering data analysis. Full resolution is available via nanotomy.org. (**b**) Zooming into the data reveals gold particles in the nucleus (upper left part) and quantum dots in insulin granules. Labels are identified based on grey levels and morphology. (**c**–**f**) Elemental content in the ROI as indicated. (**g**,**h**) Overlay of Au (red), Cd (green) and S (blue; g) or P (blue; h) allows identification of G4 structures based on gold presence and insulin granules based on Cd content. Note the localization of Cd on S-enriched insulin granules (**g**) and localization of Au to heterochromatin regions enriched in P in the nucleus (h). Bars: 50 µm (a) and 2 µm (**b**–**h**). See for more elements Fig. S2 and spectral analysis Fig. S6.

To explore EDX for biomedical microscopy, we used embedded material from our previous studies[15], namely a diabetic prone rat. 90% of these rats spontaneously develop diabetes, with the blood sugar level as an indication for the diabetic state. This experimental animal had not developed diabetes, and showed no signs of insulitis[15] (Figs 1a, 2a, 3a and dataset). Unexpectedly, typical distinct vesicles within one cell are present at multiple locations. These multi-vesicle containing cells are at the border of the endocrine Islet of Langerhans and the surrounding exocrine tissue, the latter readily identifiable by the abundant endoplasmic reticulum and large zymogen vesicles (Fig. 3b, top). The adjacent cell has all characteristics of an endocrine cell (Fig. 3b, bottom). Note the presence of the small granules with a halo (typical for insulin) and other small granules showing an overall high electron density (typical for glucagon), but also large vesicles that resemble the zymogen granules in the exocrine tissue. Using the elemental characteristics to discriminate granules (Fig. 1), we analyzed the distribution of N, P and S (Fig. 3c–e; full elemental results in Fig. S3). Three distinct granules with characteristics of zymogen (N; red), glucagon (N in red and P in green, yellow appearance of coincidence) and insulin (N in red and S in blue, purple appearance) are present (Fig. 3f), which is more prominent at higher zoom (Fig. 3g). Color-coding of the backscatter image in green, a signal mainly caused by Os, allows to superpose the signal created by Os enriched in membranes (Fig. 3h). Interpretation of the multi-hormone and zymogen containing area is modelled on the STEM image (Fig. 3i). Thus, only with EM three distinct granules can be conclusively identified within the same cell and EDX shows the different composition based on different elemental ratios, thus without prior knowledge or anticipated labeling. Based on these new observations, we decided to substantiate our notion probing protein content, and subsequent optimization of double-immunolabeling confirmed our findings (Fig. 4)

Discussion

EDX imaging strongly aids in analysis of EM-data of mammalian tissue. Compared to previous approaches using EDX-imaging[11, 12], which to our knowledge, have mostly been done on cryo-samples, freeze dried samples and/or unstained epon[23, 24] we used chemical fixation, staining, and dehydration. Nanotomy allows analysis of complete cross sections of Islets of Langerhans, although the use of labels to detect proteins in an immunobased manner may benefit from Tokuyasu-sample preparation, which will be better compatible with epitope recognition, but this is typically performed on smaller sections (reviewed in refs [6, 7]). Together with EM-based enhancements (silver) and immuno-labeling nanoparticles this enables recognition of multiple targets at the EM resolution level.

The use of high-sensitivity silicon drift detectors (SDDs)[25] with high-current, high-resolution SEMs now allows determination of variations in elemental composition and elemental fingerprinting from the subcellular to the nanoscale level. These may be due to natural or enriched variations of endogenous elements, introduced stains (like osmium), and/or specific labels as shown for immunotargeted gold and QDs. Elemental detection has been explored before, mostly EELS focusing on quantitative determination of concentrations of typically one or two elements at the (sub)cellular level (reviewed in refs [26, 27]). The Leapman lab pioneered EELS, which is capable of discriminating insulin and glucagon in cells[13]. An early study on the use of QDs[21] for immunolabeling directly noted the possibilities of elemental detection (EELS), posing that the diversity may be increased by using other elements in nanoparticles[21].

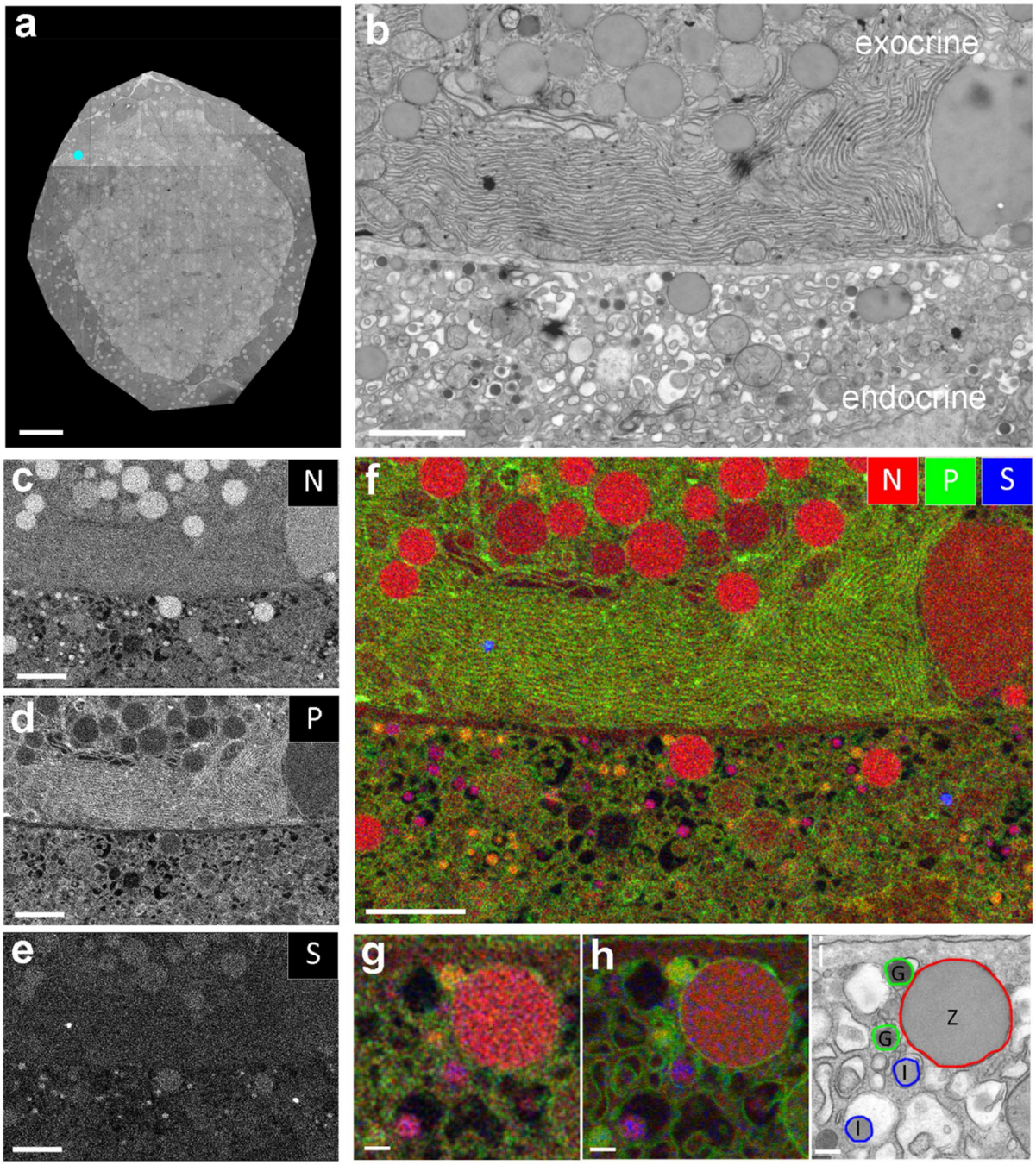

Figure 3 | EDX analysis reveals singles cells that contain exocrine zymogen granules together with endocrine glucagon and insulin. (**a**) Overview as in Fig. 1a. (**b**) Area indicated in (a) by the cyan dot with parts of two cells with different granules based on grey levels and morphology. (**c**–**e**) Elemental maps as indicated. (**f**) Overlay of N (red), P (green) and S (blue) allows identification of cells and granules. (**g**) Zoom of the center part of f, note the small purple and yellow granules, as well as the big red granule, all present in the same cell. (**h**) Same region, with P and S combined with the backscatter image, which was reverted to red. Note the membranes around the vesicles. (**i**) Interpretation of the EDX data on the large scale STEM image showing the presence of three distinct granules in an endocrine cell. Bars: 50 µm (a), 2 µm (**b**–**f**) and 0.2 µm (**g**–**i**). See for more elements Fig.S3.

Implementation of EDX to discriminate ultrastructural features in the rat model for Type 1 diabetes (T1D) revealed distinct granules, believed to be cell-specific, within the same cells (Fig. 3), which have been substantiated by immunolabeling (Fig. 4). Such diversity has been reported in artificial differentiation protocols[28-30]. T1D is caused by loss of the insulin-producing beta cells due to an auto-immune reaction of which the trigger is not known. More recently, the exocrine pancreas has been proposed to play a role in the destruction of beta cells, either by enhanced infiltration of immune cells in an animal model[31] or by the notion that T1D patients have a 30% reduction in pancreas weight[32]. Our observation may also hint to a malfunctioning of differentiation, or may reflect an exocrine/endocrine cell interaction, which opens the intriguing possibility that exocrine cells may interfere with beta cells. Thus the existence of mixed cells is readily identified by EDX. Although we only observed this in Islets of two diabetic rats (total of 32 cells), not in two controls, a conclusive statement whether or not this phenomenon relates to a (pre)diabetic state should await results from a follow-up study. This will include examining human pancreas[32], but is beyond the scope of this paper.

EDX has been used to discriminate healthy or diseased cells based on elemental expression, or to address whether certain elements are enriched[33]. Recently in an isolated cell model the potential to use elemental analysis and subcellular features was shown. Combination of EDX with EELS to explore additional elements with weak X-ray signals may thus further increase the elemental palette[8]. EDX can be implemented in an existing TEM or SEM, is compatible with epon-embedded material, straightforward, and compared to EELS analysis, does not need a priori selection of imaging windows. Another mode of color-EM, CLEM, is widely used to localize targets typically between 0.05–1 µm[2-5]. We foresee an integrated[34] approach, where EDX and CLEM not only complement, but also allow crossing scales from rapid fluorescence screening of large fields-of-view to lower-throughput high-resolution elemental painting. Here we focused on qualitative measurement of chemically fixed targets, using protocols we – and others - typically use for EM examination of human tissues for diagnosis. Implementing other existing sample preparation protocols refined for research, like high pressure freezing followed by freeze substitution, may help to use EDX imaging in quantitative analysis and also allow determination of certain ions at high resolution in biosamples. Broad application of EM-EDX will allow experimental analysis on large-scale tissues using endogenous elements, multiple stains, and multiple markers and thus brings nanometer-scale 'color-EM' as a tool to unravel molecular (mis)regulation in biomedicine.

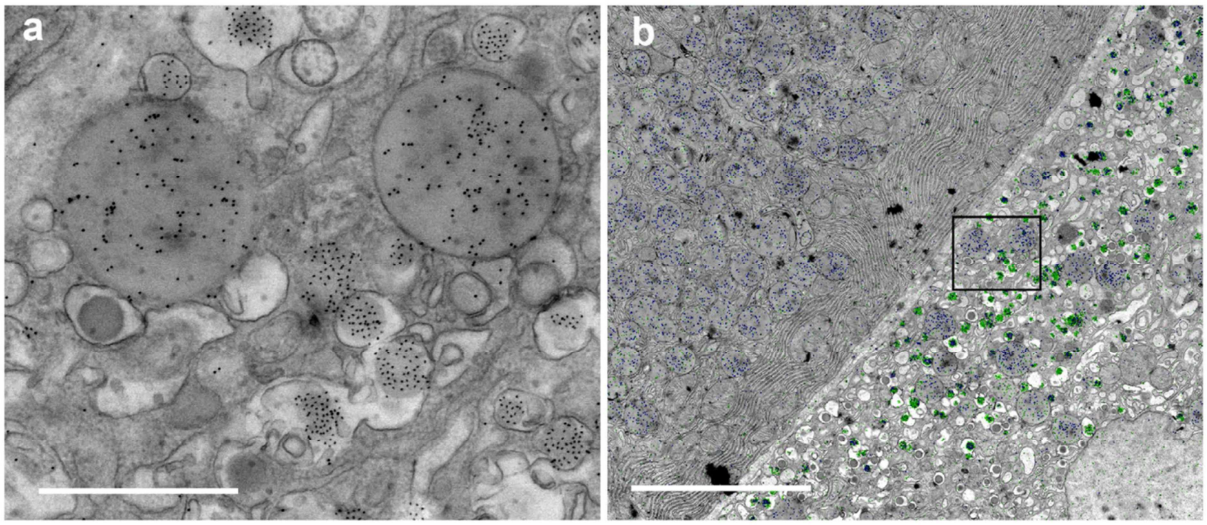

Figure 4 | Distinct granules in the same cell determined by immunolabeling. (**a**) Double immunolabeling of amylase (zymogen granules) with 10 nm immunogold and insulin with QD655 shows the appearance of distinct granules in the same cell based on morphology and electron density of the nanoparticles; immunogold is rounder and darker compared to the more rectangular and less electron dense QDs. Note that also unlabeled glucagon granules are present in the same cell. (**b**) Semi-automated nanoparticle annotation using the Fiji macro "golddigger" shows that distinct granules in the same cell occurs specifically in the islet (right) with the co-appearance of amylase (nanogold, blue) and insulin (QD655, green) labeling, and solely amylase (blue) labeling in the exocrine pancreas (left). Bars: 1 µm (**a**) and 5 µm (**b**).

Methods

Tissue and sample preparation

Embedded tissue blocs in EPON (Serva) were used as described before[15]. Alternatively, in the case of osmium-free EPON embedding, tissue was post-fixed with 1% tannic acid (BDH chemicals, UK) in 0.05 M maleate buffer pH 5.15 for 40 minutes at room temperature. Furthermore, for additional membrane fixation, tissue was incubated in 1% poly-phenylenediamine (PPD, Merck-Millipore, Germany) in 70% ethanol for 20 minutes as one of steps during dehydration via graded ethanol series. All methods were carried out in accordance with relevant guidelines and regulations and the university ethical board for animal studies from the University Medical Center Groningen (UMCG), The Netherlands approved all animal experiments reported in this study[15].Ultrathin sections (100 nm) were cut and collected on formvar single slot pyrolytic carbon grids (EMS, Hatfield, Pennsylvania).

Post-embedding immunolabeling

Grids were incubated with tissue facing down on droplets on parafilm at RT. First, samples were etched with 1% periodic acid (Merck, New Jersey) in milliQ water for 10 minutes to increase antigenicity, and rinsed in milliQ (4 × 5 min). This was followed by 30 minutes blocking with 1% bovine serum albumin (BSA; Sanquin, The Netherlands) in tris-buffered saline (TBS), pH 7.4. For insulin and amylase labeling an alternative blocking buffer (1% BSA-c (Aurion, Netherlands), 1% cold water fish skin gelatin (Sigma-Aldrich), 35 mM lysine (Fluka), and 1% normal goat serum (Jackson Immunoresearch, UK) in TBS, pH 7.4) was used for both blocking and antibody dilutions. Next, anti-insulin (guinea pig; 1:1000 in 1% BSA/TBS, Invitrogen) combined with either monocolonal 1H6

(1 µg/ml in 1% BSA/TBS)[19] or anti-amylase (rabbit; 1:50 in blocking buffer, Sigma-Aldrich), or anti-glucagon (rabbit; 1:50 in 1% BSA/TBS, Thermo Fisher) alone incubated for 2 hours, rinsed in TBS (4 × 5 min), followed by incubation for 1 hour with biotinylated secondary antibody (donkey-anti-guinea pig; 1:400 in 1% BSA/TBS, Jackson Immunoresearch) and subsequent rinsed in TBS (4 × 5 min). Finally, streptavidin-conjugated QD655 (1:1000 in 1% BSA/TBS; Life technologies, California) and secondary goat-anti-mouse antibody for 1H6 or goat-anti-rabbit for amylase conjugated to 10 nm gold (1:100 in 1% BSA/TBS; BBI solutions, United Kingdom), or goat-anti-rabbit-conjugated QD655 (1:1000 in 1% BSA/TBS; Life technologies) for glucagon were added for 1 hour and subsequently rinsed in TBS (4 × 5 min) and 0.1 M sodium cacodylate (2 × 5 min).

Microscopy

Large-scale STEM (nanotomy) - A large area scan using Scanning Transmission Detection (STEM) was made using a Zeiss supra55 SEM with Atlas as described before[35]. From this dataset smaller areas covering several cell types were selected for EDX analysis. Pre-exposure to stabilize samples was carried out at low magnification, depending on sample area. Typically, for the complete islets, 80 kV was used for 1 hour in a TEM. We note that after careful pre-exposure, we analyzed samples without signs of electron-beam induced damage or carbon deposition visible when comparing SEM images obtained before and after inspection, even after EDX maps acquisition times exceeding 1,5 hours, i.e., pixel exposure times >1 ms (excluding time for drift correction procedures), and after spectral point acquisition times of ~30 s.

EDX-analysis - The experiments were performed on a FEI Verios SEM equipped with an Oxford Instruments X-Max 80 mm^2 Solid State EDX detector. As stated by the supplier, when the detector is fully inserted, the distance between the sample and the EDX window is 35.81 mm for a working distance of 5 mm and a tilt angle of 35°. Hence, the collection angle is 0.061 sr. For practical reasons the position might not be identical, since we optimized the position for collecting the maximum number of X-ray counts at 4 mm working distance. It is difficult to measure the exact distance between the window and the sample. The EDX detector has supplier-stated energy resolution of ≤ 127 eV at the Mn Kα line, ≤64 eV at the F Kα line, and ≤56 eV at C Kα, all at count rates of 20,000 cps. Peak position and resolution on the Mn Kα do not change more than 1 eV between 1,000 and 100,000 cps as calibrated upon installation. Au nanoparticles with a mean diameter of 2.7 nm dispersed on a thin Carbon support grid were detected in EDX, indicating that for high-density probes spatial resolution in EDX can approach the SEM probe size.

The imaging of the region of interest is performed using the ICD (In Column Detector) available in the Verios SEM at a resolution of 3072 × 2207 pixels, with dwell time of 30 us per pixel. All the regions of interest were imaged at 15 kV acceleration voltage and 26 nA current, at 4 mm working distance, in Ultra High Resolution (UHR) mode. The EDX maps were all taken at 15 kV primary beam energy and 26 nA current, at a working distance of 4 mm, in UHR mode. The Oxford Instrument AZtec software was used for the acquisition of EDX maps and point & ID analysis. The resolution of the maps is 2048*1408 pixels, with dwell time 20 us per pixel. The process time, i.e. the time over which the voltage signal generated by the detector is averaged, was set to 4 (on a scale from 1 to 6) in order to optimize the acquisition rate and to reduce the voltage noise, and we selected 2048 channels, that gives an energy window of 10 eV per channel. In case of point & ID analysis, 4096 channels were used, with an energy of 5 eV per channel. Because of the long acquisition time for the EDX maps, sample and stage drift plays an important role. For that reason, the AZtech software drift correction option was activated, meaning that after a certain amount of time, determined by the software based on the drift speed, an EM image is acquired, which is compared to an original image taken at the start of the EDX map. The software automatically detects

particles or shapes in the image, from which it calculates the drift and compensates for it. The life-time, i.e. the effective time in which the spectra is acquired and integrated, and the collected number of frames for each field of view are listed in Supplementary Table S1.

Image processing

In Fiji (http://fiji.sc/), three selected elements were merged as RGB. All image processing has been applied to the whole image in a linear fashion using Fiji and/or Adobe Photoshop. To discriminate 10 nm immunogold and QD655 nanoparticles upon immunolabeling of amylase and insulin, semi-automated annotation using the Fiji macro "golddigger" was performed[36].

Acknowledgments

We thank Y. Weide, A. Wolters and N. Pirozzi for assistance with immunolabeling and P. Lansdorp for 1H6. We acknowledge financial support from the European Union (Agreement No. 318804 – SNM; Single Nanometer Manufacturing for Beyond CMOS devices) and the Netherlands Organization for Scientific Research (ZonMW91111006; "Microscopy Valley" STW12714; STW12718; NWO175-010-2009-023).

References

1. Patwardhan, A. *et al*. A 3D cellular context for the macromolecular world. *Nat. Struct. Mol. Biol.* **21**, 841-845 (2014).

2. Nelson, A. & Hess, S. Localization microscopy: mapping cellular dynamics with single molecules. *J. Microsc.* **254**, 1-8 (2014).

3. Hell, S. W. Nanoscopy with Focused Light (Nobel Lecture). *Angew. Chem. Int. Ed Engl.* **54**, 8054-8066 (2015).

4. Schermelleh, L., Heintzmann, R. & Leonhardt, H. A guide to super-resolution fluorescence microscopy. *J. Cell Biol.* **190**, 165-175 (2010).

5. Giepmans, B. N., Adams, S. R., Ellisman, M. H. & Tsien, R. Y. The fluorescent toolbox for assessing protein location and function. *Science* **312**, 217-24 (2006).

6. de Boer, P., Hoogenboom, J. P. & Giepmans, B. N. Correlated light and electron microscopy: ultrastructure lights up! *Nat. Methods* **12**, 503-513 (2015).

7. Loussert Fonta, C. & Humbel, B. M. Correlative microscopy. *Arch. Biochem. Biophys.* **581**, 98-110 (2015).

8. Feng, J., Somlyo, A. V. & Somlyo, A. P. A system for acquiring simultaneous electron energy-loss and X-ray spectrum-images. *J. Microsc.* **215**, 92-99 (2004).

9. Shuman, H., Somlyo, A. V., Safer, D., Frey, T. & Somlyo, A. P. Applications of energy filtered imaging in biology. *Scan. Electron Microsc.* **(Pt 2)**, 737-743 (1983).

10. Somlyo, A. V., Shuman, H. & Somlyo, A. P. Composition of sarcoplasmic reticulum in situ by electron probe X-ray microanalysis. *Nature* **268**, 556-558 (1977).

11. Vrensen, G. F. *et al*. Tryptophan deficiency arrests chromatin breakdown in secondary lens fibers of rats. *Exp. Eye Res.* **78**, 661-672 (2004).

12. Mauritz, J. M. *et al*. X-ray microanalysis investigation of the changes in Na, K, and hemoglobin concentration in plasmodium falciparum-infected red blood cells. *Biophys. J.* **100**, 1438-1445 (2011).

13. Aronova, M. & Leapman, R. Development of electron energy-loss spectroscopy in the biological sciences. *MRS Bull* **37**, 53-62 (2012).

14. Adams, S. R. *et al*. Multicolor Electron Microscopy for Simultaneous Visualization of Multiple Molecular Species. *Cell. Chem. Biol.* **23**, 1417-1427 (2016).

15. Ravelli, R. B. *et al*. Destruction of tissue, cells and organelles in type 1 diabetic rats presented at macromolecular resolution. *Sci. Rep.* **3**, 1804 (2013).

16. Sokol, E. *et al*. Large-Scale Electron Microscopy Maps of Patient Skin and Mucosa Provide Insight into Pathogenesis of Blistering Diseases. *J. Invest. Dermatol.* **135**, 1763-1770 (2015).

17. Sousa, A. A. & Leapman, R. D. Development and application of STEM for the biological sciences. *Ultramicroscopy* **123**, 38-49 (2012).

18. Kuipers, J., de Boer, P. & Giepmans, B. N. Scanning EM of non-heavy metal stained biosamples: Large-field of view, high contrast and highly efficient immunolabeling. *Exp. Cell Res.* **337**, 202-207 (2015).

19. Hoffmann, R. F. *et al*. Guanine quadruplex structures localize to heterochromatin. *Nucleic Acids Res.* **44**, 152-163 (2016).

20. Emsley, J. in *The elements* vii, 292 pages : illustrations ; 29 cm (Clarendon Press ;; Oxford University Press, Oxford :; New York :, 1998).

21. Nisman, R., Dellaire, G., Ren, Y., Li, R. & Bazett-Jones, D. P. Application of quantum dots as probes for correlative fluorescence, conventional, and energy-filtered transmission electron microscopy. *J. Histochem. Cytochem.* **52**, 13-18 (2004).

22. Giepmans, B. N., Deerinck, T. J., Smarr, B. L., Jones, Y. Z. & Ellisman, M. H. Correlated light and electron microscopic imaging of multiple endogenous proteins using Quantum dots. *Nat Methods* **2**, 743-9 (2005).

23. Wu, J. *et al*. Imaging and elemental mapping of biological specimens with a dual-EDS dedicated scanning transmission electron microscope. *Ultramicroscopy* **128**, 24-31 (2013).

24. Pivovarova, N. B. & Andrews, S. B. Measurement of Total Calcium in Neurons by Electron Probe X-ray Microanalysis. *JoVE (Journal of Visualized Experiments)*, e50807-e50807 (2013).

25. Falke, M. *et al*. Element Analysis by EDX for Life Science: Light Elements and Bio-Mineralization. *Microscopy and Microanalysis* **19**, 222-223 (2013).

26. Fernandez-Segura, E. & Warley, A. Electron probe X-ray microanalysis for the study of cell physiology. *Methods Cell Biol.* **88**, 19-43 (2008).

27. Michalak, I., Marycz, K., Basińska, K. & Chojnacka, K. Using SEM-EDX and ICP-OES to Investigate the Elemental Composition of Green Macroalga Vaucheria sessilis. *The Scientific World Journal* **2014** (2014).

28. Zhou, Q., Brown, J., Kanarek, A., Rajagopal, J. & Melton, D. A. In vivo reprogramming of adult pancreatic exocrine cells to beta-cells. *Nature* **455**, 627-632 (2008).

29. Spijker, H. S. *et al*. Conversion of mature human beta-cells into glucagon-producing alpha-cells. *Diabetes* **62**, 2471-2480 (2013).

30. Bertelli, E. & Bendayan, M. Intermediate endocrine-acinar pancreatic cells in duct ligation conditions. *Am. J. Physiol.* **273**, C1641-9 (1997).

31. Rodriguez-Calvo, T., Ekwall, O., Amirian, N., Zapardiel-Gonzalo, J. & von Herrath, M. G. Increased immune cell infiltration of the exocrine pancreas: a possible contribution to the pathogenesis of type 1 diabetes. *Diabetes* **63**, 3880-3890 (2014).

32. Campbell-Thompson, M., Rodriguez-Calvo, T. & Battaglia, M. Abnormalities of the Exocrine Pancreas in Type 1 Diabetes. *Curr. Diab Rep.* **15**, 79-015-0653-y (2015).

33. Sporn, T. A., Roggli, V. L., Shelburne, J. D. & Ingram, P. in *Biomedical Applications of Microprobe Analysis* (eds Ingram, P., Shelburne, J. D. & Roggli,V.L.,LeFurgey,A.) 87-122 (Academic Press, 1999).

34. Zonnevylle, A. C. *et al*. Integration of a high-NA light microscope in a scanning electron microscope. *J. Microsc.* **252**, 58-70 (2013).

35. Kuipers, J., de Boer, P. & Giepmans, B. N. Scanning EM of non-heavy metal stained biosamples: Large-field of view, high contrast and highly efficient immunolabeling. *Exp. Cell Res.* **337**, 202-207 (2015).

36. Sjollema, K. A. & Giepmans, B. N. G. Automated Annotating Label in Nanotomy - Using ImageJ to quantify nanoparticles in large EM datasets. *Imaging and microscopy* **4**, 45-46 (2016).

Supplementary information

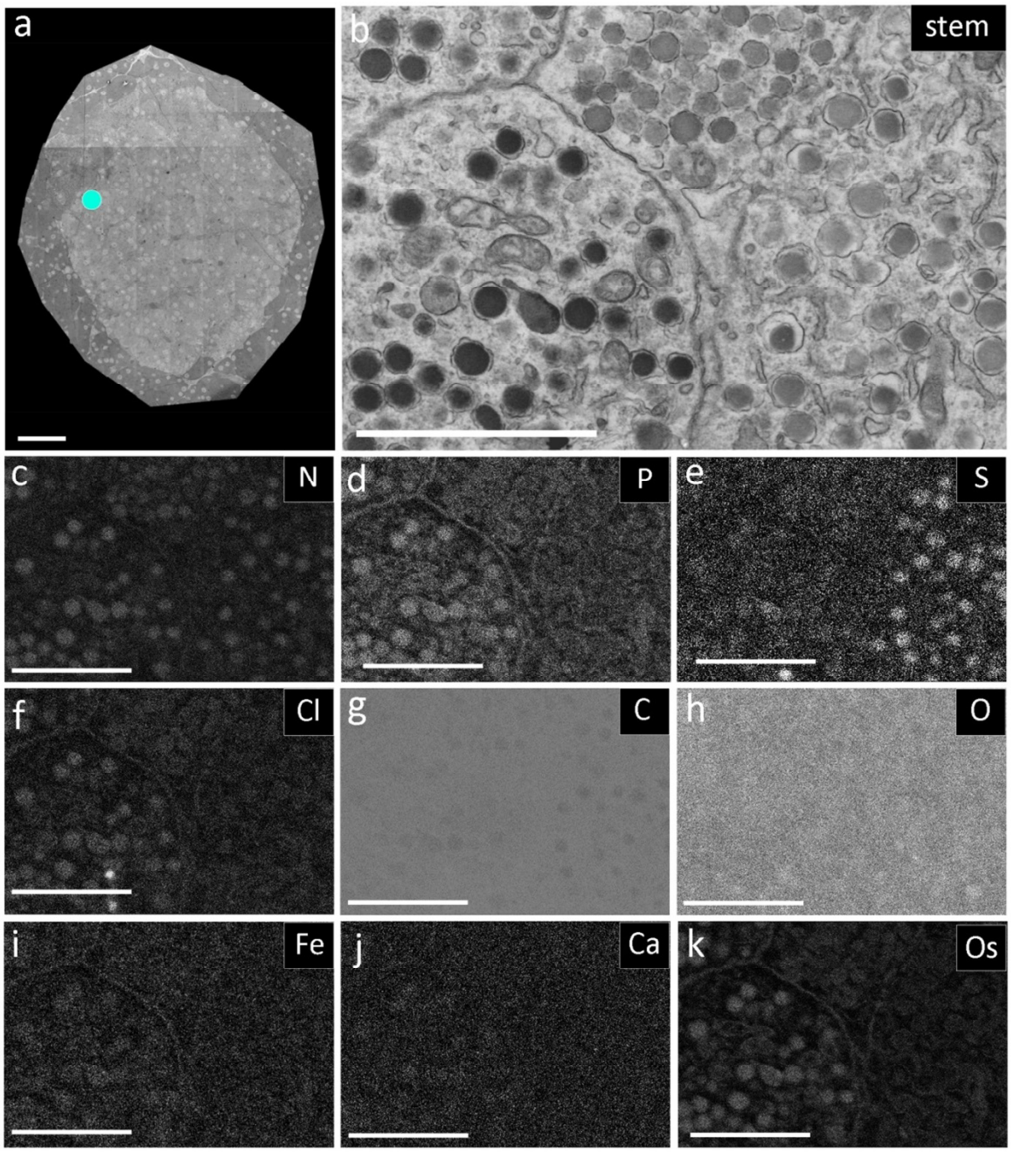

Figure S1 | Additional element-specific images as indicated. See Fig. 1 for details.

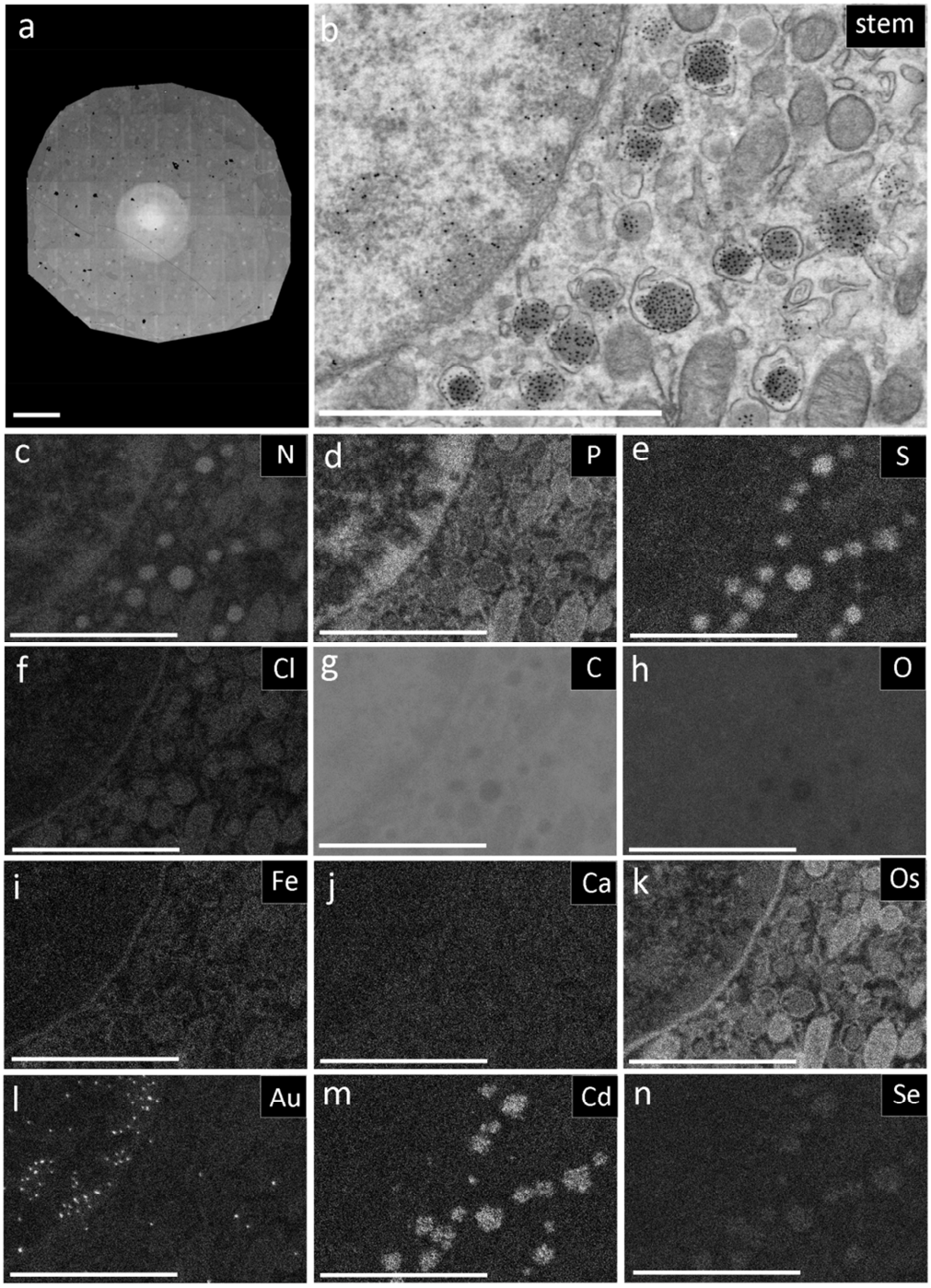

Figure S2 | Additional element-specific images as indicated. See Fig. 2 for details.

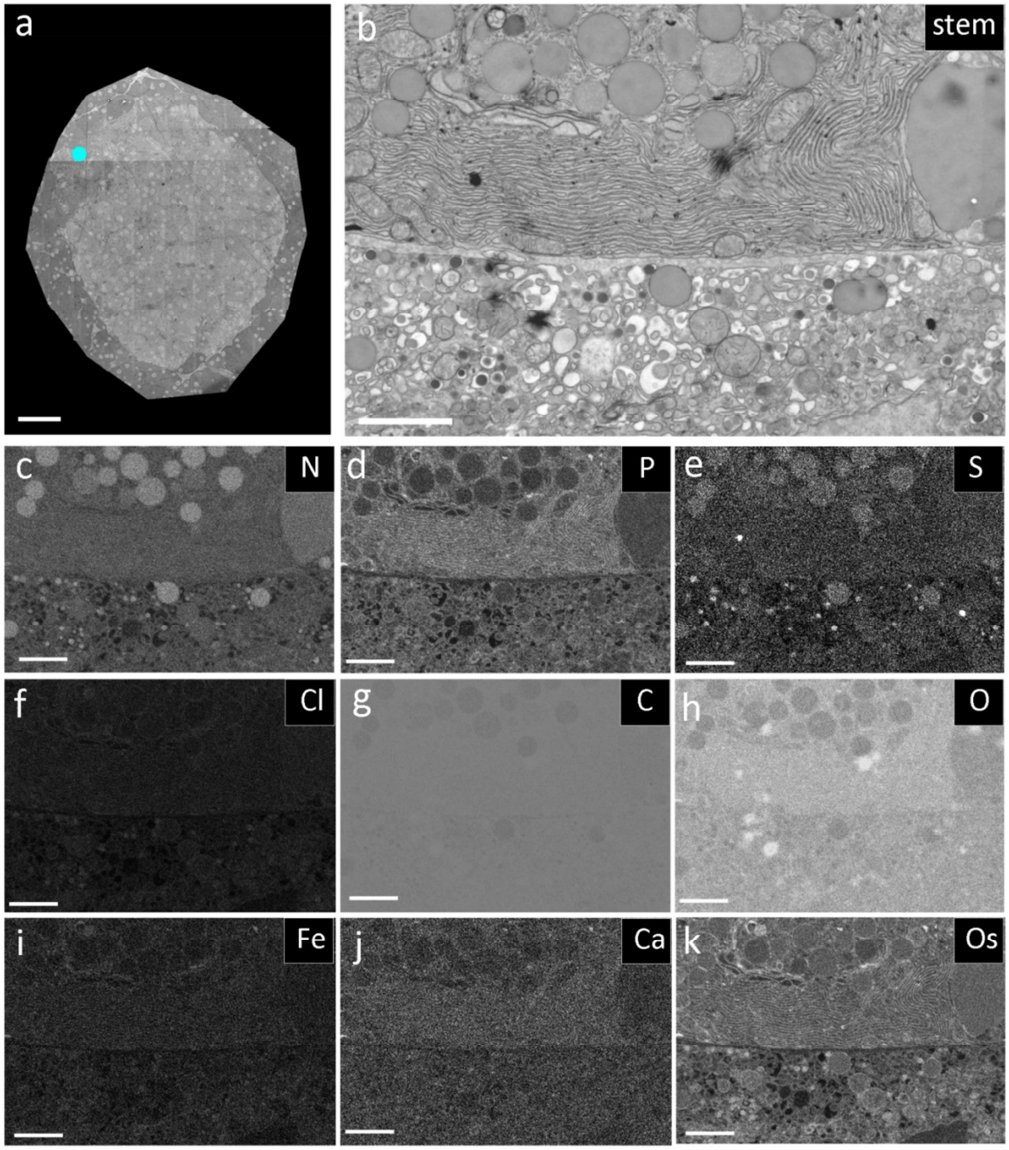

Figure S3 | Additional element-specific images as indicated. See Fig. 3 for details.

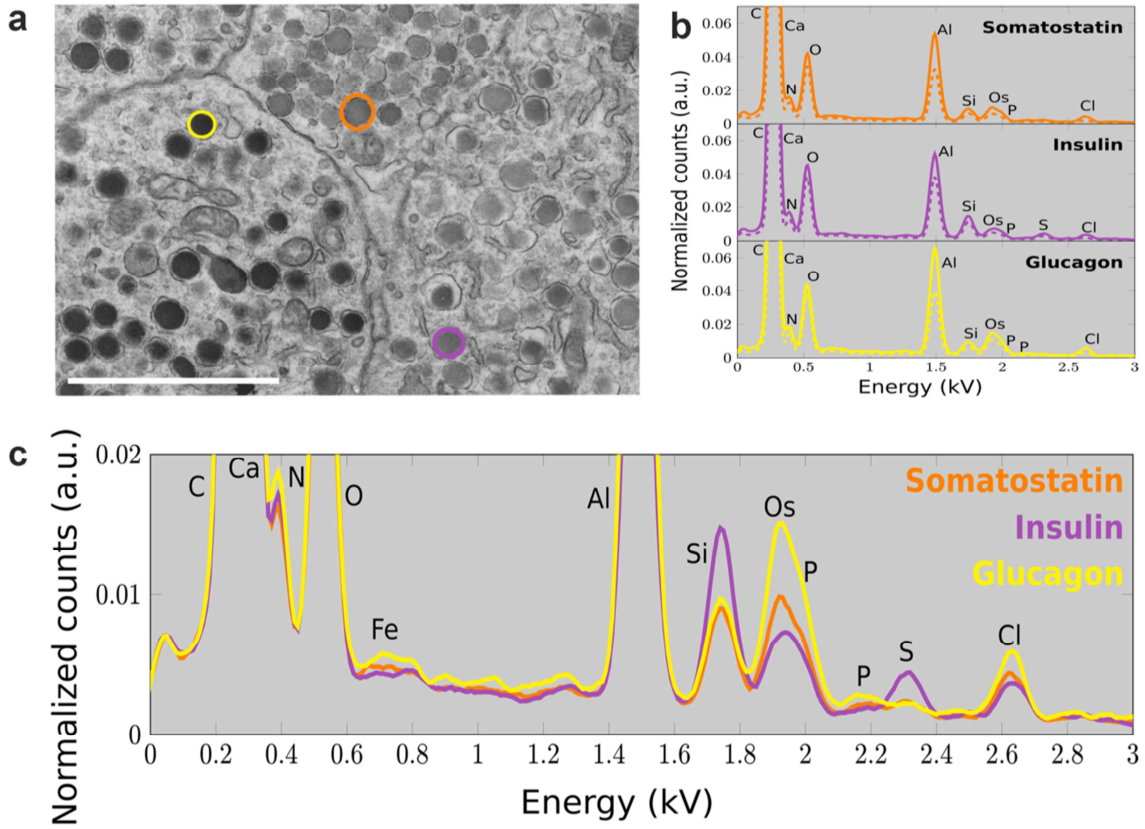

Figure S4 | EDX spectral differences between different hormone-containing granules. (**a**) Same area as in manuscript Figure 1 with circles indicating the granules for which EDX spectra are shown in (b). (**b**) EDX spectra for the respective granules in (a). Drawn lines denote spectra obtained by averaging the data collected in the spatial maps over the indicated granules. Dashed lines indicate spectra obtained by 30 second integration on a single spot within the granule. All spectra are normalized to the C peak and smoothed using a standard Matlab routine. All spectral features in the spectra obtained from the EDX maps are qualitatively reproduced in the spot integration curves, confirming the validity of the acquisition time for the EDX maps. The pronounced Al signal comes from sampleholder, probably from back-scattered electrons generated in the sample that hit the sample holder. (**c**) Comparison of EDX spectra obtained for the three different granules, revealing the increased level of S in insulin granules, P in glucagon granules, and relative absence of both for somatostatin. Note also the pronounced differences in Os staining level corresponding to the granule interpretation in standard grey-scale EM. Scalebar in (a) 2□m. Experimental settings: 15kV beam energy at 26nA, EDX: process time 4, 4096 channels, 5eV per channel.

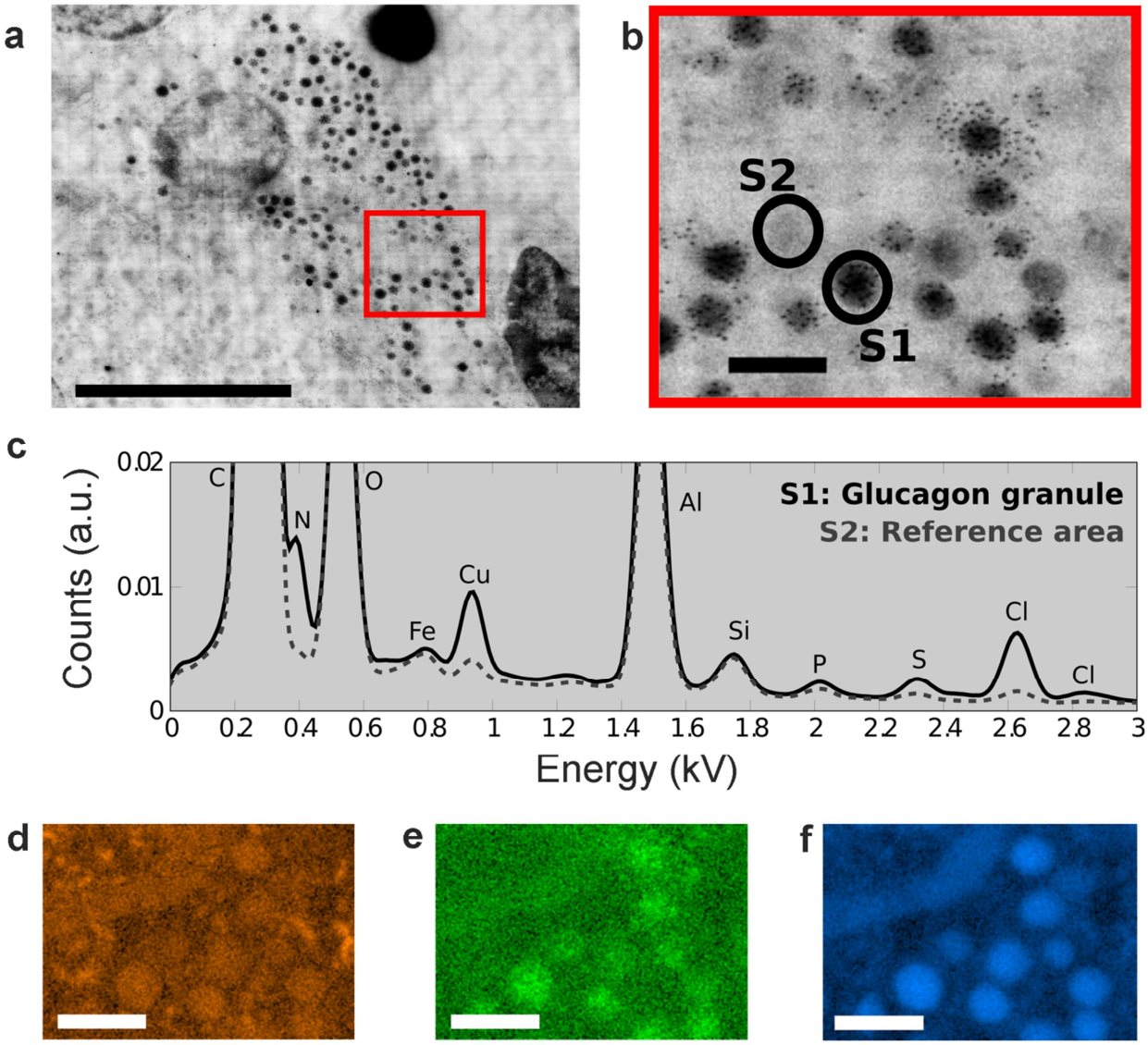

Figure S5 | EDX data on glucagon-producing alpha cell using an Osmium-free sample preparation. Quantum dots are labelling glucagon to allow identification of the glucagon granules (**a**) SEM image of an alpha cell. (**b**) Magnified image of the boxed area in (a) with clear visibility of QDs on the granules. (**c**) EDX spectra obtained by integrating the spectral maps over the glucagon granule and the reference area indicated in (b). (**d, e, f**) EDX maps of the area in (b) depicting the signal for the indicated spectral lines for (d) P, (e) S, and (f) N. Note how the (speckled) S signal follows the distribution of the ZnS-shelled quantum dots, visible especially in the upper right corner. The glucagon granules are clearly discerned in the P map. Sample preparation was similar to that for the data in the manuscript, except for the omission of Osmium and a section thickness of 300 nm. The spectra in (c) have been normalized to the C peak and smoothed using Matlab. Scale bars are 5 µm in (a) and 500 nm in the other panels.

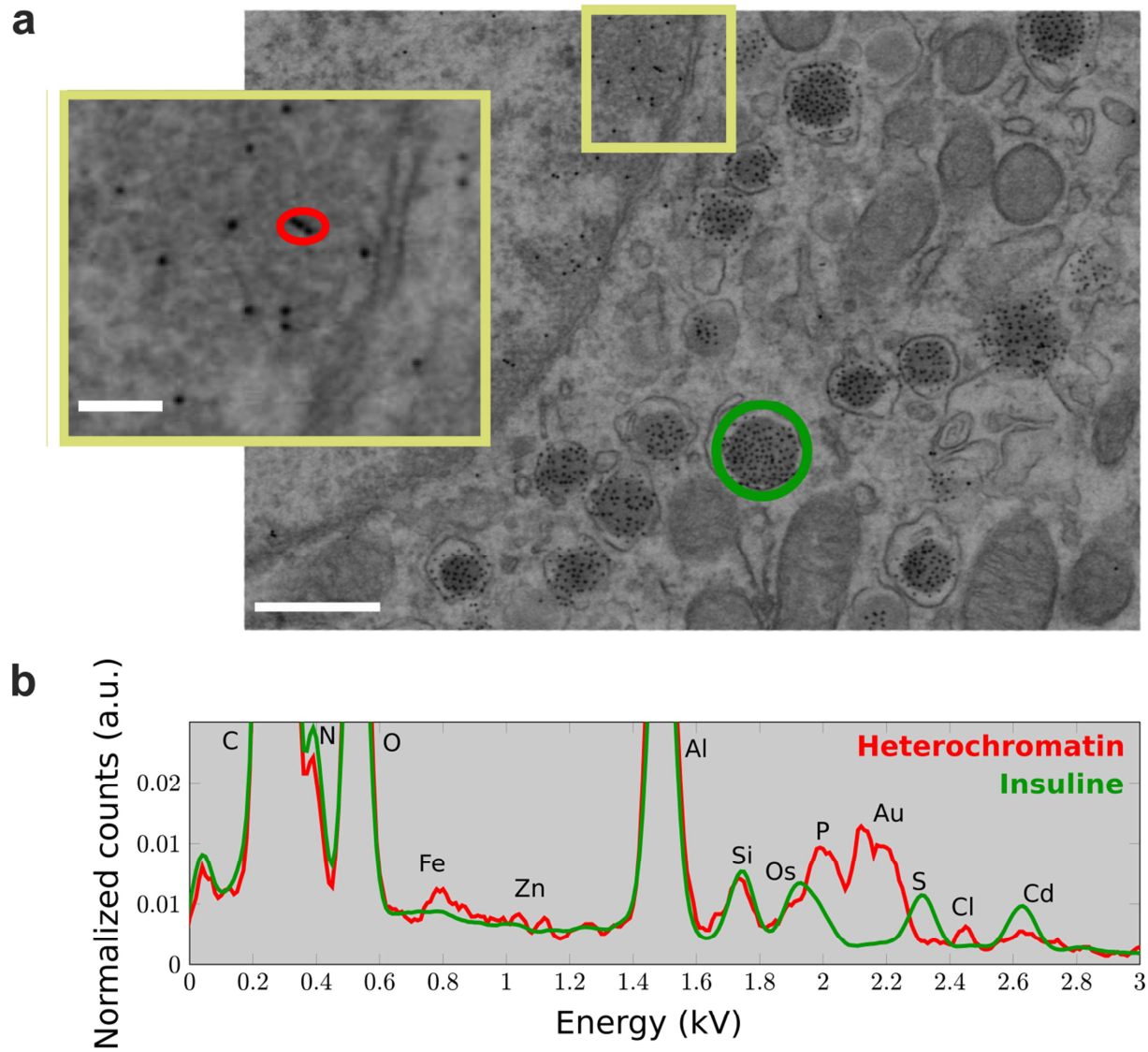

Figure S6 | EDX spectra comparison for quantum dot and gold nanoparticle labelled sample. (Manuscript Fig. 2). (**a**) Same area as in Fig 2b with circles indicating regions over which EDX spectra were averaged for (b). Inset is shown for the area indicated with yellow rectangle. (**b**) EDX spectra averaged over the indicated areas. Au signal (targeted to 1H6) is clearly visible in conjunction with a strong P peak from heterochromatin. In the green area, Cd is clearly present originating from the quantum dots core, together with weaker Zn from the quantum dot shell. Note that the S peak appears slightly more pronounced compared to, e.g., Os and Cl than in Fig. 1b, presumably due to the additional presence of the ZnS quantum dots shell. Experimental settings as stated in the manuscript, spectra normalized to the C peak and smoothed using Matlab. Scale bar 500nm, and 100nm in the inset.

Table S1 | EDX acquisition characteristics per FOV

Data	Lifetime (10^3 s)	Frames (n)
Fig.1	1.5	25
Fig.2	3.7	64
Fig.3	5.8	100
Fig.4	5.8	100

Chapter 5

Advanced microscopy implementation in type 1 diabetes research

Chapter 5a

Large-scale digital electron microscopy resource for human type 1 diabetes

Pascal de Boer[1#], Nicole M. Pirozzi[1#], Anouk H.G. Wolters[1], Jeroen Kuipers[1], Irina Kusmartseva[2], Martha Campbell-Thompson[2] and Ben N.G. Giepmans[1]

[1]Department of Cell Biology, University Medical Center Groningen, University of Groningen, Groningen, The Netherlands; [2]Department of Pathology, Immunology and Laboratory Medicine, University of Florida, Gainesville, FL USA.

[#]Denotes equal contribution

Manuscript submitted

Abstract

The cause of type 1 diabetes remains unknown. Here, we applied a recently developed microscopic imaging approach on a unique biobank of human islets of Langerhans to study ultrastructural morphology of islets in type 1 diabetes donors using electron microscopy (EM). To make human islet EM data of greatest value to multiple researchers, we created an online repository composed of large-scale EM images (termed 'nanotomy') that allows analysis of islets and surrounding exocrine tissues at macromolecule resolution. Donors include those without diabetes, type 1 and type 2 diabetes and donors with autoantibodies associated with type 1 diabetes. Using a web-based infrastructure, the equivalent of ~1 million traditional EM images is now available via www.nanotomy.org/nPOD. A first analysis based on morphology and subsequent 'ColorEM' reveals intermediate cells found in two donors with type 1 diabetes. Moreover, the specificity of leukocytes found in islet inflammation is observed as recently published by other methods. Thus, the EM islet nanotomy database reveals features from the macromolecular to the tissue level presented in an unbiased way. By providing open access to the repository, diabetes investigators worldwide can address countless research questions through the database.

Introduction

The underlying mechanism(s) initiating destruction of beta cells resulting in type 1 diabetes are still poorly understood (1), precluding curing the disease. Injectable insulin is the replacement treatment for type 1 diabetes since 1921 (2-4). The JDRF Network for Pancreatic Organ Donors with Diabetes (nPOD) provides high quality biospecimens to understand mechanisms leading to type 1 diabetes (5, 6). nPOD encourages investigators to work across multiple disciplines and implement new tools to study type 1 diabetes, as well as open-access publication of raw data that enables reuse and analysis by scientists worldwide to obtain new information from complex datasets (7, 8). Pancreases and other biospecimens are obtained from donors with type 1 diabetes as well as donors without diabetes (ND), type 2 diabetes, and type 1 diabetes-associated autoantibody-positive (AAb+) donors. AAb+ donors have one or more autoantibodies but no clinical diabetes symptoms. People with multiple AAb+ are at high risk to develop type 1 diabetes (9).

Here, we present a nanoscale data repository from nPOD organ donors of islets of Langerhans. Through large-scale electron microscopy (EM), termed 'nanotomy' for nano-anatomy (10-12), an extensive database of unbiased islet ultrastructure was established. Islets and surrounding exocrine tissue were imaged in fields of view up to 0.5 mm in diameter at 2.5 nm pixel size. From a web-based viewer, the entire tissue section can be analyzed from low to high resolution, ranging from structures as large as islets (sub-mm diameter) to single intra-islet cells and their organelles (µm- to nm-scale)(10). The parameters can be analyzed across an intact islet in near-molecular detail from a single dataset. Several relevant features were analyzed for this report including insulin granules, prevalence of mast cells and neutrophils near islets, and the presence of a rare type of intermediate cell seen only in donors with type 1 diabetes that contained both endocrine as well as zymogen secretory granules. Different granules were identified using a recently reported 'ColorEM' approach allowing label-free identification of elements in granules (13). The reported data are only a subset of features contained within the complex dataset. Data are open access available for reuse to analyze all ultrastructural information of specific nPOD donor samples to permit additional insights as well as in conjunction with findings using different techniques. This repository contains the most elaborate pancreatic EM data sets that is push-button available, bypassing laborious and expensive image-acquisition by individuals. The shared data is thus expected to greatly benefit the diabetes research community and additionally may boost open access image sharing of biobank material in other fields.

Research design and methods

Donors

Thirty-one EM islet datasets were created from 23 donors (ND (8), AAb+ (4), type 1 diabetes (8), type 2 diabetes (3)) and their nPOD CaseID with demographic details are listed in Table 1. Additional donor details can be obtained through the JDRF nPOD online pathology(14). Tissues were recovered following informed research consent from next of kin in the United States and shipped to the nPOD program at the University of Florida for processing as previously described (5, 6, 15). All experiments were conducted under the approval of the University of Florida Institutional Review Board and the current study fulfills all requirements for tests as approved by the medical ethical review board of the University Medical Center Groningen.

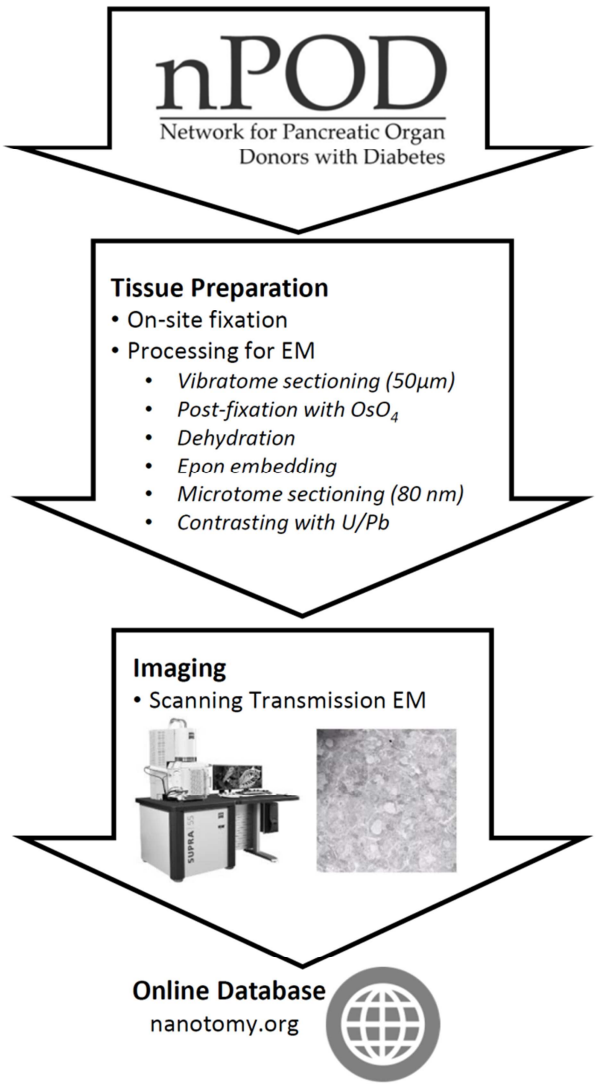

Figure 1 | nPOD nanotomy data generation workflow. Fixed pancreatic samples are received from nPOD. The tissue undergoes processing for scanning transmission electron microscopy (EM) as indicated followed by acquisition at 2.5 nm pixel size. The final stitched image is converted to html and uploaded to nanotomy.org.

Pancreas sample electron microscopy processing

Pancreas samples from the head, body, or tail regions (Table 1, S1) were fixed in cold, freshly prepared 2% paraformaldehyde-1% glutaraldehyde for 48 hours followed by transfer to phosphate-buffered saline for storage at 4°C before shipment to the EM laboratory in the Netherlands (15). Tissue vibratome sections (~50 µm; Microm HM 650V) were post-fixed in osmium tetroxide/ potassium ferrocyanide, followed by dehydration and flat-embedding as previously reported (10).

Next, regions with islets were selected from toluidine stained 1 µm sections using light microscopy. Subsequent ultrathin (80 nm) sections were cut (UC7 ultramicrotome, Leica Microsystems, Vienna, Austria) and placed on formvar coated copper grids (Electron Microscopy Sciences, Hatfield, Pennsylvania). Finally, sections were contrasted with uranyl acetate followed by Reynold's lead citrate (16) as previously described (10, 11).

EM acquisition and image processing (nanotomy)

Data were acquired on a Supra 55 scanning EM (SEM; Zeiss, Oberkochen, Germany) using a scanning transmission EM (STEM) detector at 28kV with 2.5 nm pixel size (2 nm pixel size for datasets 6098a and b, 6126a, 6197, 6087a, 6113, and 6198) using an external scan generator ATLAS 5 (Fibics, Ottawa, Canada) as previously described (11, 12). After tile stitching, data were exported as an html file and uploaded to the online image database (www.nanotomy.org) (Fig. 1).

Energy Dispersive X-Ray Analysis (EDX; 'ColorEM')

Energy dispersive x-ray analysis (EDX) imaging for element discrimination was performed essentially the same as recently described (13). Briefly, regions of interest were determined using the nanotomy maps. Next, subsequent sections of 100 nm were cut and placed on a formvar-coated single slot pyrolytic carbon grid (Ted Pella, INC., California, USA) followed by uranyl acetate staining. The selected regions of interest were imaged using an Oxford Instruments X-Max^N 150 mm^2 Silicon Drift Detector and AZtecEnergy software (Abingdon, UK) mounted on the Zeiss Supra SEM. EDX images were generated (sum of 30-40 frames) with 50 µs dwell time at 15kV acceleration voltage and 8.4 nA beam current. Image analysis and processing was done in Adobe Photoshop and included a Gaussian blur of 1.5 pixel radius to the raw elemental maps followed by adjustments of white points for each color channel in a level adjustment layer, followed by +25 brightness and +50 contrast adjustment layer. Raw data are shown in Figs. S1, 2.

Primary analysis of data

Complete nanotomy datasets were manually screened field by field for the presence of different cell types based on standard ultrastructural features (Table 1). The presence of each cell type and any abnormal cells, e.g. intermediate cells based on exocrine and endocrine vesicles as well as subtypes of mast cells which can be distinguished based on the morphology of granules: Tryptase mast cell granules have scrolls, whereas chymase-tryptase mast cells have more homogeneous granules (17).

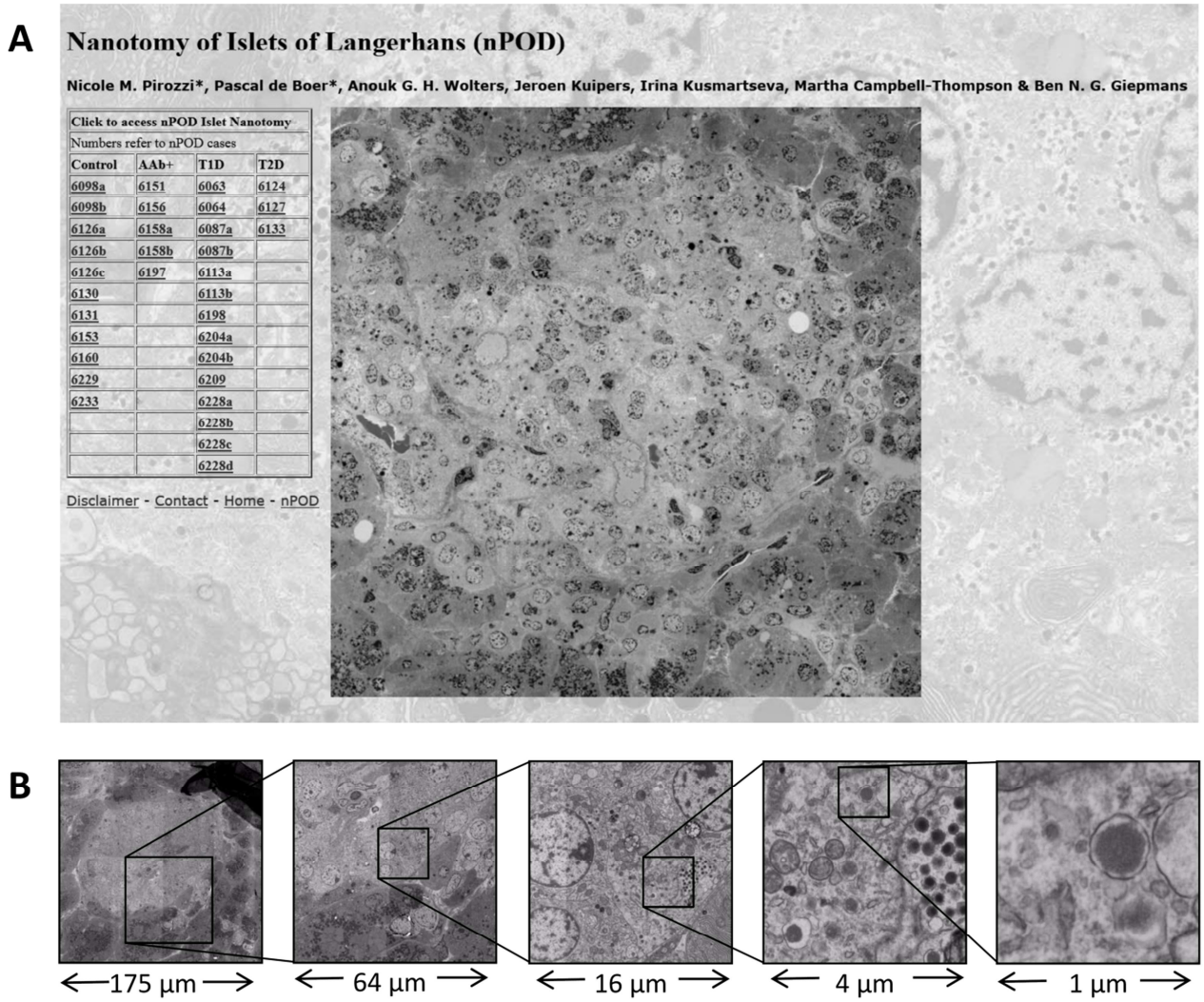

Figure 2 | nPOD nanotomy repository allows zooming into islets up to macromolecular complexes. (A) nanotomy.org/nPOD web interface allows selection of islets based on nPOD caseID and subsequent analysis of the sample. (B) While analysis should be performed digital, one example is given. From left to right: Analyzing whole cross-sections of islets, part of an islet, several cells with subcellular details like the nucleus; organelles like mitochondria and secretory vesicles. Zooming and panning allows detailed analysis on small areas on a large variety of read outs while maintaining full context.

Results

nPOD nanotomy: Equivalent of ~1 million of regular EM images of islets of nPOD donors

The unique approach of the nPOD program (15) allowed systematic analysis of islets in pancreata of type 1 donors as well as controls and other donors (Fig. 1). The repository is organized by nPOD CaseID to permit linking other studies from the same donor (18) to these ultrastructural images and now contains 31 datasets of 23 donors (Fig. 2*A*) . We set out to optimize a protocol for islet sample preparations and determined the ultrastructural quality of immersion fixed human donor pancreases. Strikingly, sample quality was deemed very high regardless of the duration of storage. Only 1 out of 24 donor samples received did not have useful morphology. As expected, islets of Langerhans were smaller and harder to find in type 1 diabetes donors. The nanotomy data acquired were uploaded to the nPOD nanotomy website (Fig. 2*A*). Images of complete cross sections of islets of Langerhans at macromolecular scale allow morphological analysis of complete islets, cells, organelles, and macromolecules (Fig. 2*B*) by simply zooming in at higher resolution at any region or feature of interest.

Label-free identification of multiple parameters in type 1 diabetes donors

Expert analysis allowed discrimination of different cell types present in the pancreas based on the morphology and grey levels of the secretory granules (Fig. 3). Islets were distinguishable by clustering of cells with lighter cytoplasm, smaller secretory granules, and less abundant ER than the acinar cells of the exocrine tissue. Islets from control donors contain the expected cell types and their various endocrine hormones (alpha, beta, delta, and pancreatic polypeptide (PP) cells) that have been characterized previously using traditional transmission EM analysis based on their distinct secretory vesicles (19-21). Glucagon-containing alpha cell granules (Fig. 3) are the most electron-dense, typically 200-250 nm in diameter, and often contain a thin halo between the membrane and the electron dense core. Insulin-containing beta cell granules (Fig. 3) are less electron-dense, typically 250-300 nm in diameter, and mature insulin granules have a prominent halo between the membrane and a crystalline core. Granules of delta and PP cells (Fig. 3) are of variable electron-density and are differentiated mainly by size with granules 200-350 nm and 120-160 nm in diameter, respectively(20). In the exocrine pancreas, acinar cells are characterized by abundant rough ER and larger zymogen-containing secretory granules (0.5-1.5 µm diameter; Fig. 3)(22). Mast cells are also frequently observed, with amorphous secretory granules (Fig. 3). For the mast cells which are of the tryptase+ subset, the granules also contain cylindrical clusters (Fig. 3)(23).

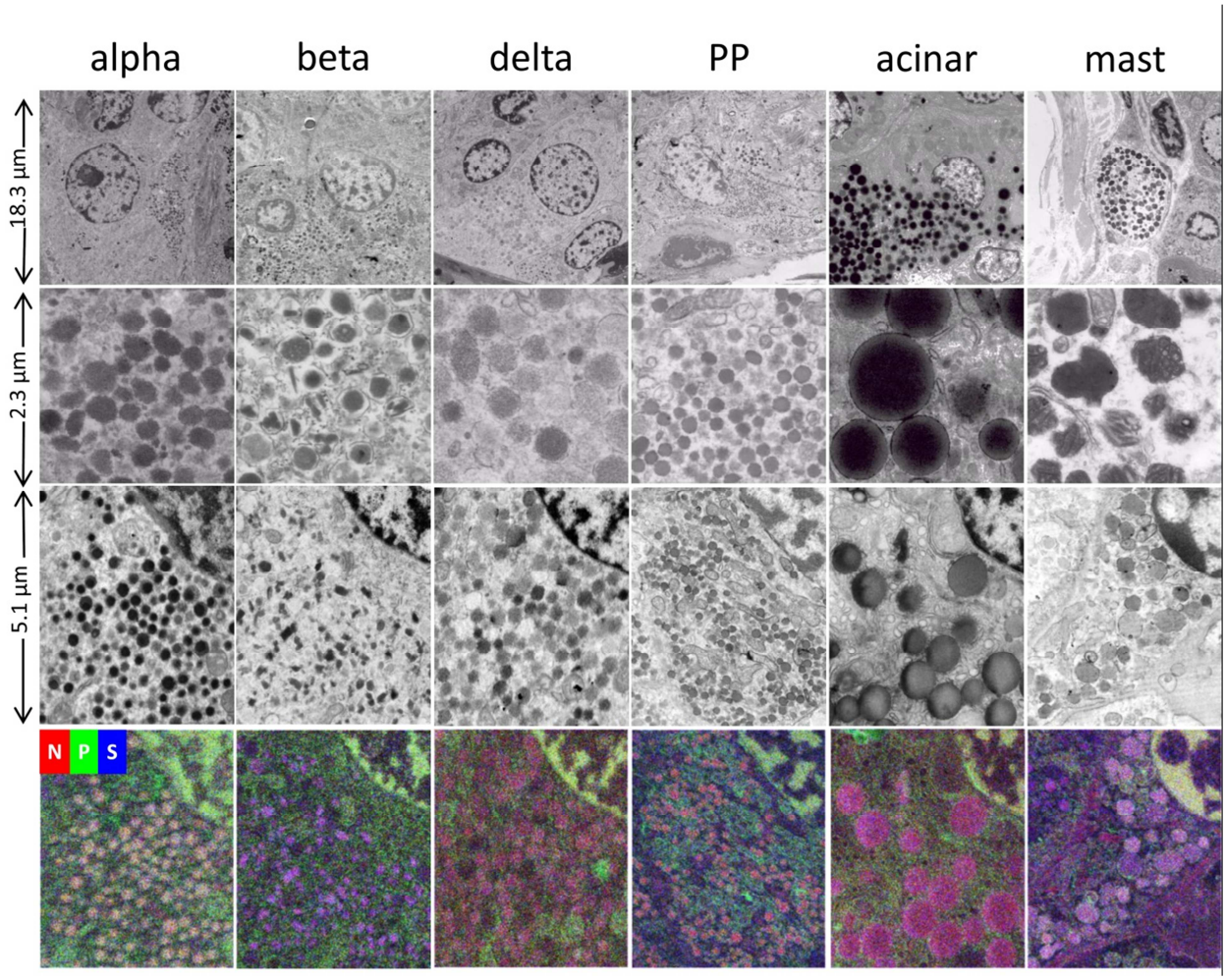

Figure 3 | Label-free identification of cells and organelles in nPOD nanotomy and ColorEM. Different pancreatic cell types are discriminated based on secretory granule appearance. Glucagon granules of the alpha cells often contain an electron dense core with a thin halo between the core and membrane. Insulin granules of the beta cells also contain a halo between core and membrane with a crystalline core in mature granules. Somatostatin granules of the delta cells and pancreatic polypeptide granules of the PP cells both contain relative small granules with variable grey values. Zymogen granules of exocrine acinar cells are relatively large (0.5-1 µm) and electron dense. Lastly, mast cells could be observed containing granules with cylindrical structures. Cells can also be distinguished by ColorEM via EDX as seen in the corresponding image to each cell type. EDX maps of phosphorus, nitrogen, and sulfur in green, red, and blue, respectively, are overlaid to show the relative difference in elemental composition of secretory granules of alpha, beta, delta, PP, acinar, and mast cells. Secretory granules of each cell type have high nitrogen (red) and cell types can be further distinguished based on enrichment of additional elements such as phosphorus (green) in alpha cell granules, displayed in orange, and sulfur (blue) in beta cell and mast cell granules, displayed in purple. Alpha, beta, delta, PP, acinar, and mast cell images are taken from nanotomy datasets from donors 6064, 6130, 6126, 6130, 6126, and 6087, respectively. ColorEM of donors 6126 (alpha, beta, delta, and acinar) and 6130 (PP and mast). Raw EDX data are shown in Fig. S1.

Although identification of endocrine cell types is feasible using these established granule morphological characteristics, elemental composition provides objective determination of cell types (13, 24). Elemental maps of phosphorus, nitrogen, and sulfur are overlaid to determine the variation of granule content within each endocrine cell type (Fig. 3, see Fig. S1 for raw element maps). The nuclei shown in the upper right corner of each image contain high amounts of nitrogen and phosphorus in the condensed heterochromatin, appearing yellow with the green and red overlay. All secretory granules have a high nitrogen content as expected from the high concentration of polypeptides. Additionally, granules of human beta and mast cells contain a prominent sulfur signal, and granules of alpha cells are enriched with phosphorus, in line with our earlier observations in rat islets(13). Thus, addition of a detector to the EM that allows elemental characterization by X-ray analysis allows differentiation of cell types and organelles by elemental content.

Mast cell and neutrophil variation between donor groups

Immune cells, including neutrophils and mast cells, are observed in the different datasets. Neutrophils are almost exclusively present in type 1 diabetes cases (Table 1), except for one case in each of the other groups, with the highest numbers in two type 1 diabetes patients who had acute pancreatitis (6064 and 6204; Supplementary Table 1). Neutrophils are found mainly in the exocrine tissue and not in the islets though some were found peri-islet (Fig. 4*A, B*). Only one islet dataset from a type 2 diabetes donor (6133) exhibited a neutrophil inside the islet. While mast cells were observed in each of the four subgroups (Table 1), in type 1 diabetes they were exclusively seen in all donors with disease durations of 3 or more years (Fig. 4*C-F)*.

Based on granular content, mast cells are subdivided into tryptase cells and chymase-tryptase cells. Tryptase mast cell granule content is characterized by well-defined scrolls (Fig. 4*C,D*), whereas chymase-tryptase mast cells have more homogeneous granules (Fig. 4*E,F*)(17). Mast cells were observed in 6 islet datasets from 5 type 1 donors, which were excluding one donor (6204) all of the tryptase subtype (Table 1).

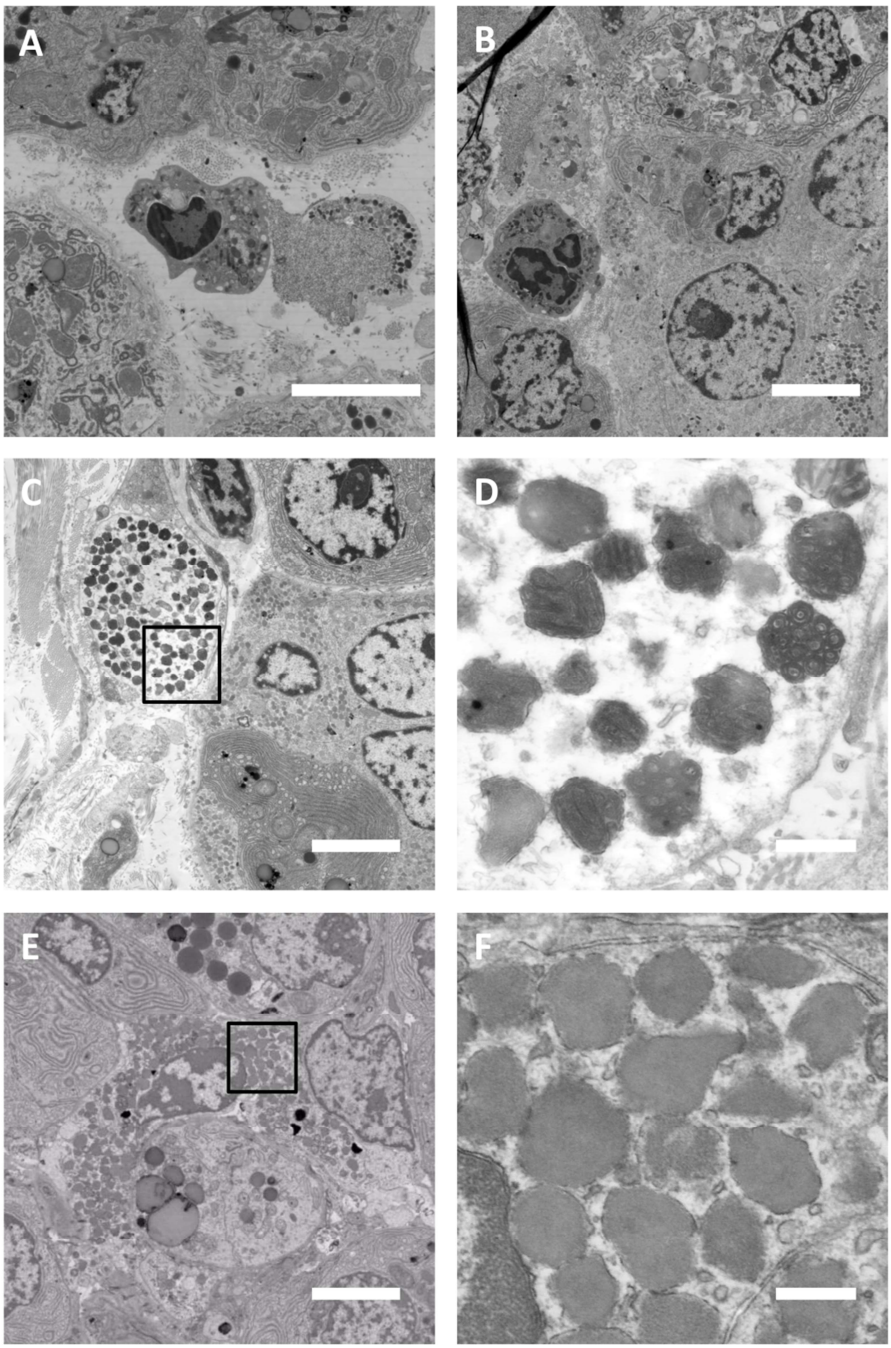

Figure 4 | Identification of mast cells and neutrophils in type 1 diabetes donors. Neutrophils are present in type 1 diabetes samples predominantly located in the exocrine parenchyma (A) and some in the peri-islet region (B). Mast cells were present in both type 1 diabetes (C) and control samples (E). However, subtypes can be distinguished based on granular morphology, with prominent scrolls in tryptase-mast cells in type 1 diabetes (D) and homogenous granules in the tryptase-chymase-mast cells in controls (F). Bars: 5 µm (A-C,E) 0.5 µm (D,F). Donor 6064 (A-B), 6087 (C-D), and 6126 (E-F).

Intermediate cells observed in type 1 diabetes donor samples

The division of islets and acinar cell functions and topology of the pancreas is typically quite strict with hormones and digestive enzymes, respectively (20, 21). Furthermore, as pointed out above, the ultrastructure of both pancreatic regions are very different, e.g. looking at secretory granule morphology. However, unique cells that contained both zymogen and endocrine storage granules were identified (Fig. 5). Such intermediate cells were observed in 2 of 8 type 1 diabetes donors. In donor 6228 (Fig. 5*A*), the intermediate cells were at the periphery of the islet while intermediate cells observed in donor 6063 were localized more scattered throughout a remnant islet (Fig. 5*B*). Elemental analysis of serial sections to determine elemental composition of the granules showed high nitrogen content for both types of granules with an additional phosphorus signal in the endocrine granules in both donors, suggesting these contain glucagon (Fig. 5*C, D*). Therefore, both morphology and EDX analysis indicated that these cells contained glucagon as well as zymogen granules (Fig. 5, Fig. S2).

Discussion

We present the development of the first open-access online database of large field and depth of view islets from organ donors with type 1 diabetes in comparison to donors without diabetes. A disadvantage of traditional EM is due to the inherent laborious sample preparations, static imaging, often precluding dynamic physiologic data extraction, and limited fields of view with a lack of tissue context when acquiring data at high resolution. The latter problem has been overcome by our nanotomy approach as the complete ultrastructure of islet cross-sections are available. As nPOD samples are used to investigate different aspects of disease pathogenesis, these EM datasets can be useful in validating findings using different techniques. One example relates to abnormalities in mitochondria function that were found in other assays and the ultrastructural morphology now can be addressed online (Mathews, C, et al, personal communication). Open access nanotomy, like initiatives on DNA sequences, protein structures etc. allows the sharing of all acquired data for reuse in entirely different research questions. EM information is typically qualitative and could be best combined with more quantitative approaches, e.g. the analysis of many islets phenotypes. A disadvantage is the known heterogeneity of human islets. This counts for islet-to-islet variation, but also variation between humans. In addition, variation in organ donor studies increases because the unique material was acquired post-mortem. This makes these examples of nPOD nanotomy more representative of case studies. This extensive database will grow with the addition of prospective discoveries and inter-connections with other datasets, like nPOD DataShare (25).

ColorEM via EDX was found to be highly valuable in conclusive feature identification through elemental composition (13, 26). All types of secretory granules that contain peptides and proteins are rich in nitrogen. However, in addition to morphology, enrichment of specific elements within the different secretory granules can aid in discriminating cell types. As seen previously in beta cells of rat and mouse via EDX (13, 26) and electron energy loss spectroscopy (27), respectively, insulin-containing granules have a higher sulfur signal due to the relative abundance of cysteines (Fig. 3D)(20). Human glucagon granules are enriched with phosphorus, which is in line with glucagon granules in rodents (13, 26, 27). Furthermore, the granules in mast cell were found to be sulfur-rich, which may be explained by the presence of heparin, heparan sulfate, and relative sulfur-rich proteases (28, 29). Nanotomy and ColorEM was applied to the nPOD biobank to analyze islets of Langerhans in type 1 diabetes.

Type 1 diabetes is considered as a T-cell driven disease however in these donor islets, non-T cell immune cell infiltrates are observed in nPOD (Table 1). Neutrophils were observed in pancreases of 6 type 1 diabetes patients, and in one donor from each of the ND, AAb+, and type 2 diabetes subgroups. The neutrophils are typically found in the exocrine pancreas which is in accordance with similar observations made with both immunohistochemistry (30, 31) and EM (31). This supports the idea that not only islets of Langerhans, but also the exocrine pancreas, is affected during type 1 diabetes (32).

We did not find that mast cells are more prevalent in the type 1 diabetes case as reported recently (33). However, the granular morphology, as clearly present in the nanotomy data, allows for discrimination between two different mast cell subtypes. Tryptase mast cells are predominantly present in type 1 diabetes, whereas control, AAb+, and type 2 diabetes samples contained chymase-tryptase mast cells (Table1). Mast cells are classically known for their role in allergies, but a broader role for mast cells in physiology and immunity is being considered, including recruitment of neutrophils, and production of pro-inflammatory cytokines and chemokines (34).

The role of the exocrine pancreas has received variable attention as a component of type 1 diabetes (reviewed in (32)). Type 1 diabetes patients show a significant reduction in pancreas weight or volume at onset of diabetes and exocrine insufficiency has been reported (35-39). Other findings include alterations in exocrine proteomic profiles compared to healthy controls (40) as well as immunological alterations including increased incidence of various exocrine-specific autoantibodies (41-44), increased infiltration of immune cells (31, 45), and complement activation (46). Furthermore, maintained beta-cell mass (7, 47) but decreased pancreas weight in AAb+ donor samples indicates that exocrine tissue might be affected preceding changes of islets in type 1 diabetes (37). This raises the question of whether endocrine-exocrine interactions have a role in the pathogenesis of type 1 diabetes. Interestingly, we find mixed endocrine-exocrine cells only in type 1 diabetes donors. Similar intermediate cells were found in a diabetic prone rat (13). Since intermediate cells, although without the affected morphology, have been observed in non-diabetic and type 2 diabetes human islets albeit with insulin granules (48-50). Additional methods are needed to determine whether this phenomenon is specifically related to type 1 diabetes pathogenesis or diabetes in general.

nPOD nanotomy allows direct qualitative ultrastructural analysis to investigate subcellular alterations of islets of Langerhans in type 1 diabetes. While each dataset represents one entire cross section of an islet at nm-scale resolution, quantitative analysis with other approaches should be used in parallel. This holds especially true when findings are found in some islets but not in others, localized to certain regions, or are extremely rare. The expanding database of human pancreatic tissue EM marks a milestone in the sharing of raw, extensive, relevant, diabetes-specific data. A first analysis revealed the presence of unsuspected innate immune cells, and intermediate exocrine and endocrine cells were found only in donors with type 1 diabetes. Open access nPOD nanotomy, in conjunction with complementary studies, will expedite better insight into the pathogenesis.

Acknowledgements

We thank Johana Isaza-Correa and Ruby Kalicharan (UMCG) for technical assistance and Jacob Hoogenboom (Delft, The Netherlands) for discussions on EDX. We acknowledge pancreas EM samples from JDRF nPOD staff members and thank Organ Procurement Organizations that partner with nPOD to recover organ donors. This work was supported by the JDRF (6-2006-1140 25-2013-268 to MCT; 25-2012-770 to MCT and BNGG); The Netherlands organization for scientific research (ZonMW 91111.006; STW Microscopy Valley 12718 to BNGG) and the European Association for the Study of Diabetes (EASD; to BNGG).

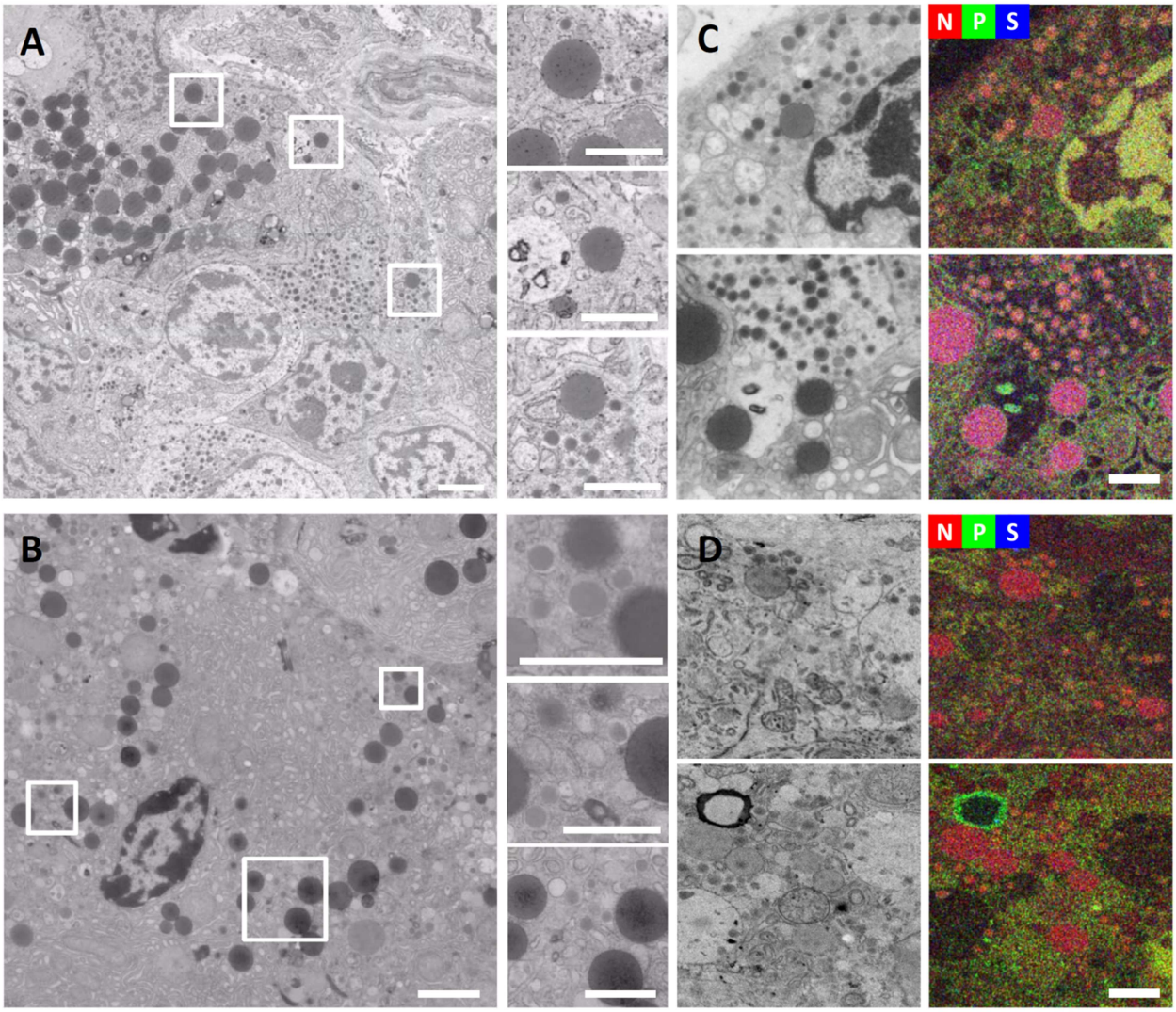

Figure 5 | Endocrine-exocrine mixing in 'intermediate cells' in type 1 diabetes pancreas. Cells containing both exocrine and endocrine granules were observed in donor 6228 at the islet's periphery (A) and 6063 throughout the islet with strong exocrine morphology based on the extensive ER (B). The intermediate cells contained both secretory granules resembling exocrine and glucagon granules based on morphology and elemental content using colorEM (C and D) with exocrine granules in red and glucagon granules in orange (see figure 3 for reference). Absence of uranyl staining in B and D explains the difference in contrast to A and C. Scale bars: 2 µm in overviews, 1 µm in boxed regions, and 1 µm in C and D. Raw EDX data are shown in Fig. S2.

Condition	nPOD donor	Pancreas Region	AAb (RIA)	Age (years)	Duration (years)	Mast cell (number-type)	Neutrophil (number)
ND	6098a	head	-	18	-	**1 -n/a**	0
	6098b					0	0
	6126a	head	-	25	-	**1 -TC**	0
	6126b					0	0
	6126c					**2 -TC**	0
	6130	head	-	5	-	**2 -T**	0
	6131	head	-	24	-	0	0
	6153	head	-	15	-	0	0
	6160	head	-	22	-	**1 -T**	**1**
	6229	head	-	31	-	0	0
	6233	head	-	14	-	0	0
AAb+	6151	head	GADA	30	-	**1 -TC**	0
	6156	head	GADA	40	-	**5 -TC**	**1**
	6158a	head	GADA, mIAA	40	-	0	0
	6158b					**9 -TC**	0
	6197	head	GADA, IA-2A	22	-	0	0
Type 1 Diabetes	6063	head	mIAA	4	3	**2 -T**	**1**
	6064	head	GADA, IA-2A, mIAA, ZnT8A	20	9	**1 -T**	**33***
	6087a	head	ZnT8A, mIAA	18	4	**3 -T**	0
	6087b					**5 -T**	0
	6113	head	mIAA	13	1.6	0	**1**
	6198	tail	GADA, IA-2A, ZnT8A, mIAA	22	3	**2 -T**	**3**
	6204a	body	GADA, mIAA	28	21	0	**12**
	6204b					**1 -TC**	**27**
	6209	head	IA-2A, ZnT8A, mIAA	5	0.25	0	0
	6228a	head	GADA, IA-2A, ZnT8A	13	0	0	0
	6228b	head				0	**3**
	6228c	body				0	0
Type 2 Diabetes	6124	head	-	62	3	0	0
	6127	head	mIAA	45	10	0	0
	6133	head	-	46	20	**1 -TC**	**9***

Table 1 | Mast cells and neutrophils enrichment in pancreas of nPOD donors. Donors are sorted by condition and case-ID, and information on pancreas donor region, type of autoantibodies present as measured by radioimmunoassay (RIA), age of demise, and disease duration is provided. The number of mast cells was recorded as well as the phenotype, tryptase (T), tryptase-chymase (TC), or indistinguishable (n/a). The neutrophils observed were mostly in the exocrine region except those marked (*) had one or more in and/or around the islet.

References

1. Atkinson MA, von Herrath M, Powers AC, Clare-Salzler M: Current concepts on the pathogenesis of type 1 diabetes--considerations for attempts to prevent and reverse the disease. *Diabetes Care.* 38:979-988, 2015

2. Banting FG, Best CH: Pancreatic extracts. 1922. *J Lab Clin Med.* 115:254-272, 1990

3. Shahani S, Shahani L: Use of insulin in diabetes: A century of treatment. *Hong Kong Med J.* 21:553-559, 2015

4. Acerini C: The rise of technology in diabetes care. not all that is new is necessarily better. *Pediatr Diabetes.* 17:168-173, 2016

5. Campbell-Thompson M, Wasserfall C, Kaddis J, Albanese-O'Neill A, Staeva T, Nierras C, Moraski J, Rowe P, Gianani R, Eisenbarth G, Crawford J, Schatz D, Pugliese A, Atkinson M: Network for pancreatic organ donors with diabetes (nPOD): Developing a tissue biobank for type 1 diabetes. *Diabetes Metab Res Rev.* 28:608-617, 2012

6. Campbell-Thompson ML, Heiple T, Montgomery E, Zhang L, Schneider L: Staining protocols for human pancreatic islets. *J Vis Exp.* (63):e4068. doi:e4068, 2012

7. Diedisheim M, Mallone R, Boitard C, Larger E: Beta-cell mass in nondiabetic autoantibody-positive subjects: An analysis based on the network for pancreatic organ donors database. *J Clin Endocrinol Metab.* 101:1390-1397, 2016

8. JDRF nPOD: Online pathology information for investigators - http://www.jdrfnpod.org/for-investigators/online-pathology-information/.

9. Torn C, Hadley D, Lee HS, Hagopian W, Lernmark A, Simell O, Rewers M, Ziegler A, Schatz D, Akolkar B, Onengut-Gumuscu S, Chen WM, Toppari J, Mykkanen J, Ilonen J, Rich SS, She JX, Steck AK, Krischer J, TEDDY Study Group: Role of type 1 diabetes-associated SNPs on risk of autoantibody positivity in the TEDDY study. *Diabetes.* 64:1818-1829, 2015

10. Ravelli RB, Kalicharan RD, Avramut MC, Sjollema KA, Pronk JW, Dijk F, Koster AJ, Visser JT, Faas FG, Giepmans BN: Destruction of tissue, cells and organelles in type 1 diabetic rats presented at macromolecular resolution. *Sci Rep.* 3:1804, 2013

11. Kuipers J, Kalicharan RD, Wolters AH, van Ham TJ, Giepmans BN: Large-scale scanning transmission electron microscopy (nanotomy) of healthy and injured zebrafish brain. *J Vis Exp.* (111). doi:10.3791/53635, 2016

12. Sokol E, Kramer D, Diercks GF, Kuipers J, Jonkman MF, Pas HH, Giepmans BN: Large-scale electron

microscopy maps of patient skin and mucosa provide insight into pathogenesis of blistering diseases. *J Invest Dermatol.* 135:1763-1770, 2015

13. Scotuzzi M, Kuipers J, Wensveen DI, de Boer P, Hagen KC, Hoogenboom JP, Giepmans BN: Multi-color electron microscopy by element-guided identification of cells, organelles and molecules. *Sci Rep.* 7:45970, 2017

14. JDRF nPOD: Online pathology database - http://ahc-path-apr01.ahc.ufl.edu/Login.php.

15. Campbell-Thompson ML, Montgomery EL, Foss RM, Kolheffer KM, Phipps G, Schneider L, Atkinson MA: Collection protocol for human pancreas. *J Vis Exp.* (63):e4039. doi:e4039, 2012

16. Reynolds ES: The use of lead citrate at high pH as an electron-opaque stain in electron microscopy. *J Cell Biol.* 17:208-212, 1963

17. Craig SS, Schechter NM, Schwartz LB: Ultrastructural analysis of maturing human T and TC mast cells in situ. *Lab Invest.* 60:147-157, 1989

18. Pugliese A, Yang M, Kusmarteva I, Heiple T, Vendrame F, Wasserfall C, Rowe P, Moraski JM, Ball S, Jebson L, Schatz DA, Gianani R, Burke GW, Nierras C, Staeva T, Kaddis JS, Campbell-Thompson M, Atkinson MA: The juvenile diabetes research foundation network for pancreatic organ donors with diabetes (nPOD) program: Goals, operational model and emerging findings. *Pediatr Diabetes.* 15:1-9, 2014

19. Pisania A, Weir GC, O'Neil JJ, Omer A, Tchipashvili V, Lei J, Colton CK, Bonner-Weir S: Quantitative analysis of cell composition and purity of human pancreatic islet preparations. *Lab Invest.* 90:1661-1675, 2010

20. Bonner-Weir S: Islets of langerhans: Morphology and postnatal growth. In *Joslin's Diabetes Mellitus.* , 14th ed. Kahn CR, Weir GC,

King GL, Jacobson AM, Moses AC, Smith RJ Eds. Boston, MA, Lippincott, Williams and Wilkins, 2005, p.41-52

21. In't Veld P, Marichal M: Microscopic anatomy of the human islet of langerhans. *Adv Exp Med Biol.* 654:1-19, 2010

22. Lack EE: Pathology of the pancreas, gallbladder, extrahepatic biliary tract, and ampullary region. New York, Oxford University Press, Inc., 2003

23. Dvorak AM: Ultrastructural studies of human basophils and mast cells. *J Histochem Cytochem.* 53:1043-1070, 2005

24. Aronova M, Leapman R: Development of electron energy-loss spectroscopy in the biological sciences. *MRS Bull.* 37:53-62, 2012

25. JDRF nPOD: Online datashare for investigators - https://www.jdrfnpod.org/for-investigators/datashare/.

26. Foster MC, Leapman RD, Li MX, Atwater I: Elemental composition of secretory granules in pancreatic islets of langerhans. *Biophys J.* 64:525-532, 1993

27. Goping G, Pollard HB, Srivastava M, Leapman R: Mapping protein expression in mouse pancreatic islets by immunolabeling and electron energy loss spectrum-imaging. *Microsc Res Tech.* 61:448-456, 2003

28. Huang C, Li L, Krilis SA, Chanasyk K, Tang Y, Li Z, Hunt JE, Stevens RL: Human tryptases alpha and beta/II are functionally distinct due, in part, to a single amino acid difference in one of the surface loops that forms the substrate-binding cleft. *J Biol Chem.* 274:19670-19676, 1999

29. Vukman KV, Forsonits A, Oszvald A, Toth EA, Buzas EI: Mast cell secretome: Soluble and vesicular components. *Semin Cell Dev Biol.* 67:65-73, 2017

30. Korsgren S, Molin Y, Salmela K, Lundgren T, Melhus A, Korsgren O: On the etiology of type 1 diabetes: A new animal model signifying a decisive role for bacteria eliciting an adverse innate immunity response. *Am J Pathol.* 181:1735-1748, 2012

31. Valle A, Giamporcaro GM, Scavini M, Stabilini A, Grogan P, Bianconi E, Sebastiani G, Masini M, Maugeri N, Porretti L, Bonfanti R, Meschi F, De Pellegrin M, Lesma A, Rossini S, Piemonti L, Marchetti P, Dotta F, Bosi E, Battaglia M: Reduction of circulating neutrophils precedes and accompanies type 1 diabetes. *Diabetes.* 62:2072-2077, 2013

32. Campbell-Thompson M, Rodriguez-Calvo T, Battaglia M: Abnormalities of the exocrine pancreas in type 1 diabetes. *Curr Diab Rep.* 15:79-015-0653-y, 2015

33. Martino L, Masini M, Bugliani M, Marselli L, Suleiman M, Boggi U, Nogueira TC, Filipponi F, Occhipinti M, Campani D, Dotta F, Syed F, Eizirik DL, Marchetti P, De Tata V: Mast cells infiltrate pancreatic islets in human type 1 diabetes. *Diabetologia.* 58:2554-2562, 2015

34. Weller CL, Collington SJ, Williams T, Lamb JR: Mast cells in health and disease. *Clin Sci (Lond).* 120:473-484, 2011

35. Hardt PD, Ewald N: Exocrine pancreatic insufficiency in diabetes mellitus: A complication of diabetic neuropathy or a different type of diabetes? *Exp Diabetes Res.* 2011:761950, 2011

36. Li X, Campbell-Thompson M, Wasserfall CH, McGrail K, Posgai A, Schultz AR, Brusko TM, Shuster J, Liang F, Muir A, Schatz D, Haller MJ, Atkinson MA: Serum trypsinogen levels in type 1 diabetes. *Diabetes Care.* 40:577-582, 2017

37. Campbell-Thompson M, Wasserfall C, Montgomery EL, Atkinson MA, Kaddis JS: Pancreas organ weight in individuals with disease-associated autoantibodies at risk for type 1 diabetes. *JAMA.* 308:2337-2339, 2012

38. Campbell-Thompson ML, Kaddis JS, Wasserfall C, Haller MJ, Pugliese A, Schatz DA, Shuster JJ, Atkinson MA: The influence of type 1 diabetes on pancreatic weight. *Diabetologia.* 59:217-221, 2016

39. Virostko J, Hilmes M, Eitel K, Moore DJ, Powers AC: Use of the electronic medical record to assess pancreas size in type 1 diabetes. *PLoS One.* 11:e0158825, 2016

40. Liu CW, Atkinson MA, Zhang Q: Type 1 diabetes cadaveric human pancreata exhibit a unique exocrine tissue proteomic profile. *Proteomics.* 16:1432-1446, 2016

41. Kobayashi T, Nakanishi K, Kajio H, Morinaga S, Sugimoto T, Murase T, Kosaka K: Pancreatic cytokeratin: An antigen of pancreatic exocrine cell

autoantibodies in type 1 (insulin-dependent) diabetes mellitus. *Diabetologia.* 33:363-370, 1990

42. Panicot L, Mas E, Thivolet C, Lombardo D: Circulating antibodies against an exocrine pancreatic enzyme in type 1 diabetes. *Diabetes.* 48:2316-2323, 1999

43. Taniguchi T, Okazaki K, Okamoto M, Seko S, Tanaka J, Uchida K, Nagashima K, Kurose T, Yamada Y, Chiba T, Seino Y: High prevalence of autoantibodies against carbonic anhydrase II and lactoferrin in type 1 diabetes: Concept of autoimmune exocrinopathy and endocrinopathy of the pancreas. *Pancreas.* 27:26-30, 2003

44. Hardt PD, Ewald N, Brockling K, Tanaka S, Endo T, Kloer HU, Bretzel RG, Jaeger C, Shimura H, Kobayashi T: Distinct autoantibodies against exocrine pancreatic antigens in european patients with type 1 diabetes mellitus and non-alcoholic chronic pancreatitis. *JOP.* 9:683-689, 2008

45. Rodriguez-Calvo T, Ekwall O, Amirian N, Zapardiel-Gonzalo J, von Herrath MG: Increased immune cell infiltration of the exocrine pancreas: A possible contribution to the pathogenesis of type 1 diabetes. *Diabetes.* 63:3880-3890, 2014

46. Rowe P, Wasserfall C, Croker B, Campbell-Thompson M, Pugliese A, Atkinson M, Schatz D: Increased complement activation in human type 1 diabetes pancreata. *Diabetes Care.* 36:3815-3817, 2013

47. Campbell-Thompson M, Fu A, Kaddis JS, Wasserfall C, Schatz DA, Pugliese A, Atkinson MA: Insulitis and beta-cell mass in the natural history of type 1 diabetes. *Diabetes.* 65:719-731, 2016

48. Aida K, Saitoh S, Nishida Y, Yokota S, Ohno S, Mao X, Akiyama D, Tanaka S, Awata T, Shimada A, Oikawa Y, Shimura H, Furuya F, Takizawa S, Ichijo M, Ichijo S, Itakura J, Fujii H, Hashiguchi A, Takasawa S, Endo T, Kobayashi T: Distinct cell clusters touching islet cells induce islet cell replication in association with over-expression of regenerating gene (REG) protein in fulminant type 1 diabetes. *PLoS One.* 9:e95110, 2014

49. Cossel L: Electron microscopic demonstration of intermediate cells in the healthy adult human pancreas. *Virchows Arch B Cell Pathol Incl Mol Pathol.* 52:283-287, 1986

50. Masini M, Marselli L, Himpe E, Martino L, Bugliani M, Suleiman M, Boggi U, Filipponi F, Occhipinti M, Bouwens L, De Tata V, Marchetti P: Co-localization of acinar markers and insulin in pancreatic cells of subjects with type 2 diabetes. *PLoS One.* 12:e0179398, 2017

Supplementary information

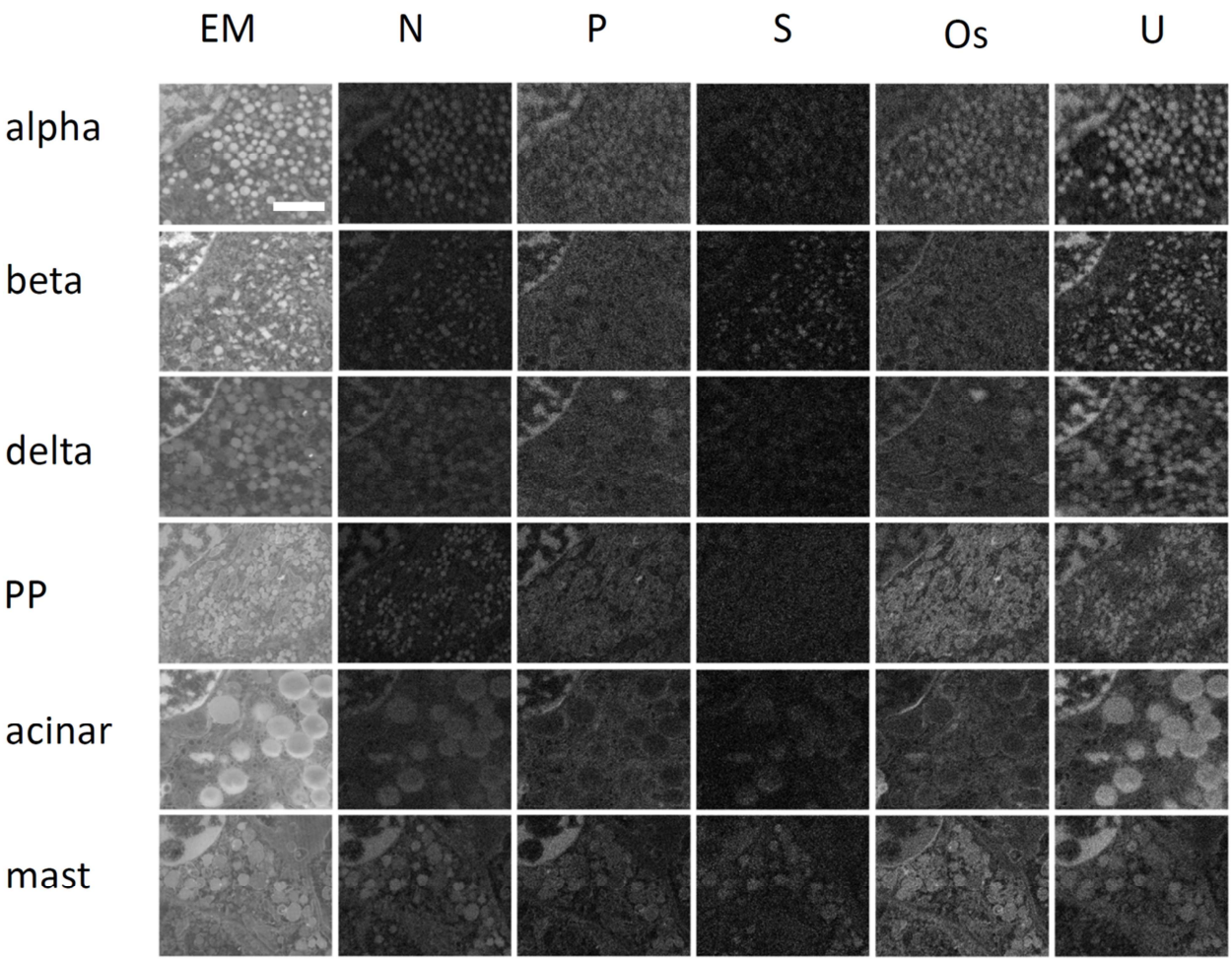

Figure S1 | Raw EDX data from different cell types. Element specific images displaying nitrogen (N), phosphorus (P), sulfur (S), osmium (Os), uranium (U) are shown. See figure 3 for further details. Bar: 2 µm.

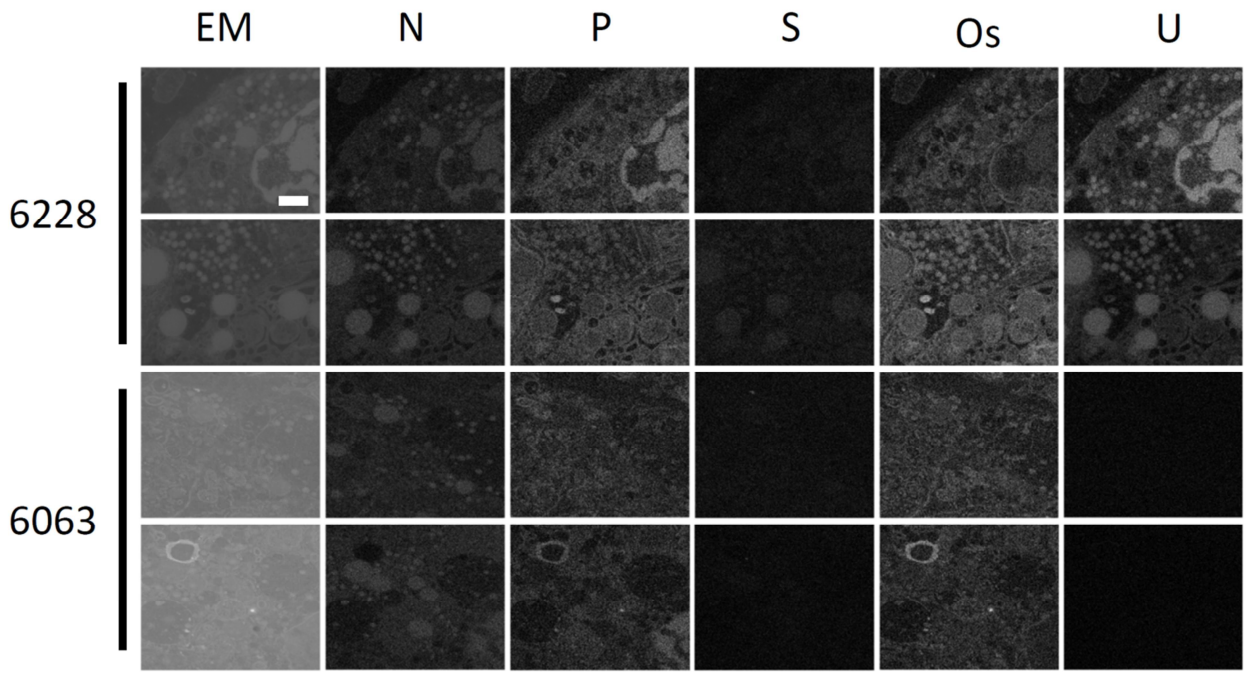

Figure S2 | Raw EDX data from intermediate cells. Element specific images displaying nitrogen (N), phosphorus (P), sulfur (S), osmium (Os), uranium (U) are shown. See figure 3 for further details. Bar: 1 µm.

Chapter 5b

Exocrine pancreas cell lysates specifically evoke beta cell stress

Pascal de Boer, B.H. Peter Duinkerken, Marlinda Everaars and Ben N.G. Giepmans

Department of Cell Biology, University Medical Center Groningen, Groningen, the Netherlands

Work in progress: The work in this chapter was proposed by PdB and BNGG and granted by the European association for the study of diabetes (EASD) based on our findings in chapter 5a.

Abstract

The trigger for type 1 diabetes (T1D) is unknown. Recent studies revealed that the exocrine pancreas is affected in T1D patients, which can already be observed before the onset of T1D. In chapters 4b and 5a rare intermediate endocrine and exocrine cells were observed in islets of 'pre-diabetic' rats and early onset T1D donors respectively. In this chapter, a functional follow-up pilot study is performed to elucidate whether lysates specifically of exocrine cells could induce beta cell stress. The pro-inflammatory C-X-C motif chemokine ligand 10 (CXCL-10) gene expression is increased in insulinoma cells upon exocrine cell lysate treatment. Thus far, only CXCL-10 was upregulated of the beta cell stress associated genes tested. Currently endoplasmic reticulum (ER) stress markers are being investigated. Taken together, exocrine cell damage might provoke a pro-inflammatory reaction by beta cells which should be further elucidated upon experimental model optimization as proposed in this chapter.

Introduction

Type 1 diabetes (T1D) is an autoimmune disorder in which the insulin producing beta cells from the islets of Langerhans in the pancreas are destroyed resulting in elevated and uncontrolled blood glucose with accompanying severe complications. Compiling evidence indicate that beta cell stress and defects precede the massive beta cell death upon T cell infiltration and clinical onset of T1D[1-3]. However, underlying mechanism(s) including intrinsic or extrinsic triggers involved in beta cell dysfunction are not clear. Chapter 4b and 5a of this thesis describe the appearance of intermediate exocrine and endocrine cells displaying an affected ultrastructure in EM in 'pre-diabetic' BB rats and early onset T1D nPOD islets respectively. Subsequently, we proposed that exocrine cell damage triggers beta cell stress at the onset of T1D. This is in line with a current growing notion that the exocrine pancreas, and not only the islets of Langerhans, is affected during T1D[4].

Functional follow up experiments aim to address whether beta cells acquire a stressed phenotype specifically upon treatment with exocrine cell lysates. Hallmarks for early T1D associated beta cell stress include the production of pro-inflammatory mediators[5, 6], human leukocyte antigen (HLA) class I hyperexpression[7], endoplasmic reticulum (ER) stress[8], and neoantigen formation[9]. We find that the pro-inflammatory chemokine C-X-C motif chemokine 10 (CXCL-10) mRNA expression is most prominently increased in insulinoma cells upon exocrine lysate treatment. This might indicate that exocrine cell damage could evoke a pro-inflammatory response following beta cell stress.

Material and methods

Cell culturing

Rat insulinoma (RIN-m5F), and mouse macrophage (J774) cell lines were cultured in Dulbecco's Modified Eagle Medium (DMEM; Gibco, 42430-025) supplemented with 1% penicillin/streptomycin (pen/strep; PAA), 10% fetal calf serum (FCS; Greiner Bio-one), and beta-mercaptoethanol (BME; Sigma-Aldrich) to a final concentration of 72 µM was added to RIN-m5F medium. The rat pancreatic exocrine cell line AR42J was cultured in DMEM (Gibco, 10-013-CVK) supplemented with 1% pen/strep and 20% FCS. Table 1 shows an overview of cell lines used in this study.

Lysate stimulation

Min6, RIN-m5F, and J774 cells were seeded in a 24 wells plate at a density of 1.0 x 10^5 cells/well and left to adhere for 24 hours. Upon trypsinization and centrifugation, non-seeded Min6, RIN-m5F and AR42J cells were resuspended in dH_2O in a concentration of 1.0 x 10^5 cells/ 100 µl and left for 15 minutes to induce osmotic cell lysis. Subsequently stimulation of the seeded cells was performed by adding 100 µl of the cell lysates, i.e. an equivalent of 1.0 x 10^5 cells, +/- the presence of lipopolysacheride (LPS, 200 ng/ml). As a control 100 µl dH_2O +/- LPS was added to the seeded cells. Stimulated cells incubated for 24 hours before further processing.

mRNA extraction and real-time PCR

An RNeasy Mini kit (Qiagen) was for cell lyses of stimulated cells in accordance with the manufacturer's instructions. To avoid RNA degradation by RNases, BME was added to the RTL lysis buffer as proposed in the manufacturer's protocol. Reverse transcription of the mRNA for cDNA synthesis was performed with the iScript^{tm} cDNA Synthesis Kit (Bio-Rad) according to the manufacturer's manual. Quantitative real-time PCR was performed using SYBR Green (SsoAdvanced Universal^{tm} SYBR Green Supermix; Bio-Rad) and a StepOnePLus Real-Time PCR system (ThermoFisher). Expression values were corrected by the housekeeping genes β-actin and glyceraldehyde 3-phosphate dehydrogenase (GAPDH). Primer sequences are listed in supplementary table 1.

Cell line name	Cell type	Species
RIN-m5F	Insulinoma	Rat
AR42J	Exocrine pancreas	Rat
J774	Macrophages	mouse

Table 1 | Overview of cell lines used in this study

Results and discussion

Mechanisms and triggers leading to autoimmune attack against beta cells are poorly understood. In this thesis intermediate endocrine and exocrine cells with an affected ultrastructure in 'pre-diabetic' BB rats (chapter 4b)[10] and early onset human T1D donor islets (chapter 5a) are described. Subsequently, we proposed that damaged exocrine cells could trigger beta cell stress at the onset of T1D, which is functionally addressed in this chapter.

Pro-inflammatory cytokine and chemokine production by beta cells is a sign of beta cell stress and might evoke a local immune response[5, 6]. Expression of the chemokine CXCL10 is increased in RIN-m5F cells upon stimulation with AR42J cell lysates, and not with RIN-m5F cell lysate stimulation (Figure 1). Furthermore LPS, used as co-stimulator[11] and as additional control for exocrine lysate specificity, did not evoke increased CXCL-10 expression. As a first indicator for beta cell specific CXCL-10 expression upon exocrine lysate stimulation, expression was not increased in J774 macrophages upon stimulation (Figure 1). Responsiveness of J774 cells was indicated by increased CXCL-10 expression upon LPS treatment. Expression of the pro-inflammatory cytokines interleukin 1 beta (IL-1β) and IL-6 was not increased by insulinoma cells upon exocrine lysate stimulation (Figure 2). These cytokines were upregulated in J774 macrophages upon LPS treatment, but not exocrine lysates, which shows LPS effectiveness (Figure 2). Ideally, other target cells should be stimulated with exocrine lysates to elucidate the beta cell specificity of the response, these would for example include alpha cells. CXCL-10 serum levels are specifically elevated during early onset T1D[12] and is

known as a potent chemoattractant for T cells[13]. Furthermore, histopathology showed that CXCL-10 is highly present in early onset T1D donor islets accompanied with infiltrated T cells expressing the CXCR-3 receptor for CXCL-10[14]. Moreover, beta cells have been identified as the resource for CXCL-10 in both animal models[15] and recent onset T1D patient material[16].

Abbreviation	Full name	Relevance
CXCL-10	C-X-C motif chemokine 10	Chemoattractant for immune cells
CXCR-3	C-X-C motif chemokine receptor 3	Receptor for CXCL-10 on target immune cells
IL-1β	Interleukin 1 beta	Pro-inflammatory cytokine
IL-6	Interleukin 6	Pro-inflammatory cytokine
XBP-1	X-Box binding protein 1	ER stress: alternative mRNA splicing of XBP-1
CHOP	C/EBP homologous protein	Increased expression upon ER stress
BiP	binding immunoglobulin protein	Increased expression upon ER stress
LPS	Lipopolysacharide	Cell wall component of gram negative bacteria

Table 2 | Explanation of important molecules discussed in this chapter.

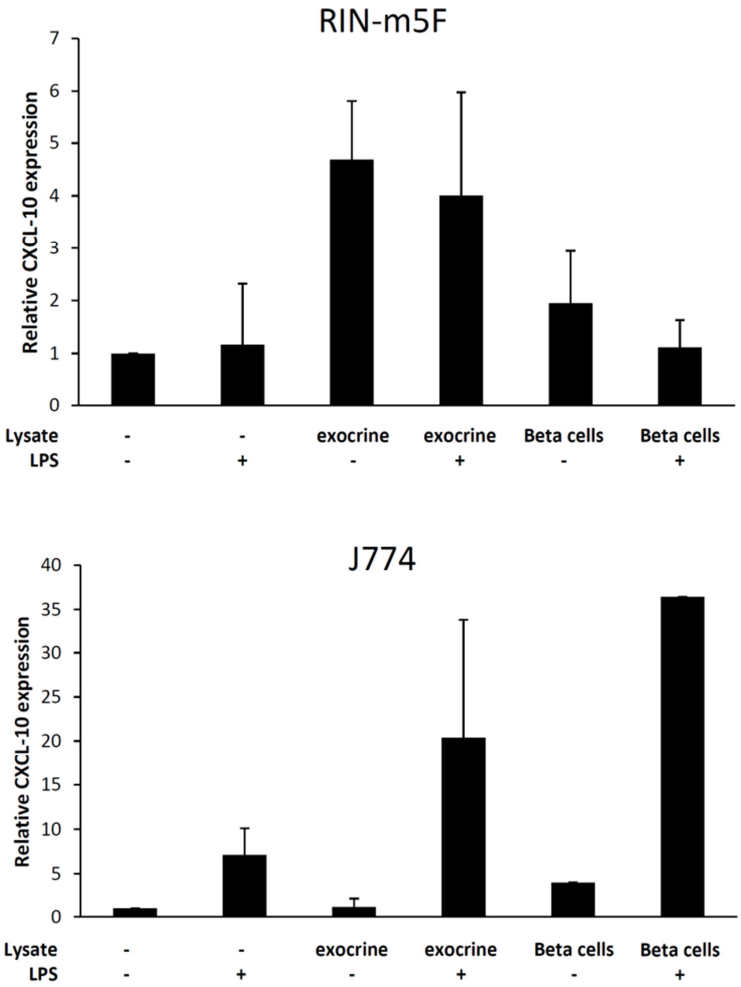

Figure 1 | Exocrine lysates evoke CXCL-10 expression in RIN-m5F cells. CXCL-10 mRNA expression by RIN-m5F cells is increased upon exocrine lysate stimulation compared to unstimulated controls (upper panel). Moreover, lysates from beta cells do not increase CXCL-10 expression. Furthermore, LPS has no effect on CXCL-10 expression from RIN-m5F cells. Only LPS was able to increase CXCL-10 expression by J774 macrophages, and not exocrine or beta cell lysates. N=3 except for the beta cell lysate treated J774 cells, which is n=1.

Additional to assessing a pro-inflammatory response in beta cells, endoplasmic reticulum (ER) stress is a prominent hallmark for early T1D associated beta cell stress [8, 17]. Moreover, ER stress is considered as a driving force in neoantigen formation, which is increasingly considered as a link between beta cell stress and autoimmune reactivity[9]. Here, ER stress in beta cells, assessed by spliced X-Box binding protein 1 (XBP-1s) mRNA expression[17], was not observed upon exocrine lysate stimulation (Figure S1). Next experiments will assess the involvement of other ER stress markers previously linked to stressed beta cells in T1D, including binding immunoglobulin protein (BiP)[17] and C/EBP homologous protein (CHOP)[18]. Also, the degree of neoantigen formation could be investigated, for example through monitoring aberrant post-translation modifications[19] or defective ribosomal products[20]

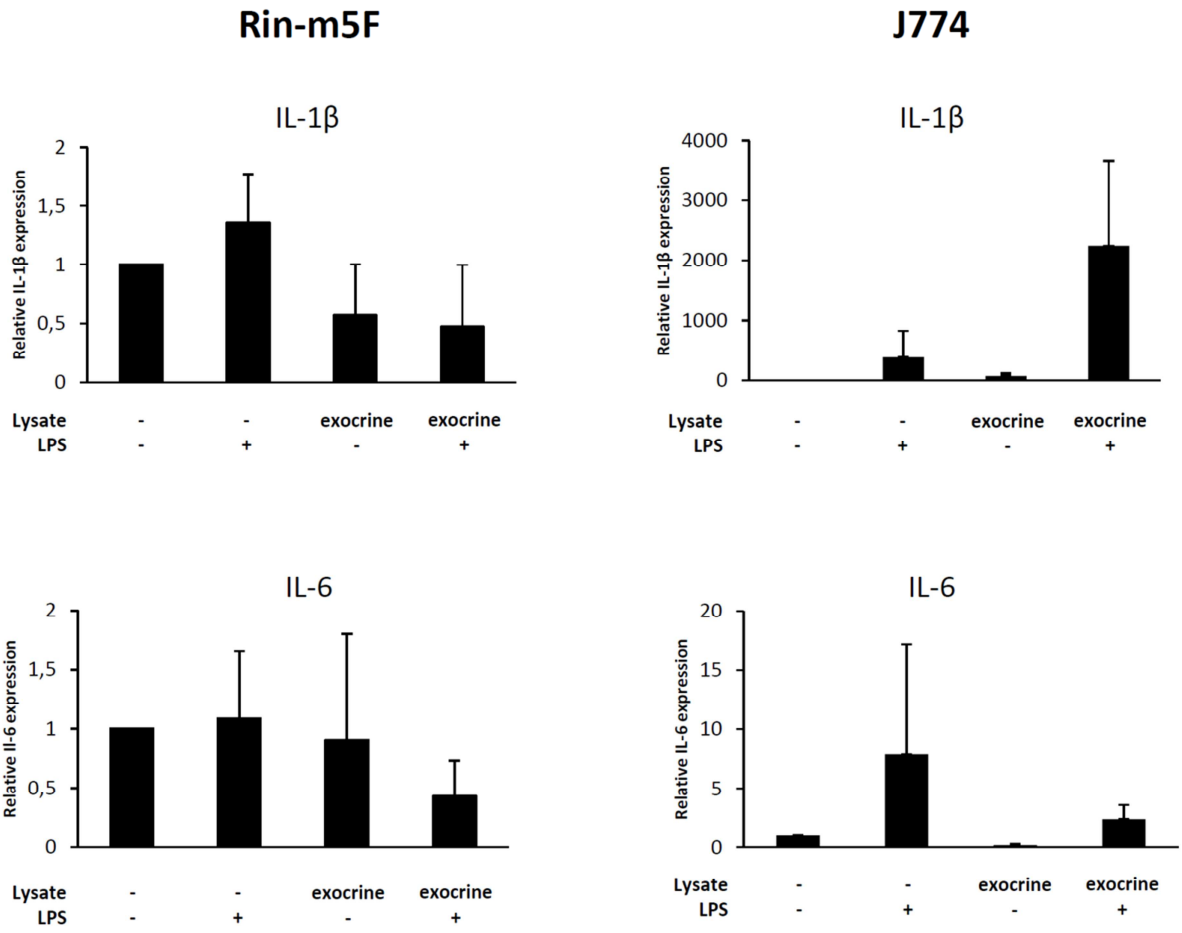

Figure 2 | No increase in pro-inflammatory cytokines by RIN-m5F cells upon exocrine lysate stimulation. mRNA expression of the pro-inflammatory cytokines IL-1β and IL-1 by RIN-m5F cells are not increased upon stimulation of exocrine lysates nor by LPS stimulation (left). These pro-inflammatory cytokines are increased in J774 macrophages upon LPS treatment but also here exocrine lysate stimulation did not increase cytokine expression (right). N=3

Although CXCL-10 mRNA expression by beta cells upon exocrine lysate stimulation is promising, the model used is limited in reflecting the interaction between exocrine damage and beta cells in T1D. First, lysate creation through osmotic shock is a fairly uncontrolled process, and pancreatic protease activity could already break down exocrine mediators before addition to the target cells. Therefore, to avoid lysate transfer, the fluorescent photosensitizing protein supernova[21] will be expressed in exocrine cells only in a co-culture with beta cells. Upon excitation with intense green light exocrine cells are selectively ablated in the vicinity with beta cells, followed by monitoring beta cell stress. First results on selective cell death through photosensitizing supernova tagged to either mitochondria or the plasma membrane look promising (data not shown).

A next limitation of the current model is that it is completely based on cell lines. Insulinoma cells do not have the real beta cell phenotype and can only be used for basic mechanistic studies. Therefore, the extend of exocrine damage in terms of beta cell stress on for example isolated islets or induced pluripotent stem cell (iPSC), possibly T1D patient, derived beta cells[22]. Furthermore, the supernova based exocrine cell ablation could be translated to an in vivo model such as the zebrafish.

Conclusion

The trigger for T1D is unknown. Recent findings show that the exocrine pancreas is affected during T1D[4], which can already be observed before the onset of T1D[23]. Our imaging studies revealed that intermediate exocrine-endocrine cells with stressed features have been observed in 'pre-diabetic' BB rats and early onset human T1D donor islets (Chapters 4b[10], and 5a of this thesis). Results from a first functional follow-up pilot suggest that beta cells acquire a pro-inflammatory phenotype, by the increase of CXCL-10 expression, specifically upon stimulation with exocrine cell lysates. These first data encourage to further investigate a potential role for endocrine-exocrine interactions at the onset of T1D and subsequent model optimization would better reflect T1D associated beta cell stress upon exocrine cell damage.

Acknowledgments

Our work relevant to this chapter is supported by the Netherlands organization for scientific research (STW Microscopy Valley 12718), the Jan Kornelis de Cock Stichting and the *European association for the study of diabetes (EASD).*

References

1. Ferrannini, E. *et al*. Progression to diabetes in relatives of type 1 diabetic patients: mechanisms and mode of onset. *Diabetes* **59**, 679-685 (2010).

2. O'Sullivan-Murphy, B. & Urano, F. ER stress as a trigger for beta-cell dysfunction and autoimmunity in type 1 diabetes. *Diabetes* **61**, 780-781 (2012).

3. Soleimanpour, S. A. & Stoffers, D. A. The pancreatic beta cell and type 1 diabetes: innocent bystander or active participant? *Trends Endocrinol. Metab.* **24**, 324-331 (2013).

4. Campbell-Thompson, M., Rodriguez-Calvo, T. & Battaglia, M. Abnormalities of the Exocrine Pancreas in Type 1 Diabetes. *Curr. Diab Rep.* **15**, 79-015-0653-y (2015).

5. Foulis, A. K., Farquharson, M. A. & Meager, A. Immunoreactive alpha-interferon in insulin-secreting beta cells in type 1 diabetes mellitus. *Lancet* **2**, 1423-1427 (1987).

6. Donath, M. Y., Boni-Schnetzler, M., Ellingsgaard, H., Halban, P. A. & Ehses, J. A. Cytokine production by islets in health and diabetes: cellular origin, regulation and function. *Trends Endocrinol. Metab.* **21**, 261-267 (2010).

7. Richardson, S. J. *et al*. Islet cell hyperexpression of HLA class I antigens: a defining feature in type 1 diabetes. *Diabetologia* **59**, 2448-2458 (2016).

8. Marhfour, I. *et al*. Expression of endoplasmic reticulum stress markers in the islets of patients with type 1 diabetes. *Diabetologia* **55**, 2417-2420 (2012).

9. Kracht, M. J., Zaldumbide, A. & Roep, B. O. Neoantigens and Microenvironment in Type 1 Diabetes: Lessons from Antitumor Immunity. *Trends Endocrinol. Metab.* **27**, 353-362 (2016).

10. Scotuzzi, M. *et al*. Multi-color electron microscopy by element-guided identification of cells, organelles and molecules. *Sci. Rep.* **7**, 45970 (2017).

11. Garay-Malpartida, H. M. *et al*. Toll-like receptor 4 (TLR4) expression in human and murine pancreatic beta-cells affects cell viability and insulin homeostasis. *BMC Immunol.* **12**, 18-2172-12-18 (2011).

12. Antonelli, A. *et al*. Chemokine (C-X-C motif) ligand (CXCL)10 in autoimmune diseases. *Autoimmun. Rev.* **13**, 272-280 (2014).

13. Groom, J. R. & Luster, A. D. CXCR3 ligands: redundant, collaborative and antagonistic functions. *Immunol. Cell Biol.* **89**, 207-215 (2011).

14. Roep, B. O. *et al*. Islet inflammation and CXCL10 in recent-onset type 1 diabetes. *Clin. Exp. Immunol.* **159**, 338-343 (2010).

15. Frigerio, S. *et al*. Beta cells are responsible for CXCR3-mediated T-cell infiltration in insulitis. *Nat. Med.* **8**, 1414-1420 (2002).

16. Uno, S. *et al*. Expression of chemokines, CXC chemokine ligand 10 (CXCL10) and CXCR3 in the inflamed islets of patients with recent-onset autoimmune type 1 diabetes. *Endocr. J.* **57**, 991-996 (2010).

17. Tersey, S. A. *et al*. Islet beta-cell endoplasmic reticulum stress precedes the onset of type 1 diabetes in the nonobese diabetic mouse model. *Diabetes* **61**, 818-827 (2012).

18. Allagnat, F. *et al*. C/EBP homologous protein contributes to cytokine-induced pro-inflammatory responses and apoptosis in beta-cells. *Cell Death Differ.* **19**, 1836-1846 (2012).

19. Marre, M. L. & Piganelli, J. D. Environmental Factors Contribute to beta Cell Endoplasmic Reticulum Stress and Neo-Antigen Formation in Type 1 Diabetes. *Front. Endocrinol. (Lausanne)* **8**, 262 (2017).

20. Kracht, M. J. *et al*. Autoimmunity against a defective ribosomal insulin gene product in type 1 diabetes. *Nat. Med.* (2017).

21. Takemoto, K. *et al*. SuperNova, a monomeric photosensitizing fluorescent protein for chromophore-assisted light inactivation. *Sci. Rep.* **3**, 2629 (2013).

22. Millman, J. R. *et al*. Generation of stem cell-derived beta-cells from patients with type 1 diabetes. *Nat. Commun.* **7**, 11463 (2016).

23. Campbell-Thompson, M., Wasserfall, C., Montgomery, E. L., Atkinson, M. A. & Kaddis, J. S. Pancreas organ weight in individuals with disease-associated autoantibodies at risk for type 1 diabetes. *JAMA* **308**, 2337-2339 (2012).

Supplementary information

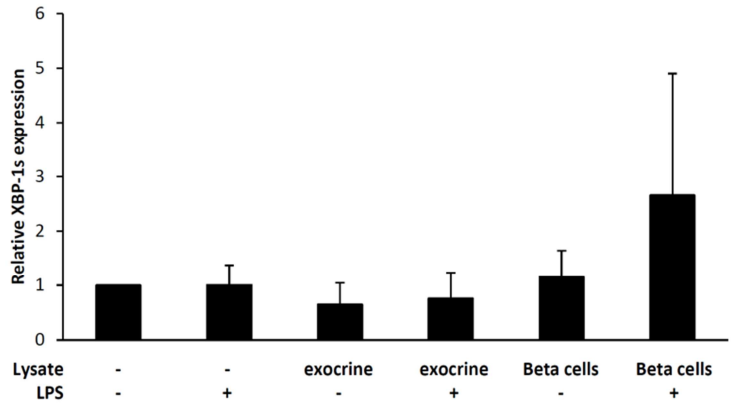

Supplementary figure 1 | No increased spliced XBP-1 expression by RIN-m5F cells upon exocrine cell stimulation. No changes in the ER stress marker XBP-1s mRNA expression by RIN-m5F cells could be observed upon stimulation with exocrine and beta cell lysates or LPS treatment.

Supplementary table 1| RT-qPCR primer sequences used for this study.

Primer	Sequence 5' to 3'
Rat CXCL-10 FWD	GCATGTTGAGATCATTGCCAC
Rat CXL-10 REV	CGTCTCTCTGCTGTCCATCG
Mouse CXCL-10 FWD	ATGACGGGCCAGTGAGAATG
Mouse CXCL-10 REV	TCGTGGCAATGATCTCAACAC
Rat IL-1β FWD	TAGCAGCTTTCGACAGTGAGG
Rat IL-1β REV	CTCCACGGGCAAGACATAGG
Mouse IL-1β FWD	TGCCACCTTTTGACAGTGATG
Mouse IL-1β REV	ATGTGCTGCTGCGAGATTTG
Rat IL-6 FWD	CATTCTGTCTCGAGCCCACC
Rat IL-6 REV	GCTGGAAGTCTCTTGCGGAG
Mouse IL-6 FWD	ACAAAGCCAGAGTCCTTCAGAG
Mouse IL-6 REV	TGTGACTCCAGCTTATCTCTTGG
Rat XBP-1s FWD	CTGAGTCCGAATCAGGTGCAG
Rat XBP-1s REV	ATCCATGGGAAGATGTTCTGG
Mouse XBP-1s FWD	CTGAGTCCGAATCAGGTGCAG
Mouse XBP-1s REV	GTCCATGGGAAGATGTTCTGG
Rat β-Actin FWD	AGATCAAGATCATTGCTCCTCCTG
Rat β-Actin REV	GGGTGTAAAACGCAGCTCAG
Mouse β-Actin FWD	CCACTGTCGAGTCGCGTCC
Mouse β-Actin REV	GTCATCCATGGCGAACTGGTG
Rat GAPDH FWD	GACATGCCGCCTGGAGAAAC
Rat GAPDH REV	AGCCCAGGATGCCCTTTAGT
Mouse GAPDH FWD	CATGGCCTTCCGTGTTCCTA
Mouse GAPDH REV	CCTGCTTCACCACCTTCTTGAT

Chapter 6

Summary, general discussion and perspectives

Summary and discussion

Implementation of various microscopy techniques has been essential to study the regulation of life and disease for many years. Continuously ongoing development of hardware, software, molecular targeting etc. enables to see an increasing amount of molecular features at high resolution. CLEM utilizes the strengths of both fluorescent light- and EM to complement their respective limitations. LM is used for specific and effective molecular targeting, possible followed by live cell imaging, and provides color to grey-scaled EM. Subsequently, EM provides high resolution context to data recorded with LM. **Chapter 2** reviewed recent CLEM developments on sample preparation, data acquisition and correlation, dedicated probes, and future perspectives[1]. Furthermore, guidelines with tips and tricks, including a literature overview of past performed CLEM applications (chapter 2 table S1), for novel user is provided. As many CLEM approaches are possible, choice of CLEM is primarily guided by the kind and size of material and the specific research question. Furthermore, CLEM experiments depend on whether pre- or post-embedding labeling applies, the possibility for genetically encoded tags, epitope recognition, and microscope availability. Since many specialized and often expensive equipment exist, such as integrated microscopes, dedicated sample holders, 3D EM microscopes etc., for a novel user with a more complicated research questions it is advisable to collaborate with experienced laboratories. However, more straightforward approaches can also be sufficient by using standard confocal microscopes and EM equipment available at most research institutes combined with regular labeling strategies and sample preparation.

For many years a large gap between the imaging scales of LM and EM existed. With the development of super-resolution fluorescent microscopy LM scales are approaching EM[2, 3]. On the other hand, a recent boost in development of high content 3D and 2D EM techniques bridges EM further to LM scales[4, 5]. Classical transmission EM (TEM) on ultrathin sections at high resolution is restricted to a field of view of a few micrometers leaving out the complete cellular or tissue context. With large-scale scanning transmission EM (STEM), complete tissue cross sections can be recorded for 'google-earth'-like, post-acquisition analysis, called nanotomy for nano-anatomy[6, 7] which is shared open access upon publication. However, the vast amount of grey-scaled data recorded with nanotomy is hard to analyze. The aim here was to introduce color to these datasets using affinity based probes to label endogenous targets in (human) tissue which is impossible with genetically encoded tags.

Identification of cells and structures can be achieved with post-embedding immunolabeling using quantum dots (QDs) such as described in **Chapter 3**[8]. Post-embedding immunolabeling provides a superior ultrastructure preservation compared to pre-embedding labeling, since permeabilization required for pre-embedding labeling strongly affects the ultrastructure[9]. Furthermore EM visible nanoparticles have a low penetration depth in cells and tissue[10]. However, in most cases immunolabeling on epon sections as performed in chapter 3 is often unsuccessful since epitopes are masked and affected by strong fixation and the resin. Only about 10% of the tested targets showed positive labeling (data not shown). Post-embedding labeling probably depends in part on the concentration of the target molecules, for example insulin and amylase are present at high concentrations in their respective secretory granules and successfully labeled. Adapted sample preparation might increase labeling efficiency, such as osmium-free embedding, harsh etching, or embedding in slightly hydrophilic resins[11-13]. However, these approaches again often affect the

ultrastructure preservation. Therefore choosing a method for immunoEM is a balance between efficiency and preservation. The golden standard for immunoEM is the Tokuyasu method using thawing of cryosections[14]. However, homogenous cryo-fixation, required for Tokuyasu, of bigger tissue sections is often not possible.

Integrated LM and EM in one microscope, such as the SECOM (Delmic; Delft, The Netherlands), have been developed to facilitate high precision CLEM overlays and circumvent possible damage from sample transfer between microscopes[15]. Integrated CLEM requires fluorescent EM samples, which is usually quenched by osmium during EM sample preparation. Protocols have been developed for fluorescence preservation of FPs in cultured cells[16, 17]. However, post-embedding immunolabeling with fluorescent probes can also be used for labeling of endogenous proteins in tissue sections[18].

Post-embedding immunolabeling with QDs showed a tenfold increased labeling efficiency compared with the more classically applied immunogold (**Chapter 3**)[8]. Possibly because of a strong steric hindrance of gold particles[19]. Furthermore, QDs are both fluorescent and electron dense, therefore very suitable for CLEM purposes (chapter 2 figure 2a)[1]. QD contrast is less than immunogold and are therefore most times masked by tissue contrast when heavy metal staining is applied. When uranyl acetate and lead citrate staining is omitted QDs are well visible. However, uranyl and lead are required for proper TEM imaging. With STEM on the other hand, acquisition contrast is sufficient in the absence of heavy metal staining, making it possible to identify QDs within a proper visible ultrastructure.

The availability of CLEM probes such as QDs is rather rare, since most probes are either fluorescent or electron dense, or too large for high precision targeting. The requirement of electron density can be circumvented by inducing photon emission upon electron beam excitation, cathodoluminescence (CL), by specific probes which can then be detected with the SECOM. Subsequently, the photon originating spot can be localized at nanometer resolution. Fluorescent nanodiamonds (FNDs) are CL potent nanoparticles. In **Chapter 4a** high resolution CL from FNDs in ultrathin epon sections was detected after phagocytosis and immunolabeling upon streptavidin conjugation of the particles[20]. Thus far, most CL studies were performed using large 100-150 nm sized FNDs and in uptake assays only in a biological context[21, 22]. Although FNDs showed potential as a novel CLEM probe, they still sized in a 40-70 nm range, compared to 10-15 nm QDs, and have a high polydispersity. Furthermore, immunolabeling efficiency of streptavidin-conjugated FNDs was low compared to QDs. However, these first results might provide an avenue for further optimization for FND CLEM applications.

In **Chapter 4b** another approach to introduce color using the primary electron beam was described called electron dispersive X-ray spectroscopy (EDX)[23]. When interacting with a sample, the primary electron beam may eject inner shell electrons from the atoms present creating an electron vacancy. An electron from a higher energy outer shell then fills the vacancy and the difference in energy is released as an element specific X-ray. By adding a special EDX detector to a SEM the elemental content per pixel can be fingerprinted and translated to color image with EM resolution ('colorEM'). The application of EDX in life sciences has been limited since EDX detectors lacked sensitivity to discriminate elements in biological samples which mainly consist of carbon. The use of a high-sensitive silicon drift detector (SDD)[24] with high current in a high resolution SEM now enables to determine subcellular variations in elemental composition at the nanoscale in ultrathin biological samples. Here nanoparticles with different elemental composition, nanogold and cadmium containing QDs, could be discriminated upon post-embedding labeling. Furthermore, subcellular structures could be discriminated based on enrichment of endogenous elements such as sulfur in insulin granules since insulin contains a high number of cysteines. Moreover, different cell types in rat islets of Langerhans could be discriminated based on specific granular elemental enrichment.

ColorEM was pioneered on islets of Langerhans of a normoglycaemic diabetic prone BioBreeding (BB) rat, a model for type 1 diabetes (T1D). Unexpectedly, colorEM combined with post-embedding immulabeling revealed endocrine cells at the islet's border contained additional granules from the exocrine pancreas accompanied with an overall affected ultrastructure. These intermediate cells are solely observed in islets of diabetic prone and not the control diabetic resistant rat (unpublished data), which may hint to a harmful interaction between exocrine and endocrine at the onset of diabetes in BB rats.

The mechanism(s) initiating autoimmune destruction of insulin producing beta cells in the islets of Langerhans resulting in T1D are still poorly understood precluding alternatives for insulin therapy. Knowledge of cellular composition and the islets' microenvironment under both T1D and non-diabetic conditions is key to understand T1D etiology. Nanotomy has been pioneered in the BB rat model for unbiased analysis of T1D pathology at the nano scale during different stages of the disease[5]. Although different T1D animal models provided invaluable information about autoimmune mediated beta cell death, there are major discrepancies between animal model and human T1D pathogenesis[25, 26]. Therefore, an online nanotomy repository of human T1D pancreatic tissue from the network of pancreatic organ donors (nPOD) has been created, as described in **Chapter 5a**. The repository will become open access upon publication and datasets are coupled to a specific donor number. Although the limited datasets per donor makes the repository less suitable for quantitative analysis, a qualitative survey on specific subcellular alterations can have great added value to findings with other assays by other nPOD researchers.

T1D is considered as a T cell driven autoimmune disease[27]. A first analysis of the nPOD nanotomy database revealed to presence of unexpected immune cells, including a mast cell subtype specifically present in T1D donor tissue. Upon further inspection of the database combined with EDX analysis endocrine-exocrine intermediate cells in islets of two out of eight T1D donors, and not in non-diabetic donors, were identified. Since intermediate cells have been observed in early-onset T1D human donor islets and in 'pre-diabetic' rats, we hypothesized that exocrine cell damage triggers beta cell stress at T1D onset. This is in line with a current growing notion that the exocrine pancreas, and not only the islets of Langerhans, is affected during T1D[28]. Patients have a significantly reduced pancreas while islets compose just a few percent of the whole pancreas, and exocrine insufficiency has been reported[29-31]. Moreover, a decreased pancreas weight was already observed in autoantibody positive donors, known to have maintained beta cell mass, indicating that exocrine tissue might be affected before changes of islets in T1D[32]. A functional follow up pilot, described in **chapter 5b**, upon static EM experiments suggest pro-inflammatory response by beta cells after exocrine stimulation. Insulin producing cell lines showed increased mRNA expression of the C-X-C motif chemokine ligand 10 (CXCL-10) upon treatment with exocrine cell line lysates compared to both a negative control and beta cell lysate treatment. CXCL10 is a potent chemoattractant for T cells[33] and its expression is strongly associated with early onset T1D[34]. Furthermore, beta cells have been identified as a possible resource for CXCL10 during T1D[35, 36].

Future perspectives

For multi-target CLEM labeling, i.e. color and high resolution localization, it is desirable to search beyond regular fluorescence for expansion of the usable color pallet and discriminate the probes at high resolution. Electron beam induced methods like CL and EDX expand the available colors visible at high resolution[20, 23]. Since CL is still photon based it's detection and discrimination is still based on the spectrum of light and thereby availability of filters. However, parameters such as CL lifetime upon

electron irradiation have already been explored to define specific nanoparticles in CL[37]. Another limitation of most nanoparticle probes used for CL is size, such as the relatively large and polydisperse FNDs used in chapter 4a[20]. Upon valuable proof-of-principle work for CL in biological samples, the next step is to develop smaller and monodisperse particles.

With EDX, probe development is not limited anymore to the spectrum of light and particle shape in EM for high-resolution discrimination and localization. In principle the periodic table of elements can be used, of which a proof-of-principle was shown for immunogold and cadmium-based QDs in chapter 4b[23]. In addition, heavy metal contrasting such as osmium, uranyl, lead, and addition stains can be used, comparable with eosin and hematoxylin in histology, upon definition of specific molecules they bind. Interestingly, defining structures and molecules with EDX can be performed based on endogenous elements, i.e. in the absence of probes, such as done for nitrogen, phosphor and sulfur based discrimination of cells in chapter 4b[23]. Moreover, optimized sample preparation protocols to prevent wash-out of elements and possibly improved detector sensitivity can aid to visualize the localization of more difficult elements such as iron, zinc, sodium etc. EDX has a long history material sciences and application and development for life sciences is still in it's infancy. Upon improvements in probe development, sample preparation and last but not least dedication from industry I predict a bright future for EDX imaging in life sciences.

ImmunoEM is limited in the number of targets and sample preparation is often a balance between ultrastructure and antigenicity preservation (discussed above). More generic immunoEM protocols would greatly benefit multi-target labeling with the potential of novel probes as discussed above. However for now, empirically testing of antibodies and exploring different sample preparation and labeling protocols, such as epon versus Tokuyasu or high pressure freezing followed by freeze substitution, is required for immunoEM. Moreover, novel CLEM probes and colorEM methods can be implemented in successful multi-target labeling protocols which otherwise use hard-to-dicriminate probes, such as different sized gold particles. In these cases it is not so much changing, but improving a winning team.

Nanotomy combined with successful post-embedding immunolabeling and EDX revealed the presence of intermediate exocrine and endocrine cells in islets of Langerhans of 'pre-diabetic' rats and early onset T1D donors (chapters 4b and 5a)[23]. The following hypothesis that damaged exocrine cells might serve as a trigger to T1D received a functional follow up study granted by the *European association for the study of diabetes* (EASD). Pilot experiments using cell lines suggested a beta cell specific response upon exocrine cell damage (chapter 5b). However, the cell line based model used is rather poor. Therefore, experimental models better controlling exocrine cell damage and reflecting a T1D beta cell response are required. Rodent or human isolated islets could replace the cell lines. Furthermore, induced pluripotent stem cell (iPSC) derived beta cells can be created and used as target cells in case of isolated islet shortage. Next, expression of a photosensitizing fluorescent protein in exocrine cells could selectively ablate these cells in co-culture with either cell lines, isolated islets or iPSC-derived beta cells. Moreover, beta cell stress upon exocrine-endocrine interactions could be studied in vivo by photosensitization induced exocrine cell damage in the vicinity of islet beta cells in a model organism such as the zebrafish.

References

1. de Boer, P., Hoogenboom, J. P. & Giepmans, B. N. Correlated light and electron microscopy: ultrastructure lights up! *Nat. Methods* **12**, 503-513 (2015).

2. Deschout, H. *et al*. Precisely and accurately localizing single emitters in fluorescence microscopy. *Nat. Methods* **11**, 253-266 (2014).

3. Schermelleh, L., Heintzmann, R. & Leonhardt, H. A guide to super-resolution fluorescence microscopy. *J. Cell Biol.* **190**, 165-175 (2010).

4. Peddie, C. J. & Collinson, L. M. Exploring the third dimension: volume electron microscopy comes of age. *Micron* **61**, 9-19 (2014).

5. Ravelli, R. B. *et al*. Destruction of tissue, cells and organelles in type 1 diabetic rats presented at macromolecular resolution. *Sci. Rep.* **3**, 1804 (2013).

6. Sokol, E. *et al*. Large-Scale Electron Microscopy Maps of Patient Skin and Mucosa Provide Insight into Pathogenesis of Blistering Diseases. *J. Invest. Dermatol.* **135**, 1763-1770 (2015).

7. Kuipers, J., Kalicharan, R. D., Wolters, A. H., van Ham, T. J. & Giepmans, B. N. Large-scale Scanning Transmission Electron Microscopy (Nanotomy) of Healthy and Injured Zebrafish Brain. *J. Vis. Exp.* **(111). doi**, 10.3791/53635 (2016).

8. Kuipers, J., de Boer, P. & Giepmans, B. N. Scanning EM of non-heavy metal stained biosamples: Large-field of view, high contrast and highly efficient immunolabeling. *Exp. Cell Res.* **337**, 202-207 (2015).

9. Schnell, U., Dijk, F., Sjollema, K. A. & Giepmans, B. N. Immunolabeling artifacts and the need for live-cell imaging. *Nat. Methods* **9**, 152-158 (2012).

10. Giepmans, B. N., Deerinck, T. J., Smarr, B. L., Jones, Y. Z. & Ellisman, M. H. Correlated light and electron microscopic imaging of multiple endogenous proteins using Quantum dots. *Nat Methods* **2**, 743-9 (2005).

11. Killingsworth, M. C., Lai, K., Wu, X., Yong, J. L. & Lee, C. S. Quantum dot immunocytochemical localization of somatostatin in somatostatinoma by Widefield Epifluorescence, super-resolution light, and immunoelectron microscopy. *J. Histochem. Cytochem.* **60**, 832-843 (2012).

12. Heinrich, U., Maurer, J., Koesling, D., Mann, W. & Forstermann, U. Immuno-electron microscopic localization of the alpha(1) and beta(1)-subunits of soluble guanylyl cyclase in the guinea pig organ of corti. *Brain Res.* **885**, 6-13 (2000).

13. Phend, K. D., Rustioni, A. & Weinberg, R. J. An osmium-free method of epon embedment that

preserves both ultrastructure and antigenicity for post-embedding immunocytochemistry. *J. Histochem. Cytochem.* **43**, 283-292 (1995).

14. van Rijnsoever, C., Oorschot, V. & Klumperman, J. Correlative light-electron microscopy (CLEM) combining live-cell imaging and immunolabeling of ultrathin cryosections. *Nat. Methods* **5**, 973-980 (2008).

15. Liv, N. *et al*. Simultaneous Correlative Scanning Electron and High-NA Fluorescence Microscopy. *PLoS One* **8**, e55707 (2013).

16. Peddie, C. J. *et al*. Correlative and integrated light and electron microscopy of in-resin GFP fluorescence, used to localise diacylglycerol in mammalian cells. *Ultramicroscopy* **143**, 3-14 (2014).

17. Watanabe, S. *et al*. Protein localization in electron micrographs using fluorescence nanoscopy. *Nat. Methods* **8**, 80-84 (2011).

18. Haring, M. T. *et al*. Automated sub-5 nm image registration in integrated correlative fluorescence and electron microscopy using cathodoluminescence pointers. *Sci. Rep.* **7**, 43621 (2017).

19. VAN Elsland, D. M. *et al*. Correlative light and electron microscopy reveals discrepancy between gold and fluorescence labelling. *J. Microsc.* **267**, 309-317 (2017).

20. Hemelaar, S. R. *et al*. Nanodiamonds as multi-purpose labels for microscopy. *Sci. Rep.* **7**, 720-017-00797-2 (2017).

21. Fukushima, S. *et al*. Correlative near-infrared light and cathodoluminescence microscopy using Y2O3:Ln, Yb (Ln = Tm, Er) nanophosphors for

multiscale, multicolour bioimaging. *Sci. Rep.* **6**, 25950 (2016).

22. Nagarajan, S. *et al*. Simultaneous cathodoluminescence and electron microscopy cytometry of cellular vesicles labeled with fluorescent nanodiamonds. *Nanoscale* **8**, 11588-11594 (2016).

23. Scotuzzi, M. *et al*. Multi-color electron microscopy by element-guided identification of cells, organelles and molecules. *Sci. Rep.* **7**, 45970 (2017).

24. Falke, M. *et al*. Element Analysis by EDX for Life Science: Light Elements and Bio-Mineralization. *Microscopy and Microanalysis* **19**, 222-223 (2013).

25. Roep, B. O., Atkinson, M. & von Herrath, M. Satisfaction (not) guaranteed: re-evaluating the use of animal models of type 1 diabetes. *Nat. Rev. Immunol.* **4**, 989-997 (2004).

26. In't Veld, P. Insulitis in human type 1 diabetes: a comparison between patients and animal models. *Semin. Immunopathol.* **36**, 569-579 (2014).

27. Atkinson, M. A., Eisenbarth, G. S. & Michels, A. W. Type 1 diabetes. *Lancet* **383**, 69-82 (2014).

28. Campbell-Thompson, M., Rodriguez-Calvo, T. & Battaglia, M. Abnormalities of the Exocrine Pancreas in Type 1 Diabetes. *Curr. Diab Rep.* **15**, 79-015-0653-y (2015).

29. Campbell-Thompson, M. L. *et al*. The influence of type 1 diabetes on pancreatic weight. *Diabetologia* **59**, 217-221 (2016).

30. Li, X. *et al*. Serum Trypsinogen Levels in Type 1 Diabetes. *Diabetes Care* **40**, 577-582 (2017).

31. Virostko, J., Hilmes, M., Eitel, K., Moore, D. J. & Powers, A. C. Use of the Electronic Medical Record to Assess Pancreas Size in Type 1 Diabetes. *PLoS One* **11**, e0158825 (2016).

32. Campbell-Thompson, M., Wasserfall, C., Montgomery, E. L., Atkinson, M. A. & Kaddis, J. S. Pancreas organ weight in individuals with disease-associated autoantibodies at risk for type 1 diabetes. *JAMA* **308**, 2337-2339 (2012).

33. Groom, J. R. & Luster, A. D. CXCR3 ligands: redundant, collaborative and antagonistic functions. *Immunol. Cell Biol.* **89**, 207-215 (2011).

34. Antonelli, A. *et al*. Chemokine (C-X-C motif) ligand (CXCL)10 in autoimmune diseases. *Autoimmun. Rev.* **13**, 272-280 (2014).

35. Frigerio, S. *et al*. Beta cells are responsible for CXCR3-mediated T-cell infiltration in insulitis. *Nat. Med.* **8**, 1414-1420 (2002).

36. Uno, S. *et al*. Expression of chemokines, CXC chemokine ligand 10 (CXCL10) and CXCR3 in the inflamed islets of patients with recent-onset autoimmune type 1 diabetes. *Endocr. J.* **57**, 991-996 (2010).

37. Garming, M. W. H. *et al*. Nanoparticle discrimination based on wavelength and lifetime-multiplexed cathodoluminescence microscopy. *Nanoscale* **9**, 12727-12734 (2017).

Appendix

Nederlandse samenvatting

Het toepassen van verschillende microscopische technieken is al vele jaren essentieel om de regulatie van het leven en ziektes te bestuderen. Constante ontwikkeling op het gebied van hardware, software, moleculaire targeting, enzovoorts, maakt het mogelijk om in toenemend mate meer moleculaire patronen te zien op hoge resolutie. Gecorreleerde licht (LM) en elektronenmicroscopie (EM; CLEM) maakt gebruik de sterke kanten van beide microscopische technieken om vervolgens elkaars zwaktes aan te vullen. Fluorescentie LM wordt gebruikt om moleculen specifiek en efficiënt aan te tonen, mogelijk in levende cellen, en kan kleur aanbrengen in grijze EM data. Vervolgens kan met EM op hoge resolutie context worden gegeven aan de data die zijn opgenomen met LM. **Hoofdstuk 2** geeft een overzicht van recente ontwikkeling op het gebied van CLEM met betrekking tot sample voorbereiding, het opnemen en correleren van data, speciale probes en geeft toekomst perspectieven[1]. Verder is er voor nieuwe gebruikers een handleiding met verschillende tips, inclusief een literatuuroverzicht met eerder toegepaste CLEM strategieën. Aangezien er meerdere manieren zijn om CLEM uit te voeren hangt de strategie voornamelijk af van het soort en grootte van het materiaal in combinatie met de specifieke vraagstelling. Verder hangt het er nog van af of pre- of post-inbedding kleuring van toepassing is, de mogelijkheid bestaat om genetisch gecodeerde labels te gebruiken, in hoeverre epitopen nog herkend kunnen worden en wat voor microscopen beschikbaar zijn. Er bestaan veel gespecialiseerde en dure apparaten zoals geïntegreerde microscopen, gespecialiseerde sample houders, 3D EM microscopen enzovoorts, waardoor het voor nieuwe gebruikers met een gecompliceerde vraagstelling wordt aangeraden om samen te werken met meer ervaren laboratoria. Echter, voor eenvoudigere vraagstellingen volstaat het vaak om gebruik te maken van een standaard confocaal microscoop en minder gecompliceerde elektronenmicroscopen die voor handen zijn op de meeste onderzoeksinstellingen, in combinatie met reguliere labeling strategieën en sample bereiding.

Lange tijd bestond er een leemte in de opnameafmetingen tussen LM en EM. Met de ontwikkeling van superresolutie fluorescentie microscopie benadert de LM schaal die van EM[2, 3]. Aan de andere kant worden de afmetingen van LM en EM dichter bij elkaar gebracht door recente ontwikkelingen in 3D- en grote oppervlakte 2D EM technieken[4, 5]. Klassieke transmissie EM (TEM) op ultradunne coupes op hoge resolutie is beperkt tot een beeld van slechts een paar micrometer, waardoor de complete cellulaire en weefsel context niet zichtbaar is. Door middel van scanning transmissie EM (STEM) op grote schaal kunnen complete weefsel doorsnedes worden opgenomen om vervolgens te analyseren op een ‘google-earth’-achtige manier. Deze data worden publiekelijk toegankelijk na publicatie en de methode wordt nanotomie, oftewel nano-anatomie, genoemd[6, 7]. Echter, de grote hoeveelheid grijze data die met nanotomie opgenomen kunnen worden zijn moeilijk te analyseren. Het doel in dit proefschrift was om kleur te introduceren in deze datasets met behulp van affiniteit gebaseerde labels tegen endogene moleculen in (humaan) weefsel, wat niet mogelijk is met genetisch gecodeerde labels.

De identificatie van cellen en structuren kan worden bereikt door middel van post-inbedding immmuunlabeling met behulp van quantum dots (QDs) zoals beschreven in **hoofdstuk 3**[8]. Ten opzichte van pre-inbedding immuunlabeling is het behoud van de ultrastructuur tijdens post-inbedding labeling superieur, aangezien voor pre-inbedding labeling de ultrastructuur sterk wordt aangetast door een benodigde permeabilisatie stap[9]. Bovendien hebben nanodeeltjes die zichtbaar

zijn met EM een lage penetratie diepte in intacte cellen en weefsel[10]. Echter, in de meeste gevallen is post-inbedding labeling, zoals uitgevoerd in hoofdstuk 3, niet succesvol omdat epitopen gemaskeerd kunnen worden door sterke fixatie en de inbeddingshars. Slechts ongeveer 10% van de geteste doelen konden succesvol worden gelabeld (data niet weergegeven). Het succes van post-inbedding labeling is waarschijnlijk deels afhankelijk van concentratie van de target moleculen, insuline en amylase worden bijvoorbeeld succesvol gelabeld en komen in hoge concentraties voor in hun respectievelijke secretoire granules. Aanpassingen aan de sample preparatie protocollen zou de labeling efficiëntie kunnen verhogen, zoals osmium-vrije inbedding, sterk etsen, of inbedden in een licht hydrofiele hars[11-13]. Deze aanpassingen kunnen echter weer een negatief effect hebben op het behoud van de ultrastructuur. Daarom is het kiezen van een immuunEM methode vaak een balans tussen efficiëntie en structuur behoud. De gouden standaard voor immunoEM is de Tokuyasu methode door middel van ontdooien van cryocoupes[14]. Echter, een homogene cryofixatie, nodig voor Tokuyasu, is vaak niet mogelijk met relatief grote stukken weefsel.

Geïntegreerde licht microscopen in een EM, zoals de SECOM (Delmic, Delft, Nederland), zijn ontwikkeld voor hoge precisie CLEM correlatie en ter voorkoming van eventuele schade aan samples tijdens overdracht tussen de verschillende microscopen[15]. Een vereiste voor geïntegreerde CLEM is dat de samples zowel fluorescent als geschikt voor EM zijn. Fluorescentie wordt normaal gesproken uitgedoofd door osmium tijdens reguliere EM sample preparatie. Speciale protocollen zijn ontwikkeld om fluorescentie van fluorescente eiwitten te behouden in gekweekte cellen[16, 17]. Maar weefsel samples na post-inbedding immuunlabeling, zoals geoptimaliseerd is in hoofdstuk 3, met fluorescente markers kunnen ook gebruikt worden[18].

Post-inbedding immuunlabeling met QDs geeft een tienvoud hogere labeling efficiëntie ten opzichte van het meer klassieke immunogoud (**hoofdstuk 3**)[8]. Mogelijk komt dit door een sterkere sterische hinder van de goud deeltjes[19]. Bovendien zijn QDs zowel fluorescent als elektronen dicht, waardoor ze zeer geschikt zijn voor CLEM toepassingen (hoofdstuk 2, figuur 2a)[1]. Het contrast van QDs is minder vergeleken met immunogoud waardoor QDs vaak gemaskeerd worden door het contrast van het weefsel als het met zware metalen gekleurd is. Wanneer uranylacetaat en loodcitraat contrastering achterwege wordt gelaten worden QDs beter zichtbaar. Echter, voor goed contrast in TEM is uranyl en lood kleuring noodzakelijk. Met STEM, aan de andere kant, is het contrast van de opnames voldoende als deze zware metalen niet worden toegepast en is het dus mogelijk om QDs goed zichtbaar te maken ten opzichte van de ultrastructuur.

De beschikbaarheid van speciale CLEM probes zoals QDs is redelijk zeldzaam aangezien de meeste microscopische probes ofwel fluorescent ofwel elektronendicht, of de deeltjes zijn te groot voor precieze lokalisatie. De noodzaak voor elektronen dichtheid kan omzeild worden door fotonen emissie vanaf specifieke probes te induceren door middel van elektronen bundel aanstraling, genaamd cathodoluminiscentie (CL). Die fotonen kunnen dan gedecteerd worden met de SECOM. Vervolgens kan de lokalisatie waar de fotonen afkomstig zijn op nanometer precisie bepaald worden. Fluorescente nanodiamantjes (FNDs) hebben CL mogelijkheden. In **hoofdstuk 4a** werden FNDs, ter grootte van 40 tot 70 nm, op hoge resolutie door middel van CL gelokaliseerd in ultradunne coupes na zowel fagocytose als immuunlabeling met streptavidine-geconjugeerde deeltjes[20]. Tot dan toe werden de meeste CL experimenten voor biologische toepassing uitgevoerd met grote deeltjes van 100 tot 150 nm en gelimiteerd tot cel-opname analyses[21, 22]. Alhoewel FNDs potentie hebben als CLEM probe zijn ze met een grootte van 40 tot 70 nm nog aan de grote kant, bijvoorbeeld vergeleken met QDs van 10 tot 15 nm, en zijn ze erg polydispers. Bovendien is de labeling efficiëntie met streptavidine-geconjugeerde FNDs laag ten opzichte van QDs. Deze eerste resultaten maken echter de weg vrij voor verdere optimalisatie van FNDs voor verdere CLEM toepassingen.

In **hoofdstuk 4b** werd een andere manier beschreven om kleur te introduceren met behulp van de primaire elektronen bundel, genaamd *electron dispersive X-ray* spectroscopie (EDX)[23]. Als een elektronen bundel interacties aan gaat met een sample kunnen de elektronen die in een binnenschil van de aanwezige atomen verkeren worden uitgestoten wat resulteert in een elektronen leemte. Vervolgens vult een elektron vanuit een verder naar buiten liggende schil met een hogere energie deze leemte en het verschil in energie word vrijgelaten in de vorm van röntgenstraling, met een spectrum dat specifiek is voor elk element. Door een speciale EDX detector toe te voegen aan een SEM kan per pixel in een sample de verhouding aan elementen worden gekarakteriseerd en worden geconverteerd naar kleuren plaatjes met EM resolutie ('kleurenEM'). De toepassing van EDX in levenswetenschappen is gelimiteerd omdat EDX detectoren veelal niet gevoelig genoeg zijn om elementen te onderscheiden en te karakteriseren in biologisch materiaal, dat voornamelijk uit koolstof bestaat. Door gebruik te maken van een sterk gevoelige *silicon drift detector* (SDD)[24] met *high current* op een hoge resolutie SEM is het nu mogelijk om subcellulaire variaties in elementaire samenstelling op de nanometer schaal in ultradunne coupes van biologische materiaal te bepalen. Nanodeeltjes met een verschillende elementen samenstelling, immunogoud alsook cadmium bevattende QDs, konden worden onderscheiden na post-inbedding immuunlabeling. Verder konden subcellulaire structuren worden herkend door middel van lokale verrijking van endogene elementen zoals zwavel in insuline granules, aangezien insuline peptiden een relatief hoog gehalte aan cysteïnes hebben. Bovendien konden verschillende celtypes in de eilandjes van Langerhans van een rat worden gediscrimineerd op basis van verrijking van hoge gehaltes aan specifieke elementen in de secretoire granules. KleurenEM werd gepionierd in eilandjes van Langerhans van een diabetisch gevoelige *BioBreeding* (BB) rat, wat een model is voor type 1 diabetes (T1D), met nog een normaal bloed glucose gehalte. Onverwacht werden door een combinatie van kleurenEM en post-inbedding immuunlabeling endocriene cellen aan de rand van een eilandje geïdentificeerd die ook granules bevatten van exocriene pancreas cellen, samen met een aangetaste ultrastructuur. Deze intermediaire cellen werden enkel geobserveerd in eilandjes van diabetisch gevoelige- en niet in controle diabetisch resistente ratten (ongepubliceerde data), wat kan wijzen op een schadelijke interactie tussen exocriene en endocriene cellen aan het begin van diabetes in BB ratten.

De mechanismen die aanleiding geven tot de auto-immuun destructie van insuline producerende bètacellen in de eilandjes van Langerhans resulterend in T1D worden nog slecht begrepen waardoor alternatieven voor insuline therapie uitgesloten worden. Kennis van cellulaire compositie en de micro-omgeving van zowel T1D-onderhevige als controle niet-diabetische eilandjes is essentieel voor het begrijpen van de etiologie van T1D. Nanotomie is gepionierd in het BB rat model met als doel om T1D pathologie op nanometer schaal gedurende verschillende stadia van de ziekte onbevooroordeeld te onderzoeken[5]. Alhoewel verschillende diermodellen voor T1D inzichten hebben verschaft die van onschatbare waarde zijn met betrekking tot auto-immuun gemedieerde bètacel dood, zijn er belangrijke discrepanties tussen de diermodellen en humane T1D pathogenese[25, 26]. Derhalve is een online nanotomie database gecreëerd met humaan T1D pancreas weefsel afkomstig van het *network of pancreatic organ donors* (nPOD), zoals beschreven in **hoofdstuk 5a**. De database, met de data gekoppeld aan specifieke donor nummers, wordt openbaar gemaakt na publicatie. Hoewel door een beperkt aantal eilandjes per donor de database minder geschikt is voor kwantitatieve analyse, kan een meer kwalitatieve inspectie naar specifieke subcellulaire veranderingen van grote toegevoegde waarde zijn voor andere analyses uitgevoerd door andere nPOD onderzoekers op pancreas weefsel van de zelfde donor.

T1D wordt gezien als een auto-immuun ziekte aangedreven door T cellen[27]. Na een eerste analyse van de nPOD nanotomie database werden onverwachte immuuncellen geobserveerd, inclusief een bepaald mast cel subtype specifiek in T1D donor weefsel. Verder werden in combinatie met EDX

analyse endocriene en exocriene intermediaire cellen geïdentificeerd in eilandjes van twee van de acht T1D donoren en niet in de niet-diabetische donoren. Aangezien intermediaire cellen werden geobserveerd in zowel vroegtijdige humane T1D donoren als 'pre-diabetische' ratten, stellen wij als hypothese dat exocriene cel schade bètacel stress in gang zet bij de aanvang van T1D. Dit gaat hand in hand met het huidige idee dat naast de eilandjes van Langerhans ook de exocriene pancreas is aangetast tijdens T1D[28]. Terwijl de pancreas maar voor een paar procent bestaat uit eilandjes hebben T1D patiënten een significant verkleinde pancreas[29, 30]. Daarnaast wordt in patiënten ook een inadequate exocriene werking gerapporteerd[31]. Bovendien werd in auto-antilichaam positieve nPOD donoren zonder T1D al een verlaagd pancreas gewicht geobserveerd, wat een indicatie geeft dat verandering van de exocriene pancreas al gaande zijn voor verandering aan de eilandjes zoals te zien is in T1D[32]. In **hoofdstuk 5** werd een functionele vervolgstudie beschreven, aanvullend aan de tot dusver statische EM data. Hierin werd een pro-inflammatoire respons van bètacellen na stimulatie door beschadigde exocriene cellen gesuggereerd. Insuline producerende cel lijnen hadden een verhoogde *C-X-C motif chemokine ligand 10* (CXCL10) mRNA expressie na stimulatie door exocriene cel lijn lysaten vergeleken met een negatieve controle en bètacel lysaten behandeling. CXCL10 is een potente chemoattractant voor T cellen[33] en de expressie is sterk geassocieerd met vroegtijdige T1D[34]. Bovendien werden bètacellen geïdentificeerd als een mogelijke bron voor CXCL10 tijdens T1D[35, 36]. In vervolg proeven zullen meerdere genen die rol spelen bij bètacel stress worden onderzocht.

Samenvattend geeft dit proefschrift ten eerste een overzicht van recente CLEM ontwikkelingen inclusief een praktische handleiding. Daarnaast werd een efficiënte labeling op EM materiaal geoptimaliseerd in combinatie met verbeterde detectie methodes, wat vervolgens tot nieuwe inzichten in de T1D pathogenese heeft geleid.

References

1. de Boer, P., Hoogenboom, J. P. & Giepmans, B. N. Correlated light and electron microscopy: ultrastructure lights up! *Nat. Methods* **12**, 503-513 (2015).

2. Deschout, H. *et al*. Precisely and accurately localizing single emitters in fluorescence microscopy. *Nat. Methods* **11**, 253-266 (2014).

3. Schermelleh, L., Heintzmann, R. & Leonhardt, H. A guide to super-resolution fluorescence microscopy. *J. Cell Biol.* **190**, 165-175 (2010).

4. Peddie, C. J. & Collinson, L. M. Exploring the third dimension: volume electron microscopy comes of age. *Micron* **61**, 9-19 (2014).

5. Ravelli, R. B. *et al*. Destruction of tissue, cells and organelles in type 1 diabetic rats presented at macromolecular resolution. *Sci. Rep.* **3**, 1804 (2013).

6. Sokol, E. *et al*. Large-Scale Electron Microscopy Maps of Patient Skin and Mucosa Provide Insight into Pathogenesis of Blistering Diseases. *J. Invest. Dermatol.* **135**, 1763-1770 (2015).

7. Kuipers, J., Kalicharan, R. D., Wolters, A. H., van Ham, T. J. & Giepmans, B. N. Large-scale Scanning Transmission Electron Microscopy (Nanotomy) of Healthy and Injured Zebrafish Brain. *J. Vis. Exp.* **(111). doi**, 10.3791/53635 (2016).

8. Kuipers, J., de Boer, P. & Giepmans, B. N. Scanning EM of non-heavy metal stained biosamples: Large-field of view, high contrast and highly efficient immunolabeling. *Exp. Cell Res.* **337**, 202-207 (2015).

9. Schnell, U., Dijk, F., Sjollema, K. A. & Giepmans, B. N. Immunolabeling artifacts and the need for live-cell imaging. *Nat. Methods* **9**, 152-158 (2012).

10. Giepmans, B. N., Deerinck, T. J., Smarr, B. L., Jones, Y. Z. & Ellisman, M. H. Correlated light and electron microscopic imaging of multiple endogenous proteins using Quantum dots. *Nat Methods* **2**, 743-9 (2005).

11. Killingsworth, M. C., Lai, K., Wu, X., Yong, J. L. & Lee, C. S. Quantum dot immunocytochemical localization of somatostatin in somatostatinoma by Widefield Epifluorescence, super-resolution light, and immunoelectron microscopy. *J. Histochem. Cytochem.* **60**, 832-843 (2012).

12. Heinrich, U., Maurer, J., Koesling, D., Mann, W. & Forstermann, U. Immuno-electron microscopic localization of the alpha(1) and beta(1)-subunits of soluble guanylyl cyclase in the guinea pig organ of corti. *Brain Res.* **885**, 6-13 (2000).

13. Phend, K. D., Rustioni, A. & Weinberg, R. J. An osmium-free method of epon embedment that preserves both ultrastructure and antigenicity for post-

embedding immunocytochemistry. *J. Histochem. Cytochem.* **43**, 283-292 (1995).

14. van Rijnsoever, C., Oorschot, V. & Klumperman, J. Correlative light-electron microscopy (CLEM) combining live-cell imaging and immunolabeling of ultrathin cryosections. *Nat. Methods* **5**, 973-980 (2008).

15. Liv, N. *et al*. Simultaneous Correlative Scanning Electron and High-NA Fluorescence Microscopy. *PLoS One* **8**, e55707 (2013).

16. Peddie, C. J. *et al*. Correlative and integrated light and electron microscopy of in-resin GFP fluorescence, used to localise diacylglycerol in mammalian cells. *Ultramicroscopy* **143**, 3-14 (2014).

17. Watanabe, S. *et al*. Protein localization in electron micrographs using fluorescence nanoscopy. *Nat. Methods* **8**, 80-84 (2011).

18. Haring, M. T. *et al*. Automated sub-5 nm image registration in integrated correlative fluorescence and electron microscopy using cathodoluminescence pointers. *Sci. Rep.* **7**, 43621 (2017).

19. Van Elsland, D. M. *et al*. Correlative light and electron microscopy reveals discrepancy between gold and fluorescence labelling. *J. Microsc.* **267**, 309-317 (2017).

20. Hemelaar, S. R. *et al*. Nanodiamonds as multi-purpose labels for microscopy. *Sci. Rep.* **7**, 720-017-00797-2 (2017).

21. Fukushima, S. *et al*. Correlative near-infrared light and cathodoluminescence microscopy using Y2O3:Ln, Yb (Ln = Tm, Er) nanophosphors for multiscale, multicolour bioimaging. *Sci. Rep.* **6**, 25950 (2016).

22. Nagarajan, S. *et al*. Simultaneous cathodoluminescence and electron microscopy cytometry of cellular vesicles labeled with fluorescent nanodiamonds. *Nanoscale* **8**, 11588-11594 (2016).

23. Scotuzzi, M. *et al*. Multi-color electron microscopy by element-guided identification of cells, organelles and molecules. *Sci. Rep.* **7**, 45970 (2017).

24. Falke, M. *et al*. Element Analysis by EDX for Life Science: Light Elements and Bio-Mineralization. *Microscopy and Microanalysis* **19**, 222-223 (2013).

25. Roep, B. O., Atkinson, M. & von Herrath, M. Satisfaction (not) guaranteed: re-evaluating the use of animal models of type 1 diabetes. *Nat. Rev. Immunol.* **4**, 989-997 (2004).

26. In't Veld, P. Insulitis in human type 1 diabetes: a comparison between patients and animal models. *Semin. Immunopathol.* **36**, 569-579 (2014).

27. Atkinson, M. A., Eisenbarth, G. S. & Michels, A. W. Type 1 diabetes. *Lancet* **383**, 69-82 (2014).

28. Campbell-Thompson, M., Rodriguez-Calvo, T. & Battaglia, M. Abnormalities of the Exocrine Pancreas in Type 1 Diabetes. *Curr. Diab Rep.* **15**, 79-015-0653-y (2015).

29. Campbell-Thompson, M. L. *et al*. The influence of type 1 diabetes on pancreatic weight. *Diabetologia* **59**, 217-221 (2016).

30. Virostko, J., Hilmes, M., Eitel, K., Moore, D. J. & Powers, A. C. Use of the Electronic Medical Record to Assess Pancreas Size in Type 1 Diabetes. *PLoS One* **11**, e0158825 (2016).

31. Li, X. *et al*. Serum Trypsinogen Levels in Type 1 Diabetes. *Diabetes Care* **40**, 577-582 (2017).

32. Campbell-Thompson, M., Wasserfall, C., Montgomery, E. L., Atkinson, M. A. & Kaddis, J. S. Pancreas organ weight in individuals with disease-associated autoantibodies at risk for type 1 diabetes. *JAMA* **308**, 2337-2339 (2012).

33. Groom, J. R. & Luster, A. D. CXCR3 ligands: redundant, collaborative and antagonistic functions. *Immunol. Cell Biol.* **89**, 207-215 (2011).

34. Antonelli, A. *et al*. Chemokine (C-X-C motif) ligand (CXCL)10 in autoimmune diseases. *Autoimmun. Rev.* **13**, 272-280 (2014).

35. Frigerio, S. *et al*. Beta cells are responsible for CXCR3-mediated T-cell infiltration in insulitis. *Nat. Med.* **8**, 1414-1420 (2002).

36. Uno, S. *et al*. Expression of chemokines, CXC chemokine ligand 10 (CXCL10) and CXCR3 in the inflamed islets of patients with recent-onset autoimmune type 1 diabetes. *Endocr. J.* **57**, 991-996 (2010).

Dankwoord

Het bedrijven van wetenschap is typisch iets wat niet gedaan wordt door een enkel individu. Wetenschappelijke vooruitgang wordt voornamelijk geboekt door middel van samenwerking tussen mensen in een groepsverband waarin elk individu een schakel vormt van essentieel belang. Daarom wil ik iedereen bedanken die heeft bijgedragen aan het tot stand komen van dit proefschrift.

Allereerst wil ik mijn groepsgenoten van het Giepmans lab binnen de afdeling celbiologie van het UMCG bedanken. Van **Jeroen Kuipers** kon ik alle kennis en fijne kneepjes van de wondere wereld van de elektronenmicroscopie leren. Daarnaast vond ik het erg fijn om samen te werken aan het beruchte '*Kuipers & de Boer 2015'* paper. Ook wil ik mijn overige kantoorgenoten, **Anouk Wolters**, **Marit de Beer** en **Nicole Pirozzi** bedanken voor onze samenwerking en het tot stand komen van een zeer prettige werkomgeving. Onder andere hierdoor ga ik elke dag met veel plezier naar het lab en het heeft absoluut bijgedragen aan mijn beslissing om nog een aantal jaar te blijven plakken voor een postdoctoraal project. Jeroen en Anouk ook bedankt dat jullie mijn paranimfen willen zijn. Naast elektronenmicroscopie is ook fluorescente lichtmicroscopie belangrijk geweest voor dit proefschrift. Daarom wil ik **Klaas Sjollema** bedanken voor het leren te bedienen van de geavanceerde microscopen binnen ons imaging centrum. **Peter Duinkerken** wil ik bedanken voor zijn bijdrage aan het diabetes project. Ik kan niet ontkennen dat dit project tijdens jouw stage een enorme boost heeft gekregen. Het is dan ook prettig samenwerken nu je onze groep als collega bent komen versterken. Veel succes volgend jaar met je Master! Ook wil ik alle studenten bedanken die zich hebben ingezet voor de verschillende projecten binnen mijn promotietraject.

Mijn grote dank gaat ook zeker uit naar **Ben Giepmans** voor de kans die ik heb gekregen om aan dit project te werken en de manier waarop je mijn mentor was gedurende mijn promotietraject. Het was erg fijn om een zekere vrijheid te hebben binnen het project om mijn eigen keuzes te maken en daardoor mijn eigen richting kon kiezen. Daarnaast bleef je me ook altijd uitdagen door kritisch te zijn en door mezelf te leren kritisch te reflecteren. Naast een uitstekende mentor, heb ik jou ook altijd als mijn inspiratiebron gezien voor hoe ik, in mijn ogen, goede wetenschap kon bedrijven.

Naast onze eigen groep wil ik ook mijn dank betuigen aan **Jacob Hoogenboom** en zijn groep aan de TU Delft. Door de jaren heen, gedurende mijn promotietraject, heb ik deze interdisciplinaire en tevens vruchtbare samenwerking tussen onze beide groepen steeds meer zien groeien. Ik kijk dan ook uit naar mijn postdoctoraal project, waarin de samenwerking tussen onze groepen centraal komt te staan en de celbiologie en technische ontwikkelingen op het gebied van geavanceerde microscopie nog dichter bij elkaar komen.

Het leven bestaat niet alleen uit werken, daarom wil ik mijn familie en vrienden bedanken voor alle steun en vertrouwen in mijn project en voor de nodige ontspanning naast mijn werk. Mijn ouders wil ik bedanken voor de mogelijkheden, ondersteuning, vertrouwen en aanmoediging van mijn studie en werk. Hetzelfde geldt voor mijn broer **Jeroen** en zusje **Joyce**. Ook ben ik blij met mijn schoonfamilie die ik lief heb als ware het mijn directe familie.

Allerlaatst wil ik mijn vriendin en aanstaande vrouw **Danielle** bedanken voor haar steun, aanmoediging en liefde. Ik ben heel blij dat jij in mijn leven bent gekomen en dat ik in jou mijn zielsverwant heb gevonden. Ook heb ik door jou het mooie Makkum leren kennen waar ik naast het werken aan mijn project momenten van rust kon vinden.

Pascal de Boer

About the author

Pascal de Boer was born on the 28th of December 1988 Leeuwarden, The Netherlands. After completing secondary school in 2007 (VWO at Piter Jelles Montessori, Leeuwarden) he went for his Bachelor in biology at the University of Groningen with a major in biomedical sciences and a minor in behavior and neurosciences. Subsequently, from 2011 until 2013, Pascal followed the biomedical sciences Master at the University of Groningen. During his Master's, Pascal worked on two research projects. First at the department of cell biology at the University Medical Center Groningen, he joined the group of Dr. Wia Baron under the supervision of Dr. Eric Sikkema, where he worked on a project elucidating differences in brain white- and grey matter derived astrocytes in the context of remyelination during multiple sclerosis. His final project was performed at the department of experimental hematology at the University Medical Center Groningen in the group of Prof. Dr. J.J. Schuringa under the supervision of Dr. Hein Schepers, where he investigated the role of a transcriptional co-activator, CITED2, in context of chronic myeloid leukemia.

In February 2014 Pascal started his Ph.D. project at the department of cell biology of the University Medical Center Groningen in the group of Dr. Ben N. G. Giepmans. The Ph.D. project was part of a larger project called Microscopy Valley, funded by NWO *Stichting Techniek en Wetenschap* (STW). Within this project Pascal aimed to develop novel probes and labeling approaches for correlated light and electron microscopy with a subsequent implementation in type 1 diabetes research as described in this thesis. After completion of the Ph.D. project in February 2018, Pascal stayed in the Giepmans lab within the department of cell biology at the University Medical Center Groningen to start with a postdoctoral project. The new project aims to develop probes, with a focus on fluorescent proteins, for electron-beam induced super resolution fluorescence microscopy, with implementation in type 1 diabetes research. This project will be in close collaboration with the lab of Dr. Jacob P. Hoogenboom of the Technical University Delft.

List of publications

Garming MWH., Weppelman IGC., **de Boer P**, Martínez FP, Schirhagl R, Hoogenboom JP, Moerland RJ, Nanoparticle discrimination based on wavelength and lifetime-multiplexed cathodoluminescence microscopy. *Nanoscale* **9**, 12727-12734 (2017)

de Boer P# / Hemelaar SR#, Chipaux M, Zuidema W, Hamoh T, Martínez FP, Nagl A, Hoogenboom JP, Giepmans BNG, Schirhagl R, Nanodiamonds as multi-purpose labels for microscopy. *Scientific Reports* **7**, 720-017-00797-2 (2017) - # equal authorship

Scotuzzi M# / Kuipers J# / Wensveen DI#, **de Boer P**, Hagen CW, Hoogenboom JP# / Giepmans BNG#, Multi-color electron microscopy by element-guided identification of cells, organelles and molecules. *Scientific Reports* 7;7:45970. doi: 10.1038/srep45970 (2017) - # equal authorship

de Boer P# / Kuipers J#, Giepmans BNG, Scanning EM of non-heavy metal stained biopsamples: Large-field of view, high contrast and highly efficient immunolabeling. *Experimental Cell Research* 337(2): 202-207 (2015) - # equal authorship

de Boer P, Hoogenboom JP, Giepmans BNG, Correlated light and electron microscopy: ultrastructure lights up! *Nature Methods* 22(6): 503-513 (2015)